Herbert Oertel

Flow Control

Theoretical Concept of Absolute Instability

Herbert Oertel

Flow Control
Theoretical Concept of Absolute Instability

Flow Control

Theoretical Concept of Absolute Instability

by
Herbert Oertel

Translation
Katherine Asfaw

Author

Prof. Prof. e.h. Dr.-Ing. habil. Herbert Oertel, Ordinarius

Karlsruher Institut für Technologie, Institut für Strömungslehre (KIT)
Kaiserstr. 10, 76131 Karlsruhe

Contents

Preface

At the 37th Prandtl memorial lecture in Brunswick on *Regions of Viscous Flow*, H. Oertel 1994 used L. Prandtl's famous 1905 article *On the Motion of Fluids at Very Low Friction* as a basis to treat for the first time the stability theory of local perturbations in boundary layers and wake flows, as well as their practical application in the flow control of the flow past vehicles and the boundary layer of wings of civil aircraft. By means of stability theory of local perturbations, the regions of expansion of perturbation waves can be calculated for both laminar and turbulent flows, for which the boundary lines can be considered to be characteristic lines of the viscous flow.

This article presents how the stability theory concept of *absolute instability* has advanced and proven itself in practice in the last 15 years in terms of the efficient flow control of laminar and turbulent boundary-layer flows and wake flows, as well as for fluid mechanical resonators.

Karlsruhe, March 2010   Herbert Oertel

1 Introduction

In 1904, on the occasion of the Third International Mathematics Congress in Heidelberg, L. Prandtl presented a paper *On the Motion of Fluids at Very Low Friction.* This resulted in the mathematical approach to *boundary-layer theory*, which was further developed by his disciple *H. Schlichting* 1951 and later *H. Schlichting and K. Gersten* 2003, 2006 for practical application in aerodynamics. In boundary-layer theory the flow at large Reynolds numbers is regarded as a perturbation of the corresponding potential flow without friction. The classical Orr-Sommerfeld stability analysis of the laminar boundary layer, which leads to the primary instability of *Tollmien-Schlichting waves*, may be found in the chapter of *H. Oertel* 2003, 2006 on *Onset of Turbulence.* Stability diagrams with pressure gradient, suction, heat transfer and wall roughness offer the possibility of controlling boundary-layer flows.

Already in his first boundary-layer article, *L. Prandtl* 1905 demonstrated the effect of boundary-layer suction on the flow past a circular cylinder. Figure 1.1 shows that separation of the flow is delayed on the side where the suction is carried out and consequently the drag of the cylinder is considerably reduced. In the wake, the periodic vortex shedding called the von Kármán vortex street is supressed. Stability analysis of the flow with suction yields a stable wake flow.

Prandtl describes the process of periodic flow separation at the cylinder with a periodically varying interface between the fluid flowing past the body and the fluid flowing backward behind the cylinder. If this interface is drawn off at a slit behind the cylinder, the periodic flow separation behind the cylinder vanishes and the drag of the body in the flow is reduced.

This explanation of Prandtl is contrasted with a mathematically rigorous explanation of the supression of periodic vortex shedding in the wake of a cylinder. This leads to the topic of the article on flow control and the theory of stability of convective and absolute instability (*H. Oertel* 1989, 1990, 1994, 1995, 1997).
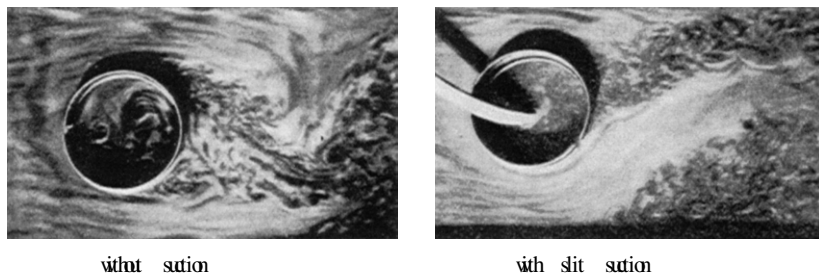

without suction   with slit suction

Fig. 1.1. Flow control with boundary-layer suction, *L. Prandtl* 1905

In Fig. 1.2, showing the direct wake of a cylinder, there is a distinction between the *absolutely unstable* region downstream of the resonance point R and the *convectively unstable* region of the wake flow. The absolutely unstable region is defined as the viscous flow region in which locally introduced perturbations are amplified in space and in time and affect the entire absolutely unstable flow region as time progresses. In the convectively unstable region, locally introduced perturbations are swept downstream and can no longer influence the original position of the perturbation as time progresses. Therefore the resonance point R shown in Fig. 1.2 is upstream from the first point at which an effect of the flow on the cylinder is possible. *W. Koch* 1985 concluded from this that the onset of the von Kármán vortex street can be understood as a resonance phenomenon in the absolutely unstable region of the wake of the cylinder. This idea has since been confirmed, and as a consequence the inviscid theory of the von Kármán vortex street formulated for the far field of the cylinder wake flow cannot provide the correct theoretical explanation for its onset. This had remained unaccounted for until now only because the experimentally determined shedding frequencies behind the cylinder differ by only around 10% from the original values of the von Kármán theory.

The classification of a flow field into different flow regions is known from gas dynamics. For mathematical reasons, for inviscid flows this has led to flow regions with elliptical, parabolic or hyperbolic differential equations. As shown in Fig. 1.3, the *elliptical* region of (inviscid) supersonic flow past a cylinder corresponds to the *absolutely unstable* region in the wake of viscous flow past a cylinder. In both regions locally introduced perturbations are amplified in time and space and affect the entire elliptical (or, correspondingly, absolutely unstable) region as time progresses. In the *hyperbolic* region of inviscid wake flow, as for the *convectively unstable* region of viscous flow past a cylinder, locally introduced perturbations are swept downstream. Thus it can be concluded that efficient flow control may be applied for inviscid flow in the elliptical region and for viscous flow in the absolutely unstable region.

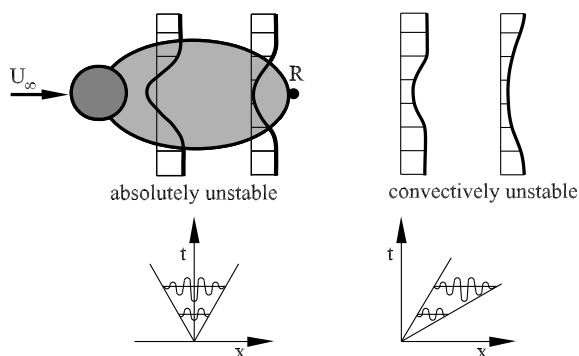A further impressive experiment on control of the wake flow of a cylinder was

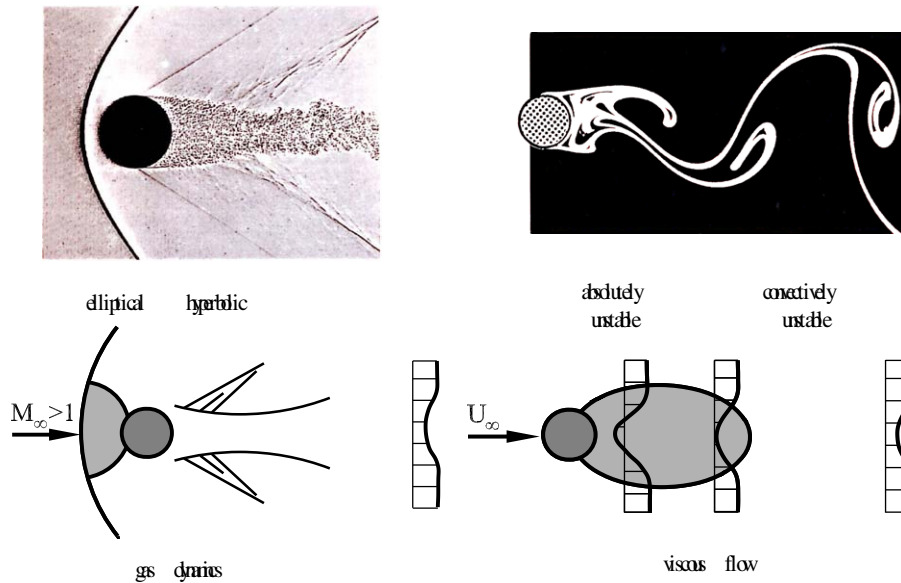Fig. 1.2. Flow regions in the wake flow

4

Fig. 1.3. Classification of regions of gas dynamics and of viscous flow

carried out 90 years after Prandtl by *P.J. Strykowski* 1990 and was demon-
strated by *H. Oertel* 1994 in the Prandtl memorial lecture as an optical con-
firmation of the existence of absolutely unstable regions in the lecture hall.
In order to suppress the von Kármán vortex street, instead of the suction
technique of Prandtl, a perturbation cylinder is placed in the wake of the
main cylinder, as shown in Fig. 1.4. At small Reynolds numbers, the flow past
the perturbation cylinder causes the absolutely unstable region to be swept
downstream. The formation of periodic flow separation, which leads to the
von Kármán vortex street, is then no longer possible.

In the following chapters, the classical Orr-Sommerfeld stability analysis is
supplemented by treating the perturbation calculation of local wave packet
perturbations for laminar flows and applying this treatment then to turbulent
flows. The perturbation differential equations of the Navier-Stokes equations
are replaced by the time-averaged perturbation differential equations of the
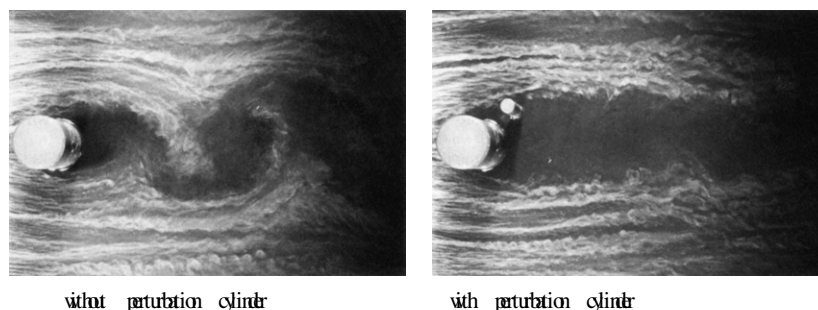Reynolds equations. The mathematical analysis for locating absolutely un-

Fig. 1.4. Flow control with a perturbation cylinder, *P.J. Strykowski* 1990, *H. Oertel*
1994

5

stable regions is the same for both laminar and turbulent flows. This is also valid for the extension to the general perturbation differential equations of compressible flows.

Application of the theory of wave-packet perturbations to the flow past cars and in the design of wings of civil aircraft will show that suitable flow control with the aim of preventing absolutely unstable regions in the flow field leads to a technically useful reduction in drag. In fluidic oscillators the resonator effect of absolute instability can be exploited to generate periodically oscillating perturbations. These can be used in practice, for example, in windsceen washing systems of cars or as periodic switches.

The basics of fluid mechanics and the mathematical details of stability theory, as well as the basics of numerical fluid mechanics, may be found, in supplement to this article, in our textbooks *H. Oertel ed.* Prandtl's Essentials of Fluid Mechanics, 2008, 2009, *H. Oertel, M. Böhle*, Strömungsmechanik 1995, 2009, *E. Laurien, H. Oertel*, Numerische Strömungsmechanik 2009 and *H. Oertel, J. Delfs*, Strömungsmechanische Instabilitäten 1995, 2005.

2   Stability Theory

During the last 120 years, a great deal of ingenuity has been expended, on both mathematical and experimental fronts, on answering the question of how turbulence arises and the role played by linear stability theory of small perturbations. Qualitatively, the transition from the laminar to the turbulent state occurs if the momentum exchange by molecular transport cannot compete sufficiently effectively with the transport due to macroscopic fluctuations in flow velocity. Making use of the ideas of dynamic similarity, *O. Reynolds* 1883, 1894 argued that the transition from the laminar to the turbulent state occurs when a dimensionless parameter exceeds a certain critical value. The Reynolds number is defined as $U_\infty L/\nu$, where U_∞ is a characteristic velocity of the flow, L its characteristic size, and ν the kinematic viscosity of the fluid.

A generic case of instability to consider in a carefully prepared experiment is one in which the perturbations are small. This idea has prompted a vast development of linear stability theory, the theory that calculates the Reynolds number at which laminar motion becomes unstable to small perturbations. Starting with *Lord Rayleigh* in the 1880s, *O. Reynolds* 1883, *W. M. F. Orr* 1907, *A. Sommerfeld* 1908, *G. I. Taylor* 1923, *W. Heisenberg* 1924, *C. C. Lin* 1955, *S. Chandrasekhar* 1961, and others (see, for example, *P. G. Drazin and W. H. Reid* 1981, *H. Oertel and J. Delfs* 1996, 2005 for details) have made lasting contributions to the subject.

Since the instabilities grow only at relatively high Reynolds numbers, or equivalently, at small viscosities, it appears reasonable at first to treat the problem as essentially inviscid. Indeed, inviscid instability is often able to explain certain observations concerning the behavior of fluids with finite viscosity. This turns out to be the case particularly for flows for which the maximum vorticity occurs within the bulk of the fluid rather than on the boundaries.

Inviscid instability yields implausible answers for certain other flows. For instance, the inviscid theory yields the result that the flow between two parallel plates, one of which is stationary while the other moves with finite velocity, called plane Couette flow, is stable at all Reynolds numbers. Experiments, on the other hand, show that the flow does indeed become unstable at some finite Reynolds number on the order of a thousand. This phenomenon is puzzling at first sight because, if a flow is stable in the absence of viscosity, the additional damping provided by viscosity may be thought reasonably to make it even more stable, not less so. However, viscosity plays a role that is not so obvious, as explained by *W. Tollmien* 1929, and more fully by *C. C. Lin* 1955, and can promote instability.

These issues are best explained for the case of a convectively unstable bound-

ary layer on a thin flat plate, for which extensive literature is available. This is an important flow in practice because it will be seen that turbulence often arises within a boundary layer. To study the initial growth of the perturbation in the boundary layer of a viscous fluid, *W. M. F. Orr* 1907 and *A. Sommerfeld* 1908 derived from the Navier–Stokes equations a linear differential equation, the Orr–Sommerfeld equation. The solutions of this equation are of the form shown in Figure 2.1. Inside the neutral curve ($\omega_i = 0$), the two-dimensional wave perturbations are unstable ($\omega_i > 0$), and outside, they are stable ($\omega_i < 0$). In regions of instability, the perturbations grow exponentially with time if they are spatially homogeneous. The perturbations grow exponentially with space if introduced at some point in space and allowed to grow as they propagate, or in both space and time if the perturbations are in the form of a wave packet, which is convectively unstable.

Further investigation shows that a second characteristic layer is formed at the position in the flow where the velocity of the main flow is the same as the phase velocity of the oscillation. In the absence of friction this would lead to singularities in the motion of fluid particles, since they are subject to the same pressure gradient for a very long time. However, if viscosity is postulated in this second layer also, then the disturbance is free from singularities. With the presence of viscosity, the phase displacement of longitudinal motion produces a damping effect, which, in conjunction with the amplification due to the secondary boundary layer, gives a critical value for the Reynolds number. Here the basic physics is only hinted at, but it was the notable achievement of *W. Tollmien* 1929 to carry out the calculation needed to compute the critical Reynolds number.

The so-called *Tollmien–Schlichting waves* are spatially amplified downstream. Via several intermediate states in the transition regime, the state of fully developed turbulence is reached. Above a second critical Reynolds number, plane Tollmien–Schlichting waves initially become unstable to cross-wave perturbations. Downstream, they form the so-called lambda structures with local shear layers in the boundary layer. It is only when these shear layers lose their
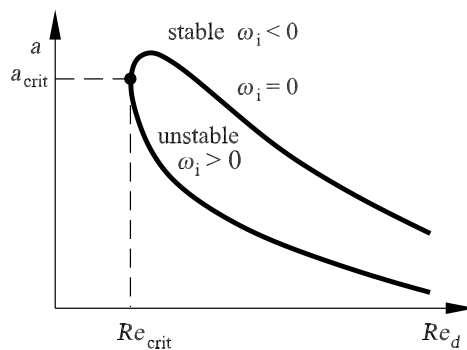

Fig. 2.1. Stability diagram of Tollmien-Schlichting waves in a flat plate boundary layer

8

identity that the turbulent boundary-layer flow is fully developed (see Figure 2.2).

In *three-dimensional boundary layers*, such as those that occur on a swept wing of a civil aircraft, the cross flow along the wing can also lead to further instabilities as well as the Tollmien–Schlichting transition. These *cross-flow instabilities* occur downstream from the stagnation line of the wing. They form traveling waves and a steady vortex pattern along the cross-flow component of the three-dimensional boundary layer. This pattern decays with the same mechanisms as the Tollmien–Schlichting transition and passes over to the turbulent boundary layer close to the stagnation line.

For numerous flow problems, the loss of linear stability of the laminar state is the first step in the transition to turbulence. The next step of the transition process is nonlinear, in which the perturbations grow to a sufficiently large amplitude and the interaction with the basic flow causes them to be exponentially amplified.

The definition of *fluid-mechanical instability* depends on whether one considers *temporal* or *spatial perturbation development*. The flow field is perturbed with a harmonic periodic perturbation wave u' with small amplitude:

$$u'(x, z, t) = \hat{u}(z) \cdot \exp(\mathrm{i} \cdot a \cdot x - \mathrm{i} \cdot \omega \cdot t). \tag{2.1}$$

For a given wavelength $\lambda = 2 \cdot \pi / a$, the laminar initial state is regarded as *temporally unstable* with respect to this wavelength if the flow causes the wave amplitude to be amplified in time ($\mathrm{Im}(\omega(a)) > 0$). If the perturbing wave is damped in time ($\mathrm{Im}(\omega(a)) < 0$), the laminar initial flow is *temporally stable* with respect to the given wavelength. The *temporally neutral* state is the limiting case of a temporally constant perturbation amplitude. Instead of temporal perturbation development, the concept of stability can also be defined with respect to the purely spatial (ω real, a complex), or, more generally, the spatiotemporal (ω, a complex) development of perturbations. In the latter case, the division into so-called absolute and convective instabilities is convenient. A *convective instability* is present when the temporally amplifying perturbation energy moves downstream with the flow. On the other hand, if the perturbation remains in one place, the instability is *absolutely unstable*.
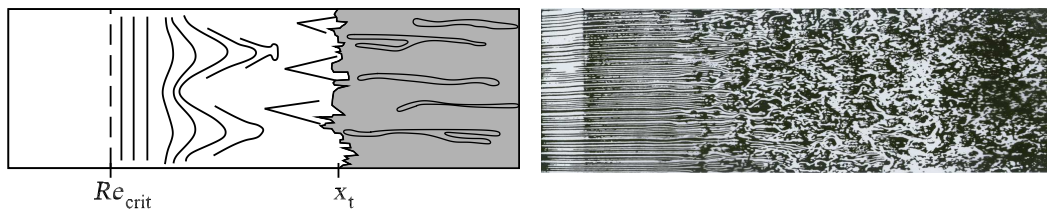

Fig. 2.2. Transition process in a flat plate boundary layer

9

In the mathematical definition of stability, a steady flow state $U_i^0(x, y, z)$ is assumed, which is completely defined by, for example, its dimensionless density distribution ρ_0, temperature distribution T_0, and the three components of the velocity vector (u_0, v_0, w_0) at each spatial position (x, y, z). The state $U_i^0 = (\rho_0, u_0, v_0, w_0, T_0)$ satisfies the fluid-mechanical equations. The question is whether further solutions, that is, additional equilibrium states of the system, exist. In order to be able to answer this question, the flow state U_i^0 is disturbed out of its basic state with a small perturbation $u_i'(x, y, z, t)$. This disturbance must be physically possible; i.e., the new flow state $u_i(x, y, z, t)$ occurring at the time $t = 0$ must satisfy the boundary conditions of the flow problem.

Then:

$$u_i(x, y, z, t) = U_i^0(x, y, z) + u_i'(x, y, z, t). \tag{2.2}$$

The size of the perturbation is introduced with

$$|u_i'| = \int_V |u_i'(x, y, z)^2| \cdot \mathrm{d}V. \tag{2.3}$$

This is a measure of the deviation of the perturbed flow u_i from the basic flow U_i^0 in the entire flow field V. In what follows, the quantity $|u_i'|$ will be called the *perturbation energy* in the flow field.

The basic flow is stable as long as the size of a perturbation remains smaller than a given number ϵ for all times $t \geq 0$:

$$|u_i'|_t < \epsilon \quad \text{with} \qquad t \geq 0, \tag{2.4}$$

for all initial perturbations $u_i'(x, y, z, t = 0)$ with perturbation energy smaller than a constant. Otherwise, the basic flow is unstable. Figure 2.3 shows examples that can be divided into stable and unstable flows by applying the above definition to the temporal behavior of the perturbation energy in the flow. Various initial perturbations, e.g. $u_{i1}'(t = 0)$, $u_{i2}'(t = 0)$, $u_{i3}'(t = 0)$, $u_{i4}'(t = 0)$ are superimposed on the fundamental flow U_i^0. It is noted that, of the infinitely many possible perturbations, there are those excited in unstable flow that then die away over time, such as the perturbation $u_{i3}'(t = 0)$. In general, flows U_i^0 are investigated for *asymptotic stability*, which is then present when any given perturbation dies away over time:
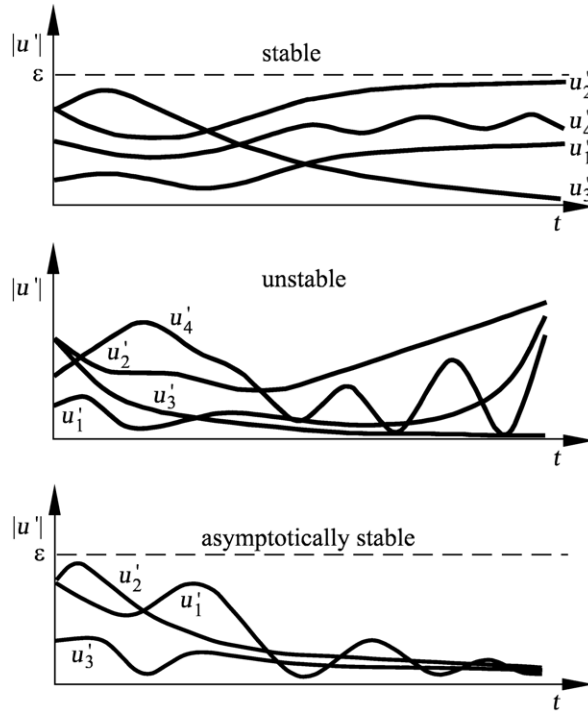
$$\lim_{t \to \infty} |u_i'(t)| = 0. \tag{2.5}$$

Fig. 2.3. The definition of stability

In this case the perturbed system again takes on its temporally asymptotic initial state U_i^0.

Note that the definition of stable and unstable flow is not a statement about the spatiotemporal expansion of unstable perturbations.

To clarify the problem, two unstable basic flows U_i^0 are compared, which have qualitatively different behaviors after the onset of the perturbation. Under the idealizing assumption of freedom from perturbations, a steady wake behind a body in the flow could be generated even for supercritical Reynolds numbers, so that no Kármán vortex street would occur, in contrast to the situation in Figure 2.4. Similarly, an ideal perturbation-free longitudinal flow past a flat plate would be laminar, although unstable, even at supercritical Reynolds numbers.

In the example of the wake flow, if a local perturbation is quickly placed close to the steady wake region of the body at time t_0, over time a Kármán vortex street will form. Such a perturbation in the unstable plate boundary-layer flow behaves qualitatively quite differently. The size of the perturbation also grows here, but the perturbation simultaneously moves downstream, as in the sketch. Clearly, the instability in the wake flow leads to a self-excited oscillation of the system at a fixed position while, in the boundary-layer flow, perturbations at a fixed position vanish over time. Perturbation energy at a fixed position can be observed here only if continuous perturbation energy is introduced upstream,

from outside the system.

In order to be able to make a statement regarding the spatial behavior of the perturbation, a measure for the local size of the perturbations clearly needs to be introduced. To do this, the region of integration V is shrunk to one small region. This shrinking is carried out until the region of integration has been reduced to an infinitesimally small size $\mathrm{d}V$. From (2.3) then

$$\mathrm{d}|u_i'| = |u_i'|^2\mathrm{d}V.$$

Dividing by the volume element $\mathrm{d}V$, a perturbation energy density A is obtained with

$$A(x, y, z, t) = \frac{\mathrm{d}|u_i'|}{\mathrm{d}V} = |u_i'|^2, \tag{2.6}$$

which will be defined in what follows as a measure of the size of the perturbation at position x, y, z at time t. If the perturbation energy density A in an initially perturbation-free unstable flow dies away time-asymptotically at the position where the perturbation was introduced, this flow is *convectively unstable*. Otherwise, the flow is *absolutely unstable*. The wake flow shown in Figure 2.4 is therefore absolutely unstable, while the plate boundary layer is convectively unstable.

2.1   Perturbation Equations

The theoretical treatment of the stability analysis begins with the classical Orr–Sommerfled perturbation differential equations for three-dimensional perturbations in, initially, incompressible boundary-layer flows. The formulation of the stability analysis for the wake flow is carried out analogously.

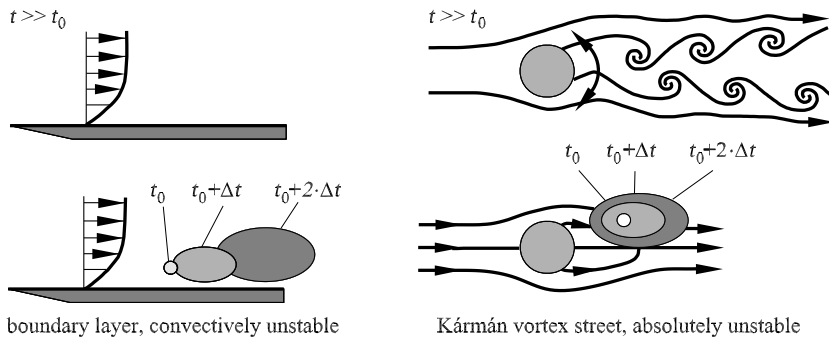In the *plate boundary layer*, the instability occurs with two-dimensional

boundary layer, convectively unstable   Kármán vortex street, absolutely unstable

Fig. 2.4. Expansion of unstable perturbations in convective and absolute instability

Tollmien–Schlichting waves at the critical Reynolds number $\text{Re}_{x,\text{crit}} = 5 \cdot 10^5$ or, with $d = \sqrt{\nu \cdot x / U_\delta}$ at $\text{Re}_{d,\text{crit}} = 302$, which corresponds to the displacement thickness Reynolds number $\text{Re}_{\delta*,\text{crit}} = 520$. The wave fronts are shown in Figure 2.2. The primary perturbation amplitudes grow downstream, and so the flow in this region becomes unstable to three-dimensional *secondary perturbations* (region (2) in Figure 2.5). The vortex lines are deformed in a wavelike shape. Further downstream, the vortex tubes deformed with the vortex lines are stretched and form the *lambda structures* (3). The subsequent decay of these structures and the spatial and temporal irregular appearance of quickly growing *turbulent spots* (4) completes the transition process at position x_t, called the *position of complete transition*. Following this is the developed turbulent state (5). Even fully developed turbulence is not without structure, since longitudinal stripe-shaped regions with greatly reduced downstream components of the velocity (*streaks*) are observed close to the wall. Other structures also exist.

Throughout the entire transition process (1)–(4), there is a significant increase in the thickness of the boundary layer. This is because the ever growing perturbation amplitudes, particularly the vertical oscillations, result in distributing the time average of the downstream momentum more evenly within the boundary layer. The greatest oscillation intensity initially takes place directly at the surface, causing the time-averaged wall shear stress in the transition regime to take on an even higher value than that in the region of full turbulence. Note particularly that the transition described does not take place at one position, but rather over an extended distance $x_{\text{crit}} < x < x_t$.

The unstable primary perturbation (1) of the laminar flow (0) causes lasting change to the flow field only downstream of the critical position x_{crit}. Upstream of this position, the flow remains laminar. If a local perturbation is introduced into the boundary layer at a point $x > x_{\text{crit}}$, the perturbing wave packet expands downstream with a characteristic velocity and simultaneously disintegrates, while the perturbation intensity due to the instability grows. If such an unstable wave packet does not continue to affect the original position of the perturbation, the instability is convectively unstable (see Figure 2.4). Thus, the primary perturbation of the boundary layer is convectively unstable.
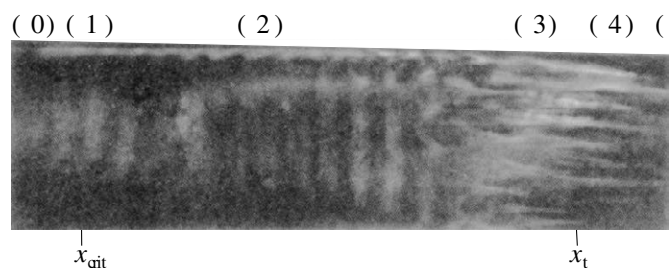

Fig. 2.5. Transition process in the boundary layer of a rotationally symmetric body, *F. N. M. Brown* 1957

The *stability analysis* begins with the determination of the *basic flow*. Usually, it consists of solving the Navier–Stokes or boundary-layer equations by numerical methods, which are described in Chapter 3.

In the stability analysis of boundary layers the increase of the boundary-layer thickness δ in the downstream direction x has to be considered. The flow quantities are therefore not only dependent on the position z in the normal direction on the boundary layer, but also on x and y. Therefore, as well as z, x and y are also inhomogeneous directions.

However, if boundary-layer flows are considered in the large Reynolds number regime, the boundary-layer thickness $\delta(x, y)$ typically varies only moderately (for example, in the case of a plate, $\delta \sim x/\sqrt{\mathrm{Re}_x}$), and so the dependence of the flow velocity on x, y is considerably weaker than that on z.

It is known from experimental results that the dependence of the *perturbations* on the parallel directions x, y is, in contrast to the basic flow, not at all weak. All perturbation velocities are referred to the free stream velocity U_∞, the lengths to δ, and the perturbation pressure to $\rho \cdot U_\infty^2$. The perturbation ansatz for the *incompressible boundary layer* reads

$$
\begin{aligned}
u &= U_\infty \cdot (u_0(\overline{x}, \overline{y}, z) + \epsilon \cdot u'), \\
v &= U_\infty \cdot (v_0(\overline{x}, \overline{y}, z) + \epsilon \cdot v'), \\
w &= U_\infty \cdot (\epsilon \cdot w_0(\overline{x}, \overline{y}, z) + \epsilon \cdot w'), \\
p &= \rho \cdot U_\infty^2 \cdot (p_0(\overline{x}, \overline{y}, z) + \epsilon \cdot p').
\end{aligned}
\tag{2.7}
$$

Here, ϵ is a suitable expansion parameter, chosen for the boundary layer after careful consideration to be $\epsilon = 1/\mathrm{Re}_\delta$. The problem depends on two different length scales, namely, a long scale $\overline{d} = \delta/\epsilon$ and the much shorter scale δ. Because these scales are so different, it is appropriate to formulate the general dependence of the solution on x or y as separate dependencies on both long-scale variables $\overline{x}$ and $\overline{y}$ and on short-scale variables $\tilde{x}$ and $\tilde{y}$. This method is called the *method of multiple scales*. Their relation to the original variable x or y is found as follows:

$$
\begin{aligned}
\tilde{x} &= x, & \overline{x} &= \epsilon \cdot x, \\
\tilde{y} &= y, & \overline{y} &= \epsilon \cdot y.
\end{aligned}
\tag{2.8}
$$

It is understood that all perturbation quantities are functions of both variables, for example $u' = u'(t, x, y, z) = u'(t, \tilde{x}, \overline{x}, \tilde{y}, \overline{y}, z)$. Derivatives with respect to x are then written in the form $\partial u'/\partial x = (\partial u'/\partial \tilde{x}) \cdot \mathrm{d}\tilde{x}/\mathrm{d}x + (\partial u'/\partial \overline{x}) \cdot \mathrm{d}\overline{x}/\mathrm{d}x = \partial u'/\partial \tilde{x} + \epsilon \cdot \partial u'/\partial \overline{x}$.

This yields the linearized *perturbation differential equations*

$$\frac{\partial u'}{\partial x} + \frac{\partial v'}{\partial y} + \frac{\partial w'}{\partial z} = 0, \tag{2.9}$$

$$\frac{\partial u'}{\partial t} + u_0 \cdot \frac{\partial u'}{\partial x} + v_0 \cdot \frac{\partial u'}{\partial y} + \frac{\mathrm{d}u_0}{\mathrm{d}z} \cdot w' + \frac{\partial p'}{\partial x} \tag{2.10}$$

$$- \frac{1}{\mathrm{Re}_d} \cdot \left(\frac{\partial^2 u'}{\partial x^2} + \frac{\partial^2 u'}{\partial y^2} + \frac{\partial^2 u'}{\partial z^2} \right) = 0,$$

$$\frac{\partial v'}{\partial t} + u_0 \cdot \frac{\partial v'}{\partial x} + v_0 \cdot \frac{\partial v'}{\partial y} + \frac{\mathrm{d}v_0}{\mathrm{d}z} \cdot w' + \frac{\partial p'}{\partial y} \tag{2.11}$$

$$- \frac{1}{\mathrm{Re}_d} \cdot \left(\frac{\partial^2 v'}{\partial x^2} + \frac{\partial^2 v'}{\partial y^2} + \frac{\partial^2 v'}{\partial z^2} \right) = 0,$$

$$\frac{\partial w'}{\partial t} + u_0 \cdot \frac{\partial w'}{\partial x} + v_0 \cdot \frac{\partial w'}{\partial y} + \frac{\partial p'}{\partial z} \tag{2.12}$$

$$- \frac{1}{\mathrm{Re}_d} \cdot \left(\frac{\partial^2 w'}{\partial x^2} + \frac{\partial^2 w'}{\partial y^2} + \frac{\partial^2 w'}{\partial z^2} \right) = 0.$$

It is essential that the coefficients, e.g. $u_0(\overline{x}, \overline{y}, z)$, of this homogeneous linear system of partial differential equations in the variables t, $\tilde{x}$, $\tilde{y}$, z depend only on the variables $\overline{x}$, $\overline{y}$, z and not on the small-scale variables $\tilde{x}$, $\tilde{y}$. It can be seen that no explicit derivatives with respect to $\overline{x}$ or $\overline{y}$ appear in (2.9)–(2.12). Within the framework of the above approximation, the solution of the system of differential equations is therefore only algebraically dependent on the spatial variables $\overline{x}$, $\overline{y}$ and not differentially dependent. This stability analysis is then called a *local stability analysis*. The constant basic solution with respect to the short-scale parallel coordinates $\tilde{x}$, $\tilde{y}$ is given at the fixed selected position $\overline{x}$, $\overline{y}$, and the stability analysis is carried out locally here. It is also noted that the perturbation differential equation is homogeneous in t, $\tilde{x}$, and $\tilde{y}$.

In deriving the perturbation differential equations, the dependence on the normal component w_0 of the basic flow drops away. This is called the *parallel flow assumption*.

The perturbations satisfy the *boundary conditions*

$$u'(x, y, z = z_{\mathrm{w}}, t) = v'(x, y, z = z_{\mathrm{w}}, t) = w'(x, y, z = z_{\mathrm{w}}, t) = 0, \tag{2.13}$$

at the wall $z = z_{\mathrm{w}}$, and additionally, the far-field boundary conditions

$$v'(x, y, z \to \infty, t) = 0, \qquad p'(x, y, z \to \infty, t) = 0. \tag{2.14}$$

The system of perturbation differential equations (2.9)–(2.12) is homogeneous in $\tilde{x}$, $\tilde{y}$, and t. A separation trial solution (wave ansatz) can be carried out

$$
\begin{pmatrix}
\tilde{u}'(\tilde{x},\tilde{y},z,t;\overline{x},\overline{y}) \\
\tilde{v}'(\tilde{x},\tilde{y},z,t;\overline{x},\overline{y}) \\
\tilde{w}'(\tilde{x},\tilde{y},z,t;\overline{x},\overline{y}) \\
\tilde{p}'(\tilde{x},\tilde{y},z,t;\overline{x},\overline{y})
\end{pmatrix}
= \mathrm{F}_x(\tilde{x};\overline{x},\overline{y})\cdot \mathrm{F}_y(\tilde{y};\overline{x},\overline{y})\cdot \mathrm{F}_t(t;\overline{x},\overline{y})\cdot
\begin{pmatrix}
\hat{u}(z;\overline{x},\overline{y}) \\
\hat{v}(z;\overline{x},\overline{y}) \\
\hat{w}(z;\overline{x},\overline{y}) \\
\hat{p}(z;\overline{x},\overline{y})
\end{pmatrix},
\quad (2.15)
$$

because the boundary conditions depend only on z. Inserting (2.15) into the continuity equation (2.9), then

$$
\left(\frac{1}{\mathrm{F}_x}\cdot\frac{\mathrm{dF}_x}{\mathrm{d}\tilde{x}}\right)\cdot\hat{u} + \frac{\mathrm{d}\hat{w}}{\mathrm{d}z} + \left(\frac{1}{\mathrm{F}_y}\frac{\mathrm{dF}_y}{\mathrm{d}\tilde{y}}\right)\cdot\hat{v} = 0,
$$

where the two terms on the right are independent of $\tilde{x}$, and the two terms on the left are independent of $\tilde{y}$, so that the expressions in parentheses are each constants with respect to $\tilde{x}$ and $\tilde{y}$. The same procedure can be carried out with the function F_t. Inserting the separation ansatz into equation (2.12), then

$$
\frac{1}{\mathrm{F}_x}\cdot\frac{\mathrm{dF}_x}{\mathrm{d}\tilde{x}} = \mathrm{i}\cdot a(\overline{x},\overline{y}), \quad
\frac{1}{\mathrm{F}_y}\cdot\frac{\mathrm{dF}_y}{\mathrm{d}\tilde{y}} = \mathrm{i}\cdot b(\overline{x},\overline{y}), \quad
\frac{1}{\mathrm{F}_t}\cdot\frac{\mathrm{dF}_t}{\mathrm{d}t} = -\mathrm{i}\cdot \omega(\overline{x},\overline{y}),
$$

where the three separation parameters a, b, and ω have been introduced, and these are still functions of the long-scale variables. From the equations for F_x, F_y, and F_t it follows that

$$
\begin{pmatrix}
\tilde{u}'(\tilde{x},\tilde{y},z,t) \\
\tilde{v}'(\tilde{x},\tilde{y},z,t) \\
\tilde{w}'(\tilde{x},\tilde{y},z,t) \\
\tilde{p}'(\tilde{x},\tilde{y},z,t)
\end{pmatrix}
= \exp(\mathrm{i}\cdot a\cdot\tilde{x} + \mathrm{i}\cdot b\cdot\tilde{y} - \mathrm{i}\cdot\omega\cdot t)
\begin{pmatrix}
\hat{u}(z) \\
\hat{v}(z) \\
\hat{w}(z) \\
\hat{p}(z)
\end{pmatrix},
\quad (2.16)
$$

where the dependence of the functions on $\overline{x}$ and $\overline{y}$ has not been indicated here. The exponent $a(\overline{x},\overline{y})\cdot\tilde{x} + b(\overline{x},\overline{y})\cdot\tilde{y} - \omega(\overline{x},\overline{y})\cdot t$ is also called the *phase*. The separation parameters a, b, and ω are initially any, generally complex, numbers.

Inserting the wave ansatz (2.16) into the system of equations (2.9)–(2.12), then

$$a \cdot \hat{u} + b \cdot \hat{v} = \mathrm{i} \cdot \frac{\mathrm{d}\hat{w}}{\mathrm{d}z}, \tag{2.17}$$

$$(a \cdot u_0 + b \cdot v_0 - \omega) \cdot \hat{u} - \mathrm{i} \cdot \frac{\mathrm{d}u_0}{\mathrm{d}z} \cdot \hat{w} = -a \cdot \hat{p} + \frac{i}{\mathrm{Re}_d} \cdot \left(a^2 + b^2 - \frac{\mathrm{d}^2}{\mathrm{d}z^2} \right) \hat{u}, \tag{2.18}$$

$$(a \cdot u_0 + b \cdot v_0 - \omega) \cdot \hat{v} - \mathrm{i} \cdot \frac{\mathrm{d}v_0}{\mathrm{d}z} \cdot \hat{w} = b \cdot \hat{p} + \frac{i}{\mathrm{Re}_d} \cdot \left(a^2 + b^2 - \frac{\mathrm{d}^2}{\mathrm{d}z^2} \right) \hat{v}, \tag{2.19}$$

$$(a \cdot u_0 + b \cdot v_0 - \omega) \cdot \hat{w} = \mathrm{i} \cdot \frac{\mathrm{d}\hat{p}}{\mathrm{d}z} + \frac{i}{\mathrm{Re}_d} \cdot \left(a^2 + b^2 - \frac{\mathrm{d}^2}{\mathrm{d}z^2} \right) \hat{w}. \tag{2.20}$$

With the boundary conditions (2.13) and (2.14),

$$\hat{u}(z = z_{\mathrm{w}}) = \hat{v}(z = z_{\mathrm{w}}) = 0 \ , \qquad \hat{w}(z = z_{\mathrm{w}}) = 0, \tag{2.21}$$

$$\hat{v}_i(z \to \infty) = 0 \ , \qquad \hat{p}(z \to \infty) = 0, \tag{2.22}$$

where the eigenvalue problem is formulated for the *wave instabilities*. It is a linear system of homogeneous differential equations that contains the four parameters Re_d, a, b, and ω. The Reynolds number is given as a real number. Apart from the trivial solution, the system of equations is solvable only for certain a, b, and ω. This defines a mutual relation among these three relations, called the *dispersion relation*:

$$D(a, b, \omega) = 0. \tag{2.23}$$

In the *eigenvalue problem* described, two of the quantities a, b, and ω are given, and the remaining one is to be computed as an eigenvalue from the equations.

The *stability analysis* is concerned with the variation of the perturbation amplitude $|u_i'|$ of a perturbation u_i' introduced into a flow U_i^0. As seen in the beginning of the section, the stability is defined via the temporal amplification of the perturbation amplitudes. In boundary layers the perturbations are represented as waves that run along the directions x and y:

$$u_i'(x, y, z, t) = u_i(z) \cdot \exp(\mathrm{i} \cdot a \cdot x + \mathrm{i} \cdot b \cdot y - \mathrm{i} \cdot \omega \cdot t). \tag{2.24}$$

The tilde above the x and y has again been left out for clarity. According to the definition of stability, an eigenform is given by the wave number components a and b, and the associated value $\omega = \omega_r + \mathrm{i} \cdot \omega_{\mathrm{i}}$ is computed from the eigenvalue problem. If spatially periodic waves (i.e. real $a = a_r$ and $b = b_r$) are given, the problem is then a *temporal stability analysis*. Since the system can develop further only in the positive time direction, a wave perturbation with given $a = a_r$ and $b = b_r$ is then temporally unstable only if its amplitude is amplified in time, i.e. if $\omega_{\mathrm{i}} > 0$. Here ω_{i} is the *temporal amplification rate*. A perturbation for which $\omega_{\mathrm{i}} = 0$ holds is called an indifferent or neutral perturbation. The

quantity ω may also be given and the associated eigenform (represented by a and b) computed. The problem becomes one of *spatial stability analysis* if $\omega = \omega_r$ is given as a real value (i.e. consideration of all possible waves with a given frequency), and, for example, a is computed for a given b. The real part a_r of the computed number a is then the wave number, and the imaginary part a_i is a measure for the spatial amplification in x. An explicit definition for spatial amplification is clearly obtained only when a direction of consideration is given. Let it be represented by the unit vector $\mathbf{e}_\phi = \mathbf{e}_x \cdot \cos(\phi) + \mathbf{e}_y \cdot \sin(\phi)$ (Figure 2.6).

The variation in the amplitude $|u'_i| = |\hat{u}_i| \cdot \exp(-a_i \cdot x - b_i \cdot y + \omega_i \cdot t)$ of the wave is determined along the given direction ϕ as $\mathrm{d}|u'_i|/\mathrm{d}x_\phi = \mathbf{e}_\phi \cdot \nabla|u'_i|$. It is found that $\mathrm{d}|u'_i|/\mathrm{d}x_\phi = -(a_i \cdot \cos(\phi) + b_i \cdot \sin(\phi)) \cdot |u'_i|$. The amplitude grows along $\mathbf{e}_\phi$ if $\mathrm{d}|u'_i|/\mathrm{d}x_\phi$ is positive. The wave is amplified with respect to the direction ϕ if

$$a_i \cdot \cos(\phi) + b_i \cdot \sin(\phi) < 0.$$

The quantities a_i and b_i are also called *spatial amplification rates*. It is noted that the necessity to specify a direction ϕ is to a certain degree arbitrary. For this reason it is necessary to check whether the wave with the phase velocity vector $c_i = (c_x, c_y, 0) = \omega_r/(a_r^2 + b_r^2) \cdot (a_r, b_r, 0)$ moves in the direction of increasing amplitude. The direction of consideration $\mathbf{e}_\phi$ is allowed to lie along the direction of motion of the wave $\mathbf{e}_{\mathrm{crit}} = (a_r, b_r, 0) \cdot \mathrm{sgn}(\omega_r)/\sqrt{a_r^2 + b_r^2}$, where $\mathrm{sgn}(\omega_r) = \omega_r/|\omega_r|$ (cf. Figure 2.6). A temporally periodic wave experiences an increase in amplitude along its direction of motion if

$$\omega_r \cdot (a_r \cdot a_i + b_r \cdot b_i) < 0.$$

A two-dimensional wave ($b = 0$) can be called spatially amplified if for $\omega_r > 0$, the imaginary part satisfies $a_i < 0$. However, which wave actually contributes to the spatial amplification of perturbations can be answered precisely within the framework of the concept of the stability analysis of local perturbations
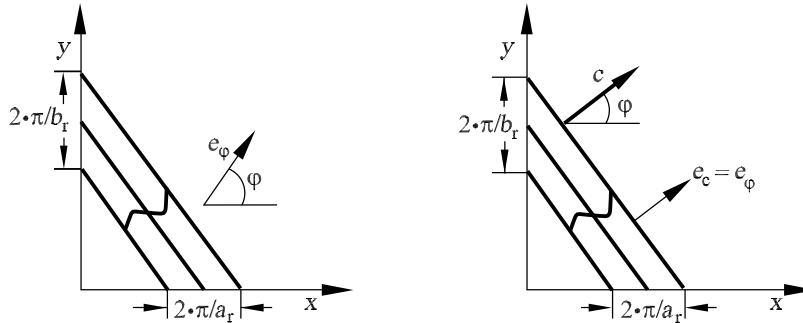

Fig. 2.6. Expansion of a wave perturbation

18

for convective instabilities.

The eigenvalue problem can deliver either a for a given $b = b_r + \mathrm{i} \cdot b_r$ and $\omega = \omega_r$ or b for a given $a = a_r + \mathrm{i} \cdot a_r$ and $\omega = \omega_r$. Rather than specifying a complex wave number, it is clearer in the spatial analysis to determine, for example, the amplification $\phi = 1/\tan(b_\mathrm{i}/a_\mathrm{i})$. This corresponds to determining the ratio of the imaginary parts a_i and b_i of a and b.

It is noted that the temporal stability analysis is simpler to carry out than the spatial stability analysis. In the eigenvalue problem (2.17)–(2.20), ω appears only linearly, whereas a and b appear quadratically. The solution of a quadratic eigenvalue problem requires considerably more computational effort than the solution of a linear problem. Therefore, a method by which temporal amplifications could be transformed into spatial amplifications was examined. Such a relation was given by *M. Gaster* 1962 for $b = 0$. The transformation of the temporal amplification ω_i of a spatially periodic wave with given real wave number a_r and associated frequency ω_r to a temporally periodic wave (i.e. $\omega_\mathrm{i} = 0$) with the same wave number a_r and frequency ω_r is performed using

$$
a_\mathrm{i} \approx -\frac{1}{\dfrac{\partial \omega_r}{\partial a_r}} \cdot \omega_\mathrm{i}.
$$

This yields the spatial amplification of the wave from the temporal amplification of the associated wave using the *group velocity* $\partial \omega_r / \partial a_r$. The above relation is called the *Gaster transformation*. It is valid only for small amplification rates a_i, ω_i, since it is based on a Taylor expansion of the dispersion relation $D(a, \omega) = 0$ about the neutral state $a_\mathrm{i} = 0$, $\omega_\mathrm{i} = 0$.

The system of perturbation differential equations (2.17)–(2.20) has a remarkable property. It can be summarized by a single fourth-order differential equation that represents an extension to the Orr–Sommerfeld equation for obliquely traveling waves, with $\hat{u}$, $\hat{v}$, and $\hat{p}$ eliminated. Using the *Squire transformation*

$$
a_\varphi \cdot u_{0,\varphi} = a \cdot u_0 + b \cdot v_0, \qquad a_\varphi^2 = a^2 + b^2,
$$

which represents a coordination rotation in the direction of expansion, the *Orr–Sommerfeld equation* is obtained

$$\left[(a_\varphi \cdot u_{0,\varphi} - \omega) \cdot \left(\frac{\mathrm{d}^2}{\mathrm{d}z^2} - a_\varphi^2 \right) - a_\varphi \cdot \frac{\mathrm{d}^2 u_{0,\varphi}}{\mathrm{d}z^2} \right. \tag{2.25}$$

$$\left. + \; \mathrm{i} \cdot \frac{1}{\mathrm{Re}_d} \cdot \left(\frac{\mathrm{d}^2}{\mathrm{d}z^2} - a_\varphi^2 \right)^2 \right] \hat{w} = 0,$$

with the following boundary conditions for $\hat{w}$:

$$\hat{w} = 0, \qquad \frac{\mathrm{d}\hat{w}}{\mathrm{d}z} = 0 \quad \text{for} \qquad z = z_{\mathrm{w}}, \tag{2.26}$$

$$\hat{w} = 0, \qquad \frac{\mathrm{d}\hat{w}}{\mathrm{d}z} = 0 \quad \text{for} \qquad z \to \infty. \tag{2.27}$$

If in equation (2.25), a_φ is replaced by a, and $a_\varphi \cdot u_{0,\varphi}$ by $a \cdot u_0$, this represents the two-dimensional case. In Figure 2.7, the stability diagram has been supplemented by a typical eigenfunction. It is pointed out that the vertical component $|\hat{w}|$ of the perturbation velocity has been enlarged 10 times. It is very small compared to the amplitude of the downstream component $|\hat{u}|$. The largest perturbation amplitudes for $\hat{u}$ are assumed to be largest directly at the wall. Now, the perturbations have not died away when the boundary-layer thickness is reached. They extend far out of the boundary layer. The sharp minimum of $|\hat{u}|$ at a distance from the wall of about 2/3 of the boundary-layer thickness δ is only a consequence of forming the magnitude of $\hat{u}$. In fact, the function $\hat{u}$ passes through zero at this position, a fact that is related to a phase change of the wave of 180°.

In three-dimensional boundary layers, *Tollmien–Schlichting waves* occur and also, because of the cross-flow component of the basic profile, do the *cross-flow instabilities*. Which waves have cross-flow instabilities is shown in the wave number diagram of Figure 2.8, using the instability region for fixed Reynolds number. Tollmien–Schlichting waves occur downstream only when the critical Reynolds number is exceeded. Note, however, that the Reynolds number in this regime is very small, and therefore there is a strong viscous effect, in this
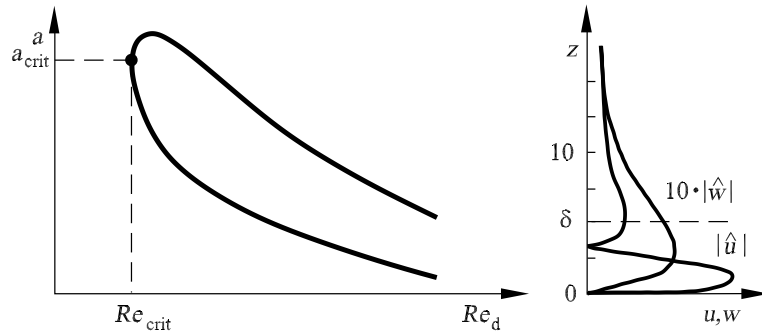

Fig. 2.7. Stability diagram for real a, $b = 0$ for the flat plate and eigenfunction for $a = 0,16$, $b = 0$, $\mathrm{Re}_{d,\mathrm{crit}} = 302$
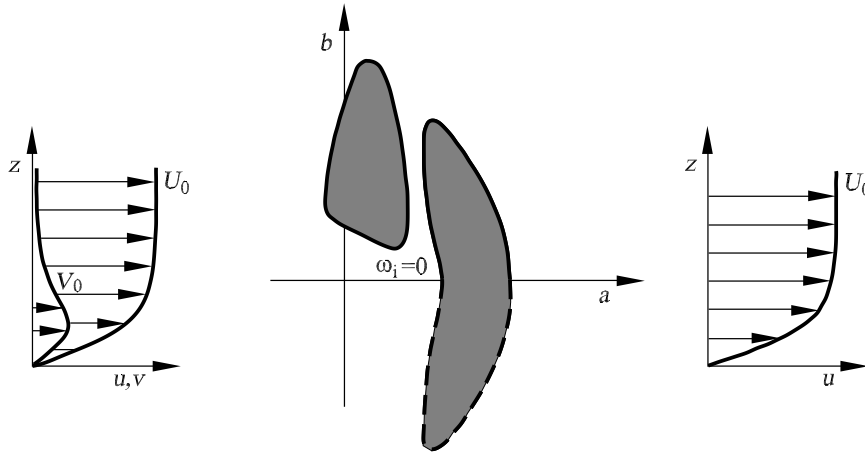
Fig. 2.8. Unstable waves for boundary layers with and without cross-flow component $V_i^0(z)$

case damping. For comparison, an instability region for the two-dimensional velocity profile $U_0(z)$ is also included. It is typical that instability waves with considerably larger king pin inclinations $\varphi = 1/\tan(b/a)$ exist than in the three-dimensional boundary layer. Because of its characteristic form, the neutral curve $\omega_i = 0$ in the wave number diagram for two-dimensional boundary layers is also called a kidney curve.

Equally typical for cross-flow instabilities is the appearance of standing perturbation vortices. Since the angular frequency of these standing perturbation waves is $\omega_r = 0$, they are also called *0-Hertz modes*. Their wave normal is almost perpendicular to the downstream direction at the edge of the boundary layer. These standing waves can be made visible in experiment, with, for example, smoke introduced into the flow, and then have a clear structure in
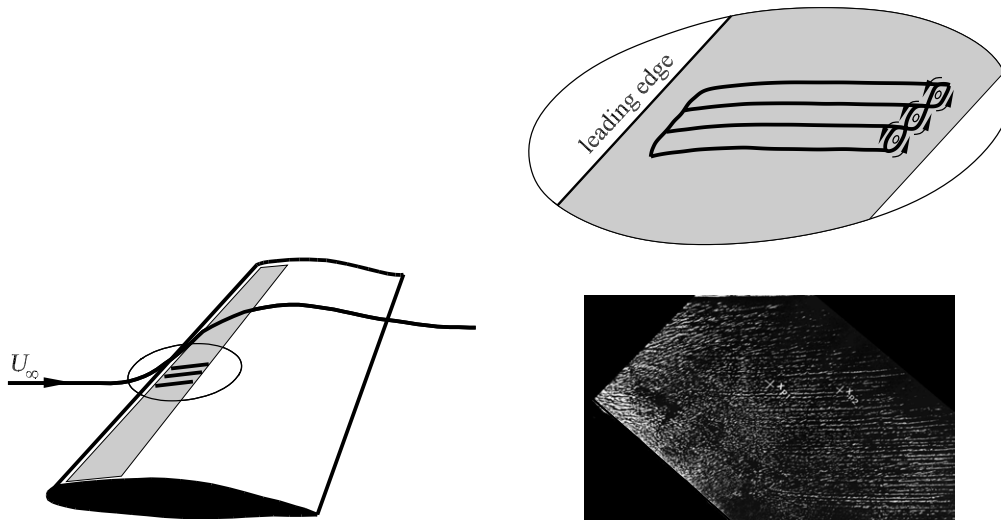
Fig. 2.9. Unstable cross-flow vortex in a three-dimensional boundary layer, *Y. Kohama* 1989

the downstream direction (see Figure 2.9). The perturbation waves that are amplified the most are, however, generally unsteady and travel at a large angle φ transverse to the downstream direction x.

2.2 Local Perturbations

Now that the classical Orr-Sommerfeld stability analysis has been developed for *harmonic* three-dimensional perturbation waves, the stability theory that is relevant in practice is derived, namely the stability theory of *local perturbations* of the compressible boundary-layer flow. Three-dimensional compressible boundary layers occur, for example, on transonic wings of civil aircraft and on turbine blades.

Local perturbations arise, for example, because of roughness on the surface. Figure 2.10 shows a sketch of the amplification of a wave packet perturbation that is swept downstream in the boundary layer. Of interest here is the angular range encompassed by the unstable perturbation. In accordance with the descriptions in Chapter 1, the boundary lines of the perturbation region are called characteristics of the inviscid flow. If, with increasing time, the local perturbation leaves the position at which it arose, as shown in Figure 2.11, as for boundary layers, it is *convectively unstable.* However, if the perturbation increases further at the position at which it arose, it is known, as in the wake flow, as an *absolutely unstable* wave-packet perturbation.

The starting point of the perturbation calculation for local wave-packet perturbations in compressible flows is the conservation equations for mass, momentum and energy:
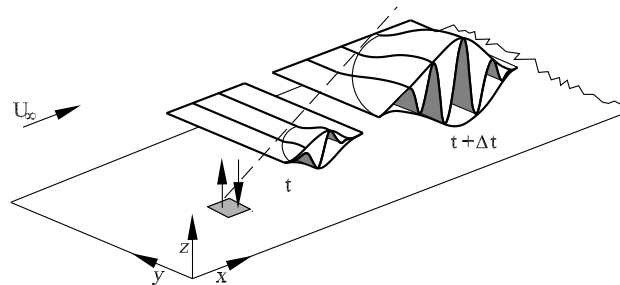

Fig. 2.10. Local perturbation of the basic flow through initially point-sized pulse excitation of a three-dimensional wave packet
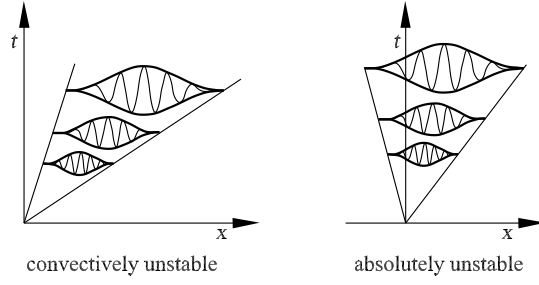
22

convectively unstable   absolutely unstable

Fig. 2.11. Path–time diagram of unstable wave packets

$$\frac{\partial \rho}{\partial t} + \frac{\partial (\rho u_k)}{\partial x_k} = 0, \tag{2.28}$$

$$\rho \left(\frac{\partial u_i}{\partial t} + u_k \frac{\partial u_i}{\partial x_k} \right) = \frac{1}{\kappa M_\infty^2} \frac{\partial p}{\partial x_i} + \frac{1}{Re_L} \frac{\partial \tau_{ik}}{\partial x_k}, \tag{2.29}$$

$$\rho \left(\frac{\partial e}{\partial t} + u_k \frac{\partial e}{\partial x_k} \right) = -(\kappa - 1)p \frac{\partial u_k}{\partial x_k} \tag{2.30}$$

$$+ \frac{\kappa}{Re_L} \left((\kappa - 1) M_\infty \tau_{ik} \frac{\partial u_i}{\partial x_k} - \frac{1}{Pr} \frac{\partial q_k}{\partial x_k} \right),$$

with the velocity vector u_i, the pressure p and the density ρ in dimensionless notation. These are extended by the thermodynamic equations of state for the specific internal energy e and the pressure p as dependents on the temperature T:

$$e = e(T, p), \qquad p = p(T, \rho). \tag{2.31}$$

The shear stress component τ_{ik} is calculated with the Newton shear stress ansatz and the Stokes hypothesis as:

$$\tau_{ik} = \mu(T, p) \left(\frac{\partial u_i}{\partial x_k} + \frac{\partial u_k}{\partial x_i} - \frac{2}{3} \frac{\partial u_j}{\partial x_j} \delta_{ik} \right), \tag{2.32}$$

where μ describes the dynamic viscosity. To calculate the heat flux term q_k, the Fourier law of heat conduction with the thermal conductivity λ is used:

$$q_k = -\lambda(T, p) \frac{\partial T}{\partial x_k}. \tag{2.33}$$

All quantities are referred to the associated value in the unperturbed approach flow, the coordinates are made dimensionless with the characteristic length L of the flow problem and the time is referred to L/U_∞. In doing this the following dimensionless characteristic numbers appear: the Reynolds number $Re_L = \rho_\infty U_\infty L / \mu_\infty$, the Prandtl number $Pr = c_p \mu_\infty / \lambda_\infty$, the Mach number $M_\infty = U_\infty / a_\infty$ with the speed of sound in the free stream a_∞, as well as the

23

ratio of the specific heat capacities at constant pressure c_p and at constant volume c_v, $\kappa = c_p/c_v$.

The differential equations are made complete by taking account of the initial and boundary conditions. For boundary-layer flow and wake flow, the no slip condition on the body and a temperature boundary condition hold as well as the unperturbed free stream at infinity. In the framework of a perturbation calculation, solution ansatz is made for the local perturbations, e.g. for the velocity vector:

$$u_i(x,y,z,t) = U_i^0(z) + u_i'(x,y,z,t). \tag{2.34}$$

Here U_i^0 denotes a steady solution of the Navier Stokes equations (2.28) – (2.31) and describes the locally observed velocity profile at the location of the perturbation analysis. Neglecting nonlinear terms in the perturbation quantities, the following differential equations hold for the perturbation quantities u_i', T', ρ':

$$L[(u_i', T', \rho')(x,y,z,t)] = G(x,y,z,t), \tag{2.35}$$

where L denotes the linear differential operator obtained by linearization around the steady state solution and G is the given perturbation function, which may be, for example, a spatio-temporal pulse excitation. For $G = 0$, from (2.35) the well-known eigenvalue problem of primary stability theory is obtained, which corresponds for incompressible flows to the Orr-Sommerfeld equation of Section 2.1. The concrete shape of $L = {}^t(L_\mu, L_u, L_v, L_w, L_T)$ may be found in *H. Oertel, J. Delfs* 1995. For the perturbation waves, either harmonic waves are assumed

$$u_i'(x,y,z,t) = \hat{u}_i(z)e^{i(ax+by-\omega t)} \tag{2.36}$$

or else wave packets

$$u_i'(a,b,z,\omega) = \int\limits_0^\infty \left[\int\limits_{-\infty}^\infty \int\limits_{-\infty}^\infty u_i'(x,y,z,t)e^{-i(ax+by)} \, \mathrm{d}x \, \mathrm{d}y \right] e^{i\omega t} \, \mathrm{d}t. \tag{2.37}$$

In the case of a complex a (or b), this is known as a spatially amplified perturbation wave. If ω is complex, the perturbation waves are amplified in time. If a (or b) and ω are complex, then, in accordance with the definition of flow regions for temporally and spatially amplified waves, the flow at the location of consideration is absolutely unstable. The mathematical analysis of the development in time and space of wave packets was developed in the 1950s by *R. J. Briggs* 1964 and *A. Bers* 1973 for stability problems in plasma physics.

The wave-packet method has been further developed for the subdivision of regions of viscous flows and has been carried over in general in the framework of such flow calcuations to laminar and turbulent flows. The mathematical details may be found in *H. Oertel, J. Delfs* 1995.

Figure 2.12 provides an introduction to the procedure for the mathematical analysis. It plots the temporal rates of amplification ω_i against the angular frequency ω_r of the wave-packet perturbation and the spatial rates of amplification a_i against the wave number a_r for a given direction of expansion $\varphi = \tan^{-1}(a_r/b_r)$ of the perturbation wave. The mathematical analysis shows that the inverse transform of the wave-packet perturbations to real space can be written in the form

$$u_i'(x,y,z,t) = \int\limits_{-\infty+i\sigma}^{\infty+i\sigma} \left[\int\limits_{-\infty}^{\infty} \int\limits_{-\infty}^{\infty} \frac{Z(a,b,z,\omega)}{D(a,b,\omega)} e^{i(ax+by)} \, \mathrm{d}a \, \mathrm{d}b \right] e^{-i\omega t} \, \mathrm{d}\omega. \quad (2.38)$$

The inverse transform depends only on the roots of the dispersion relation $D(a,b,\omega)$ that corresponds to the perturbation differential equation. Accordingly, for the parts of the wave with a given region of expansion φ in the wave packet, the associated value a_i may be plotted against the wave number a_r for $D = 0$ for positive rates of amplification in time ω_i. As the value ω_i is reduced (second figure, Figure 2.12), without changing the solution (2.38), both
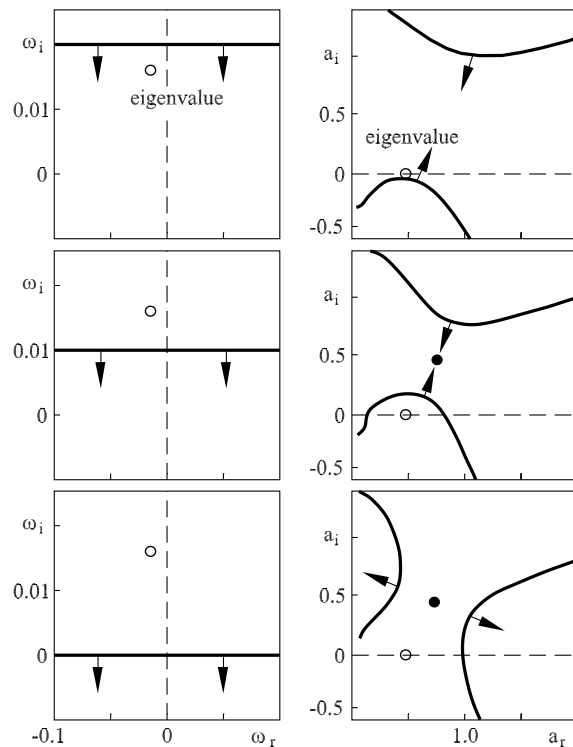

Fig. 2.12. Temporal and spatial rates of amplification ω_i and a_i for the dispersion relation $D = 0$

branches of $a_i(a_r)$ move towards each other. If, as $\omega_i > 0$ is further reduced, they form a double root, i.e. a *saddle point*, the flow field is *absolutely unstable* in respect of the direction φ. At the saddle point the group velocity component of the perturbation wave in the direction φ is $(\frac{\partial \omega}{\partial a}, \frac{\partial \omega}{\partial b})(\sin \varphi, \cos \varphi)^T = 0$. If this saddle point is not found as ω_i is reduced, the flow is convectively unstable in respect of φ.

For incompressible flows, the perturbation differential equations of local wave packets are simpler. The source of perturbation consists of a perturbation volume flux G_ρ to describe local blowing or sucking, and the perturbation force vector $G_i = {}^t(G_u, G_v, G_w)$ as shown in Figure 2.10:

$$\frac{\partial(U_k^0 + \varepsilon u_k')}{\partial x_k} = \varepsilon G_\rho,$$

$$\frac{\partial(U_i^0 + \varepsilon u_i')}{\partial t} + (U_k^0 + \varepsilon u_k')\frac{\partial(U_i^0 + \varepsilon u_i')}{\partial x_k} \tag{2.39}$$

$$+ \frac{\partial(p_0 + \varepsilon p')}{\partial x_i} - Re_d^{-1}\frac{\partial^2(U_i^0 + \varepsilon u_i')}{\partial x_k{}^2} = \varepsilon G_i.$$

The perturbation vector functions $G_\rho(t, x, y, z)$, $G_i(t, x, y, z)$ are nonzero only in a spatially limited region, e.g. $((G_\rho, G_i) = g_t(t)\delta(x)\delta(y)(f_{z\rho}(z), f_{zi}(z))$ for an x-y spatial perturbation. Differentiating (2.39) with respect to ε and then setting it to zero $\varepsilon \to 0$, the following *system of inhomogeneous perturbation differential equations* is obtained:

$$\frac{\partial u_k'}{\partial x_k} = G_\rho, \tag{2.40}$$

$$\frac{\partial u_i'}{\partial t} + U_k^0\frac{\partial u_i'}{\partial x_k} + u_k'\frac{\partial U_i^0}{\partial x_k} + \frac{\partial p'}{\partial x_i} - Re_d^{-1}\frac{\partial^2 u_i'}{\partial x_k{}^2} = G_i.$$

As with the derivation of the Orr-Sommerfeld equation, after elimination a fourth-order differential equation for the wall normal components $w'(t, x, y, z)$ of the perturbation response can be stated:

$$L[w'] = G, \tag{2.41}$$

where $L := (\frac{\partial}{\partial t} + U_k^0\frac{\partial}{\partial x_k} - Re_d^{-1}\frac{\partial^2}{\partial x_k{}^2})\frac{\partial^2}{\partial x_k{}^2} - \frac{d^2 U_k^0}{dz^2}\frac{\partial}{\partial x_k}$ is the linear differential expression that respresents the left-hand side of the Orr-Sommerfeld equation and which acts on w'. The perturbation term G is found as a consequence of transformations from G_ρ and the components G_i to $G = (\frac{\partial}{\partial t} + U_k^0\frac{\partial}{\partial x_k} - Re_d^{-1}\frac{\partial^2}{\partial x_k{}^2})\frac{\partial G_\rho}{\partial z} + \frac{d^2 U_k^0}{dz^2}\frac{\partial}{\partial x_k}G_\rho + \frac{\partial^2 G_w}{\partial x_k{}^2} - \frac{\partial G_k}{\partial x_k}$. For $G = 0$, i.e. with no perturbation in the field, (2.41) becomes the Orr-Sommerfeld equation, complemented by

problem-specific linear boundary conditions and a compatible initial condition $w'_0(x, y, z) = w'(t = 0, x, y, z)$. Typically only such cases where the flow is perturbation free for time $t < 0$ are considered, i.e $w'_0(x, y, z) = 0$. The aim is to compute the time-asymptotic solution of this *initial-boundary value problem*.

2.3   Perturbations of Turbulent Flows

For *turbulent flows* the mathematical analysis to determine the absolutely unstable flow regions is the same. Here the starting point is the Favre-averaged Reynolds equations:

$$\frac{\partial \bar{\rho}}{\partial t} + \frac{\partial (\bar{\rho} \tilde{u}_k)}{\partial x_k} = 0, \tag{2.42}$$

$$\bar{\rho} \left(\frac{\partial \tilde{u}_i}{\partial t} + \tilde{u}_k \frac{\partial \tilde{u}_i}{\partial x_k} \right) = -\frac{1}{\kappa M_\infty^2} \frac{\partial \bar{p}}{\partial x_i} + \frac{1}{Re_L} \frac{\partial \tilde{\tau}_{ik}}{\partial x_k} + R_i^u, \tag{2.43}$$

$$\bar{\rho} \left(\frac{\partial \tilde{e}}{\partial t} + \bar{u}_k \frac{\partial \tilde{e}}{\partial x_k} \right) = -(\kappa - 1)\bar{p} \frac{\partial \tilde{u}_k}{\partial x_k} \tag{2.44}$$

$$+ \frac{\kappa}{Re_L} \left((\kappa - 1) M_\infty^2 \tilde{\tau}_{ik} \frac{\partial \tilde{u}_i}{\partial x_k} - \frac{1}{Pr} \frac{\partial \tilde{q}_k}{\partial x_k} \right) + R^e,$$

$$R_i^u = \frac{\partial}{\partial x_k} \left(-\bar{\rho} (\widetilde{u_i'' u_j''}) + \frac{1}{Re_L} \overline{\tau_{ik}''} \right),$$

$$R^e = -\kappa \left(\frac{\partial \bar{\rho} (\widetilde{T'' u_k''})}{\partial x_k} + (\kappa - 1) M_\infty^2 \bar{\rho} (\widetilde{u_i'' u_j''}) \frac{\partial \tilde{u}_i}{\partial x_k} \right)$$

$$+ \frac{\kappa(\kappa - 1) M_\infty^2}{Re_L} \left(\overline{\tau_{ik}''} \frac{\partial \bar{u}_i}{\partial x_k} + \frac{\partial (\overline{\tau_{ik} u_i''})}{\partial x_k} \right) - \frac{\kappa}{Re_L Pr} \frac{\partial \overline{q_k''}}{\partial x_k}.$$

A quantity with a bar over it $\bar{f}$ denotes in each case the time averaged value $\bar{f}(t) = T_m^{-1} \int_0^{T_m} f(t + \tau) \, d\tau$ of the function f. The quantities $\tilde{u}_i = \overline{\rho u_i} / \bar{\rho}$ and $\tilde{T} = \overline{\rho T} / \bar{\rho}$ are the Favre-averaged velocity and temperature. The Favre-averaged fluctuations are by definition $u_i'' = u_i - \tilde{u}_i$ and $T'' = T - \tilde{T}$, and the usual time fluctuation of a quantity f is introduced with $f' = f - \bar{f}$. To facilitate the comparison with the non-averaged equations $(2.28) - (2.30)$, the mean average internal energy has been summarized with the average turbulent kinetic energy $k_t = \frac{1}{2} (\widetilde{u_i'' u_i''})$ to $\tilde{e} = \tilde{T} + \kappa(\kappa - 1) M_\infty^2 k_t$. The shear stress τ_{ik} is obtained from (2.32). For the sake of clearer notation, the average viscous stress tensor $\tilde{\tau}_{ik}$ has been formed with the Favre-averaged velocities $\tilde{u}_i$ and the mean dynamic viscosity $\bar{\mu}$, and, with the corresponding fluctuation τ_{ik}'', may be written:

$$\tilde{\tau}_{ik} = \bar{\mu} \left(\frac{\partial \tilde{u}_i}{\partial x_k} + \frac{\partial \tilde{u}_k}{\partial x_i} - \frac{2}{3} \frac{\partial \tilde{u}_j}{\partial x_j} \delta_{ik} \right),$$

$$\tau_{ik}'' = \mu \left(\frac{\partial u_i''}{\partial x_k} + \frac{\partial u_k''}{\partial x_i} - \frac{2}{3} \frac{\partial u_j''}{\partial x_j} \delta_{ik} \right).$$

The mean heat flux from heat conduction $\bar{q}_k$ and its fluctuation q_k'' are given by

$$\tilde{q}_k - \bar{\lambda} \frac{\partial \tilde{T}}{\partial x_k}, \quad q_k'' - \lambda \frac{\partial T''}{\partial x_k}.$$

The averaged equations $(2.42) - (2.44)$ assume an ideal gas $p = \rho T$, for which after averaging the simple relation

$$\bar{p} = \bar{\rho}\bar{T} \tag{2.45}$$

is obtained. The parts of the averaged fluctuation quantities R_i^u and R^e that are dependent on the Reynolds number can generally be neglected. In any case R_i^u and R^e may be considered as being given via a turbulence model.

For incompressible, turbulent flows of media with constant transport coefficients, the differential equation system $(2.42) - (2.44)$ is simplified:

$$\frac{\partial \bar{u}_k}{\partial x_k} = 0, \tag{2.46}$$

$$\left(\frac{\partial \bar{u}_i}{\partial u} + \bar{u}_k \frac{\partial \bar{u}_i}{\partial x_k} \right) = -\frac{\partial \bar{p}}{\partial x_i} + \frac{1}{Re_L} \frac{\partial^2 \bar{u}_i}{\partial x_k{}^2} + R_i^u, \tag{2.47}$$

$$R_i^u = -\frac{\partial \overline{u_i' u_k'}}{\partial x_k}.$$

The pressure has not been referred to its value in the free stream, but rather to the doubly dynamic pressure of the free stream $\rho_\infty U_\infty^2$. The energy equation is not required to close the system of equations. With the perturbation ansatz, for example for the Favre-averaged velocities $\tilde{u}_i^0$ at the location of the perturbation analysis

$$\tilde{u}_i(x, y, z, t) = \tilde{u}_i^0(z) + \tilde{u}_i'(x, y, z, t), \tag{2.48}$$

the following linear perturbation differential equations are found

$$\tilde{L}[(\tilde{u}_i', \tilde{T}', \bar{\rho}')(x, y, z, t)] = G(x, y, z, t), \tag{2.49}$$

where again the nonlinear terms of the perturbation quantities have been neglected. In addition it is assumed that the perturbation quantities of the Reynolds shear stresses may be neglected, so that the entire information about the turbulent flow is contained in the basic profile $\tilde{u}_i^0$, $\tilde{T}^0$, $\tilde{\rho}^0$. With these assumptions the linear operator $\tilde{L}$ is obtained from (2.49), by formally replacing the laminar basic flow u^0, T^0, ρ^0 in L by the averaged turbulent flow $\tilde{u}_i^0$, $\tilde{T}^0$, $\bar{\rho}^0$. The rest of the procedure corresponds to that for laminar basic flow.

3 Flow Simulation

At the time of the Prandtl memorial lecture *H. Oertel* 1994, the calculation of the basic flow U_i^0 as the basis for the perturbation ansatz of laminar flow (2.2), (2.34) and of turbulent flow $\tilde{U}_i^0$ (2.48) was carried out by fluid mechanical software developed at universities. To calculate the laminar, incompressible basic flow, a special finite-difference Galerkin method was developed *K. Hannemann, H. Oertel* 1989, and for the compressible basic flow the finite-volume software packet KAPPA (**Ka**rlsruhe **P**arallel **P**rogram for **A**erodynamics) *H. Oertel* 1996.

The solution of the eigenvalue problem of the stability analysis of local perturbations was carried out using a collocation-spectral method. To validate the stability analysis in the case of the boundary-layer flow and wake flow, the time and spatial development of the local perturbation was numerically simulated by direct solution of the Navier-Stokes equations (DNS). To do this, special Galerkin and spectral methods were developed *K. Hannemann, H. Oertel* 1989 and *M.T. Stoynov, H. Oertel* 2002. The mathematical details of the progressive development of the numerical algorithms can be found in seven editions of the textbook Fluid Mechanics *H. Oertel, M. Böhle* 1995–2010 and three editions of Numerical Fluid Mechanics *H. Oertel, E. Laurien* 1995–2009. In the following sections the numerical methods of calculating the basic flow and the ansatz to the eigenvalue problem of stability analysis will be described.

By now the university software packet has been replaced by commercial fluid mechanics software, which however has the disadvantage that the details of the numerical alogorithm used and the models of the source code are not available. Their application in research and practice requires solid verification of the numerical algorithms and validation of the numerical models, which are also described extensively in the above textbooks. A new approach for further development of the university software is the *OpenFOAM software packet*, which provides a CFD toolbox of source code of numerical algorithms, which can be adapted to the flow problem to be solved.

3.1 Basic Flow

To calculate the laminar basic flow, the finite-difference Galerkin method was developed. A feature of this is that it leads to a stable approximation solution with little numerical dissipation and permits elimination of the pressure of the incompressible flow via the Galerkin algorithm. The finite-difference Galerkin method enables the discrete pressure to be removed by projecting

the discretized Navier-Stokes equations into a divergence-free subspace using a Galerkin technique. Consider the following discretized form of the Navier-Stokes equations and the boundary conditions at time step t_n:

$$\frac{\partial u_k^h}{\partial x_k^h} = 0 \qquad \text{on} \quad \omega_h, \tag{3.1}$$

$$\frac{\partial u_i^h}{\partial t} + \left(u_k^h \frac{\partial}{\partial x_k^h}\right) u_i^h = -\frac{\partial p^h}{\partial x_i^h} + \frac{1}{Re_L}\frac{\partial^2 u_i^h}{\partial x_k^{h^2}} \qquad \text{on} \quad \Omega_h, \tag{3.2}$$

$$u_i^h = \beta_i^h \qquad \text{on} \quad \Omega_{R_h}, \tag{3.3}$$

with the index h indicating discrete quantities, spaces and operators. The boundary data are given by β_i^h.

The equations are discretized on a staggered grid. Ω_h and ω_h represent the inner mesh points for vectors and scalar quantities respectively, and Ω_{R_h} contains the mesh points on the boundary (see Figure 3.1). The discrete gradient and divergence operators must be adjoint in order to eliminate the pressure from the system of equations. In this application this was achieved by using central differencing on the staggered grid. The following discrete approximation can be made for the velocity vector:

$$u_i^h = r_i^h + \sum_{i=1}^{m} a_i(t)\Phi_i^h, \tag{3.4}$$

where Φ_i^h are discrete divergence-free base functions defined on Ω_h only. For a uniform grid containing n^2 inner grid points, the base functions are defined as follows:

$$
\begin{aligned}
\Phi_{i,j}^{l+\frac{1}{2},m+\frac{1}{2}} \quad &= (1,-1)^t, & i &= l, j = m, \\
&= (1,1)^t, & i &= l+1, j = m, \\
&= (-1,1)^t, & i &= l+1, j = m+1, \\
&= (-1,-1)^t, & i &= l, j = m+1, \\
&= (0,0)^t, & &\text{all other } i,j, \\
l &= 1,\ldots,n-1; & m &= 1,\ldots,n-1.
\end{aligned}
\tag{3.5}
$$

On the boundary Ω_{R_h}, these internal base functions are zero. The boundary vector r_i^h must fulfil the boundary conditions (3.5) and can be expressed with a sum similar to that in (3.4). The structure of the base functions remains unchanged, except that they must be defined on the boundary. The boundary vector can easily be computed for Dirichlet boundary conditions. However, if

the boundaries are time dependent, r_i^h must be recalculated after each time step. The system of equations for determining the unknown coefficients a_i can be derived with a discrete Galerkin technique, i.e. the scalar product of (3.3) with every base function must be zero:

$$\left(\frac{\partial u_i^h}{\partial t} + \left(u_k^h \frac{\partial}{\partial x_k^h}\right) u_i^h + \frac{\partial p^h}{\partial x_i^h} - \frac{1}{Re_L} \frac{\partial^2 u_i^h}{\partial x_k^{h^2}}, \Phi_i^h\right)_{\Omega_h} = 0, \;\; i = 1, \ldots, m. \;\; (3.6)$$

Using a discrete analogue of integration by parts, the component of the scalar product containing the pressure can be written as

$$\left(\frac{\partial p^h}{\partial x_i^h}, \Phi_i^h\right)_{\Omega_h} = \left(p^h, \Phi_i^h\right)_{\Omega_{R_h}} - \left(p^h, \frac{\partial \Phi_i^h}{\partial x_i^h}\right)_{\omega_h} = 0, \;\; i = 1, \ldots, m. \;\;\;\; (3.7)$$

The base functions are divergence free and vanish on Ω_{R_h}. Therefore the pressure is eliminated from the system of equations and only the following equation is solved:

$$\left(\frac{\partial u_i^h}{\partial t} + \left(u_k^h \frac{\partial}{\partial x_k^h}\right) u_i^h - \frac{1}{Re_L} \frac{\partial^2 u_i^h}{\partial x_k^{h^2}}, \Phi_i^h\right)_{\Omega_h} = 0, \;\; i = 1, \ldots, m. \;\;\;\; (3.8)$$

The integration in time is performed with explicit Runge–Kutta time stepping. Therefore all quantities at the time step t_n are known and the system

$$M a_t = f \tag{3.9}$$

must be solved for the time derivative a_t of the coefficient a. The right-hand side f contains the contribution of the convective and the diffusion term. It can be shown that the matrix M is symmetric and positive definite. The solution of a_t is found iteratively by a conjugate gradient method.
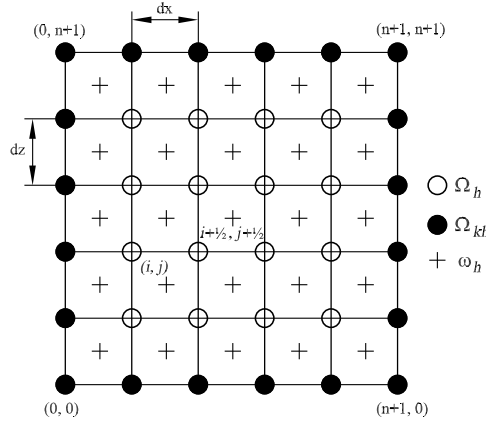

Fig. 3.1. Definition of the discrete spaces

33

The description of the finite-difference Galerkin method is restricted to the case of a uniform mesh only. Arbitrary geometries with non-uniform mesh can be handled by transforming them onto a computation space with uniform mesh, where the algorithm just described can then be applied.

To start the numerical simulation of the basic flow, a converged solution of the steady Navier-Stokes equation, obtained at a supercritical Reynolds number of $Re_D = 200$ is used. Figure 3.2 shows the disturbance evolution detected in the wake behind a flat plate up to a dimensionless time $t = 500$. The top frame shows the maximum, within the entire flow field, of the unsteady term $|\partial u/\partial t|$ at each time step. Since the entire flow field was searched to determine $|\partial u/\partial t|_{\max}$, inferences could not be made about the behavior at a fixed point. An overall impression, however, was attained about the proximity of the entire flow to steady-state conditions. In interpreting the top frame of Figure 3.2, it can be concluded that after the symmetry restriction is relaxed at $t = 0$, two competing processes take place. First, the flow proceeds towards the steady solution for a dimensionless time of about 200. Since the maximum unsteadiness in the entire flow field is less than 10^{-6} for $0 < t < 200$, it might be concluded that the flow is indeed quasi-steady at this supercritical Reynolds number. Consequenctly, the overall flow unsteadiness, indicated by
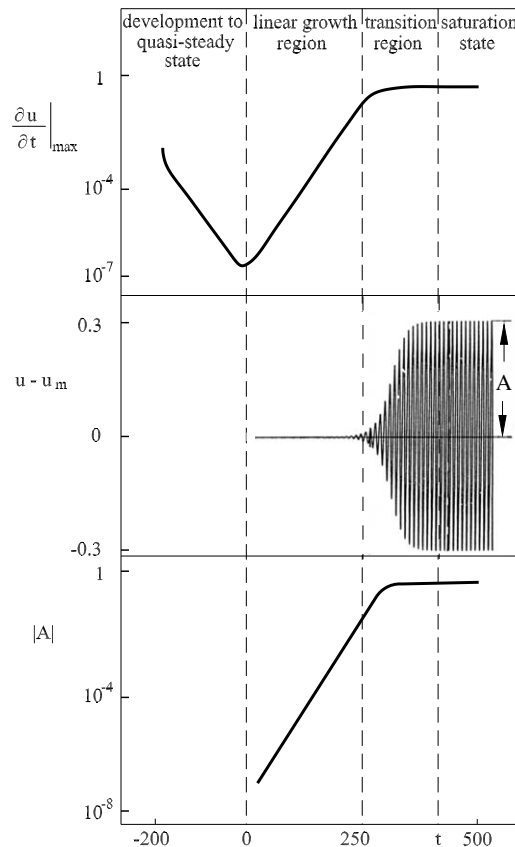
Fig. 3.2. Temporal development of the flat-plate wake, $Re_D = 200$

34
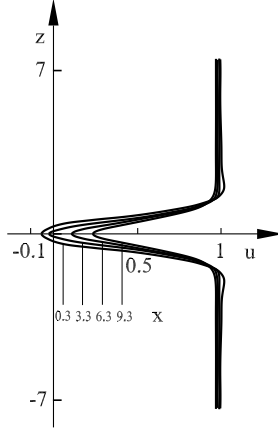
Fig. 3.3. U^0 velocity profiles of the quasi-steady wake flow, $Re_D = 200$

$|\partial u/\partial t|_{max}$, reaches a turning point that has been referred to as the quasi-steady state at $t = 0$ in Figure 3.2. This is the *basic state* for the stability analysis, for which the velocity profiles in the wake of a flat plate are shown in Figure 3.3. After the quasi-steady state is reached, the antisymmetrical disturbance continues to grow exponentially, which indicates linear stability behavior, until the nonlinear saturation or vortex-shedding state is finally reached. The velocity components, minus the mean velocity u_m, in connection with the amplitude growth A show a well-defined exponential growth rate of the vortex-shedding fluctuations occurring simultaneously with the increase of the maximum $|\partial u/\partial t|$. In the nonlinear transitional region, the transition to the saturated state occurs.

Figure 3.4 shows the development of the wake flow in terms of instantaneous streamline plots. At time t_0, the streamline pattern of the quasi-steady solution shows a symmetric backflow region extending $3.6D$ downstream of the trailing edge. The first effect, seen in the streamline plots occurring for $t > t_0$, is a change in the topological structure of the streamline patterns at the saddle point located at the end of the backflow region. Here the symmetry is removed and the backflow region breaks open. The time sequence in Figure 3.4 also shows the flow at the end of the linear growth region at $t = 240$ and the Kármám vortex street at $t = 466$.

The calculation of the turbulent basic flow $\tilde{U}_i^0$ as the basis for the stability analysis of local perturbations is carried out using the commercial software Star CD$^{©}$ (Computational Dynamics Ltd. London) and FLUENT$^{®}$ (ANSYS$^{®}$ Inc.). The Reynolds-averaged basic equations (2.46) – (2.47) for the compressible flow and (2.42) – (2.44) for incompressible flow are solved numerically using the *finite-volume method*. The finite-volume algorithms are based on the fundamental equations in conservative form, for which the derivation is described in detail in our textbook *H. Oertel, M. Böhle* 2009.

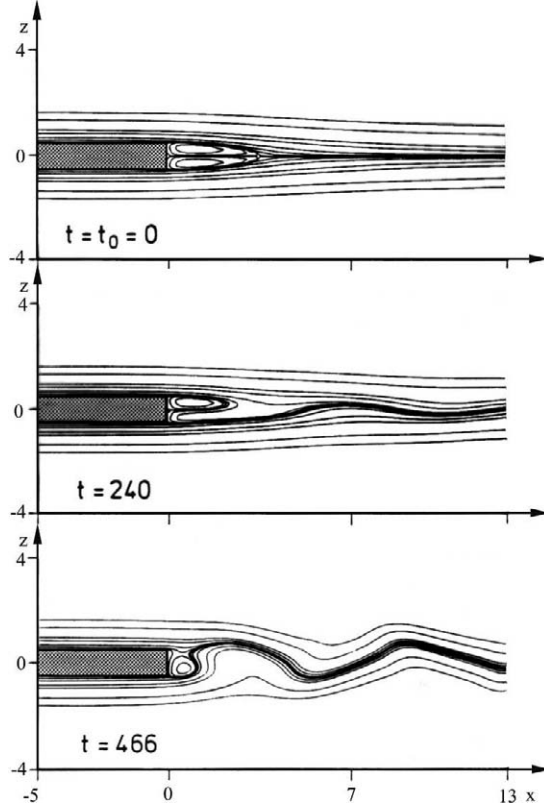The conservative form of the fundamental equations is obtained by starting

Fig. 3.4. Temporal development of the wake

from a control volume fixed in space that does not move with the flow. With the solution vector $\bar{U}_i$, the time averaged convective fluxes $\bar{F}_i$, the dissipative fluxes $\bar{G}_i$ and the vector of an algebraic turbulence model $\bar{R}_{i,m}$, which is combined with $\bar{G}_{i,m}$ to form $\bar{G}_{i,m}^{\text{alg}}$ for the calculation of, for example, the flow past a transonic wing, as follows:

$$\frac{\partial \bar{U}_i}{\partial t} + \sum_{m=1}^{3} \frac{\partial \bar{F}_{i,m}}{\partial x_m} - \frac{1}{Re_L} \cdot \sum_{m=1}^{3} \frac{\partial \bar{G}_{i,m}^{\text{alg}}}{\partial x_m} = 0. \tag{3.10}$$

For the modeling of anisotropic turbulence, for example the wake flow of a car, it is not possible to add the dissipative fluxes algebraically and additional nonlinear transport equations have to be formulated for the turbulent kinetic energy K, the turbulent dissipation ε or the vorticity ω.

As the finite-volume method starts with the discretization of the spatial region of integration V, equation (3.10) first needs to be brought to the corresponding integral form of the fundamental equations. Integrating over the entire volume V of the flow field, the following expression is obtained:

$$\int\limits_V \frac{\partial \bar{U}_i}{\partial t} \cdot \mathrm{d}V + \int\limits_V \left(\sum_{m=1}^{3} \frac{\partial \bar{F}_{i,m}}{\partial x_m} - \frac{1}{Re_L} \cdot \sum_{m=1}^{3} \frac{\partial \bar{G}_{i,m}^{\mathrm{alg}}}{\partial x_m} \right) \cdot \mathrm{d}V = 0. \qquad (3.11)$$

The divergence theorem (Gauss' theorem) is required for further maniputlation of equation (3.11). For a general vector function f_i this reads:

$$\int\limits_V \mathrm{div}\, f_i \cdot \mathrm{d}V = \int\limits_V \cdot \nabla f_i \cdot \mathrm{d}V = \int\limits_O f_i\, n_i \cdot \mathrm{d}O. \qquad (3.12)$$

This theorem states that the volume integral of the divergence of a vector function f_i is equal to the surface integral of the scalar product of the vector function f_i with the external surface normal vector n_i of the surface O, therefore the fluxes passing through the surface of the volume. O is the surface of the volume of calculation and $n_i = (n_1, n_2, n_3)$ is the outward pointing normal vector

$$\int\limits_V \frac{\partial \bar{U}_i}{\partial t} \cdot \mathrm{d}V + \int\limits_O \left(\sum_{m=1}^{3} \bar{F}_{i,m} - \frac{1}{Re_L} \cdot \sum_{m=1}^{3} \bar{G}_{i,m}^{\mathrm{alg}} \right) \cdot n_i \cdot \mathrm{d}O = 0. \qquad (3.13)$$

As the fundamental equations in conservative form were set up for a control volume fixed in space, the region of integration V is not dependent on time. This means that the time derivative in equation (3.13) can be pulled in front of the integral. It follows then that

$$\frac{\partial}{\partial t} \int\limits_V \bar{U}_i \cdot \mathrm{d}V + \int\limits_O \left(\sum_{m=1}^{3} \bar{F}_{i,m} - \frac{1}{Re_L} \cdot \sum_{m=1}^{3} \bar{G}_{i,m}^{\mathrm{alg}} \right) \cdot n_i \cdot \mathrm{d}O = 0. \qquad (3.14)$$

The first step of the discretization of the continuous region of integration V consists of dividing V into individual discrete volume cells V_{ijk} each with six surfaces $O_l \cdot n_i$, where $l = 1, \ldots, 6$ is the index for the surface. O_l denotes the magnitude of the surface of the l-th surface and $n_i^l = (n_{lx}, n_{ly}, n_{lz})$ the corresponding external normal unit vector.

Figure 3.5 shows a discrete volume element V_{ijk} with the six normal unit vectors.

The values of the flow quantities $U_{i,\mathrm{ijk}}$ in the center of each volume cell V_{ijk} are required. The next step therefore consists of approximating the fundamental equations (3.14) for each individual volume cell V_{ijk}. The following is obtained:

$$\frac{\mathrm{d}}{\mathrm{d}t} U_{i,\mathrm{ijk}} \cdot V_{\mathrm{ijk}} + \sum_{m=1}^{3} \sum_{l=1}^{6} \left(\bar{F}_{i,ml} \cdot O_{ml} \right)_{\mathrm{ijk}} - \frac{1}{Re_\infty} \sum_{m=1}^{3} \sum_{l=1}^{6} \left(\bar{G}_{i,ml}^{\mathrm{alg}} \cdot O_{ml} \right)_{\mathrm{ijk}} = 0. (3.15)$$

The fluxes F_{il} and G_{il}^{alg} are now approximated at the center of every side surface. In order to calculate them, the conservative variables are averaged between the two cells touching at one surface, e.g. for any variable Φ:

$$(\Phi_{l=1})_{\mathrm{i,j,k}} = \frac{1}{2} \cdot (\Phi_{\mathrm{i,j,k}} + \Phi_{\mathrm{i-1,j,k}}) \ , \ (\Phi_{l=2})_{\mathrm{i,j,k}} = \frac{1}{2} \cdot (\Phi_{\mathrm{i+1,j,k}} + \Phi_{\mathrm{i,j,k}}) ,$$

$$(\Phi_{l=3})_{\mathrm{i,j,k}} = \frac{1}{2} \cdot (\Phi_{\mathrm{i,j,k}} + \Phi_{\mathrm{i,j-1,k}}) \ , \ (\Phi_{l=4})_{\mathrm{i,j,k}} = \frac{1}{2} \cdot (\Phi_{\mathrm{i,j+1,k}} + \Phi_{\mathrm{i,j,k}}) , \quad (3.16)$$

$$(\Phi_{l=5})_{\mathrm{i,j,k}} = \frac{1}{2} \cdot (\Phi_{\mathrm{i,j,k}} + \Phi_{\mathrm{i,j,k-1}}) \ , \ (\Phi_{l=6})_{\mathrm{i,j,k}} = \frac{1}{2} \cdot (\Phi_{\mathrm{i,j,k+1}} + \Phi_{\mathrm{i,j,k}}) .$$

For variables that appear as derivatives, for example in the calculation of shear stresses and the heat flux in $G_{i,ml}^{\mathrm{alg}}$, a *local transformation* must be carried out for each side surface l. The direction of the grid lines with constant indices i,j,k are denoted with ξ, η and ζ.

The total differential of a variable Φ then leads to

$$\begin{pmatrix} \frac{\partial \Phi}{\partial \xi} \\ \frac{\partial \Phi}{\partial \eta} \\ \frac{\partial \Phi}{\partial \zeta} \end{pmatrix}_l = \begin{pmatrix} \frac{\partial x}{\partial \xi} & \frac{\partial y}{\partial \xi} & \frac{\partial z}{\partial \xi} \\ \frac{\partial x}{\partial \eta} & \frac{\partial y}{\partial \eta} & \frac{\partial z}{\partial \eta} \\ \frac{\partial x}{\partial \zeta} & \frac{\partial y}{\partial \zeta} & \frac{\partial z}{\partial \zeta} \end{pmatrix}_l \cdot \begin{pmatrix} \frac{\partial \Phi}{\partial x} \\ \frac{\partial \Phi}{\partial y} \\ \frac{\partial \Phi}{\partial z} \end{pmatrix}_l , \quad (3.17)$$

where the matrix is denoted T_l (*transformation matrix*). Inverting this equation yields
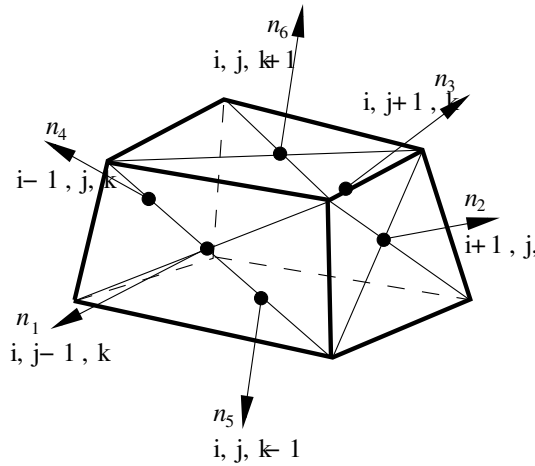
Fig. 3.5. Volume cell and normal unit vectors

$$
\begin{pmatrix}
\frac{\partial \Phi}{\partial x} \\[4pt]
\frac{\partial \Phi}{\partial y} \\[4pt]
\frac{\partial \Phi}{\partial z}
\end{pmatrix}_l
= T_l^{-1} \cdot
\begin{pmatrix}
\frac{\partial \Phi}{\partial \xi} \\[4pt]
\frac{\partial \Phi}{\partial \eta} \\[4pt]
\frac{\partial \Phi}{\partial \zeta}
\end{pmatrix}_l .
\tag{3.18}
$$

The differential quotients appearing here are expressed by means of differences in the solution variables or the mid-points of the cells along the local directions ξ, η and ζ, e.g. for the surface $l = 1$:

$$
\left(\left. \frac{\partial \Phi}{\partial \xi} \right|_{l=1} \right)_{ijk} = \Phi_{i,j,k} - \Phi_{i-1,j,k},
$$

$$
\left(\left. \frac{\partial \Phi}{\partial \eta} \right|_{l=1} \right)_{ijk} = \frac{1}{2} \cdot \left[\frac{1}{2} \cdot (\Phi_{i,j+1,k} + \Phi_{i-1,j+1,k}) - \frac{1}{2} \cdot (\Phi_{i,j-1,k} + \Phi_{i-1,j-1,k}) \right], \tag{3.19}
$$

$$
\left(\left. \frac{\partial \Phi}{\partial \zeta} \right|_{l=1} \right)_{ijk} = \frac{1}{2} \cdot \left[\frac{1}{2} \cdot (\Phi_{i,j,k+1} + \Phi_{i-1,j,k+1}) - \frac{1}{2} \cdot (\Phi_{i,j,k-1} + \Phi_{i-1,j,k-1}) \right].
$$

Here Φ may be either a solution variable or a coordinate (x, y, z). The final result of the spatial discretization is a system of coupled ordinary differential equations for each cell i,j,k:

$$
\frac{\mathrm{d}}{\mathrm{d}t} U_{i,i,j,k} + Q(U_{i,i,j,k}, U_{i,i\pm 1,j\pm 1,k\pm 1}) = 0,
\tag{3.20}
$$

with the spatial discretization operator $Q(U_i)$ which contains the coupling. The equation (3.20) is nothing other than equation (3.15) divided by the volume of the cell V_{ijk}.

This system needs to be integrated in time. For this, the classic explicit fourth order *Runge-Kutta method*, for example, may be chosen. In calculating incompressible flows the difficulty that always arises is that the pressure field is not known. Rather only the pressure gradients appear in the source terms of the Navier-Stokes equations. In order to calculate consistent pressure and velocity fields, there are at present two basically different approaches.

In the first method, the continuity equation is used to determine an artificially introduced density. Using an equation of state (e.g. the equation of state for ideal gases), the pressure can then be determined. This approach permits all derived algorithms for compressible flows to be carried over to incompressible flows. The mathematical details are set out in Chapter 5 of Strömungsmechanik, *H. Oertel jr., M. Böhle* 1999. In this *method of artificial compressibility*, an arbitrarily weak coupling is set between the pressure and the density.

Another method to determine the velocity and pressure fields of incompressible flows is a method related to the pressure. In replication of the momentum equation and the continuity equation, the pressure is determined from a separate equation that results from the Navier-Stokes and continuity equations. Various solution algorithms have been developed for this pressure-referred method. In what follows, the so-called *pressure-correction method* and the resulting *SIMPLE algorithm* will be described.

First a preliminary pressure field p^* is estimated. Using this estimated pressure field, the Navier-Stokes equations can be discretized and solved. In order to solve the Navier-Stokes equations, the finite-volume method is also used. An algebraic system of equations for the unknown velocity components u_i^*, v_i^* and w_i^* in the nodes of the finite-volume computational grid is obtained:

$$
\begin{aligned}
a_i^u \cdot u_i^* &= \sum_{nb}^{3} a_{nb}^u \cdot u_{nb} + b^u + (p_{i+1}^* - p_{i-1}^*) \cdot A_i, \\
a_i^v \cdot v_i^* &= \sum_{nb}^{3} a_{nb}^v \cdot v_{nb} + b^v + (p_{j+1}^* - p_{j-1}^*) \cdot A_j, \\
a_i^w \cdot w_i^* &= \sum_{nb}^{3} a_{nb}^w \cdot w_{nb} + b^w + (p_{k+1}^* - p_{k-1}^*) \cdot A_k.
\end{aligned}
\tag{3.21}
$$

In these equations, the coefficients a_i^u, a_i^v, a_i^w or $a_{nb}^u, a_{nb}^v, a_{nb}^w$, which result from discretizing the convective and dissipative terms at the node currently under consideration i or at neighboring nodes, respectively, are sorted and summarized. The coefficients b^u, b^v, b^w contain all source terms. The pressure gradient is represented by the pressure differences in the x, y and z directions multiplied by the corresponding side surfaces A_i, A_j and A_k. The summation $\sum_{nb}$ is carried out over all neighboring nodes of the node under consideration i. The resulting velocity field u_i will generally not satisfy the continuity equation. The aim of the next steps is therefore to improve the pressure estimate p^* so that the velocity field u_i does satisfy the continuity equation. To do this, the pressure and velocity corrections p' and v', v' and w' (not to be confused with perturbation or fluctuation quantities) are introduced. If pressure field is assumed to be correct

$$
p = p^* + p',
\tag{3.22}
$$

then it needs to be investigated how the velocity components u, v and w

$$
u = u^* + u', \quad v = v^* + v', \quad w = w^* + w'
\tag{3.23}
$$

change with the pressure correction p'. If the discretized Navier-Stokes equation for the preliminary velocity field (3.21) is subtracted from the discretized

Navier-Stokes equation for the exact velocity u, terms are found of the form $u = u^* - \mathrm{d}^u(p'_{i+1} - p'_{i-1})$, which are called velocity correction equations. It then remains to derive an equation for the pressure correction p' from the continuity equation. The velocities that occur are also replaced by the velocity correction equation and the terms that arise are finally solved for the unknown pressure corrections p'. In this manner all the equations that are necessary to calculate an incompressible flow are established.

This algorithm is contained in various forms in almost all commercial software packets and since it was developed it has undergone numerous improvements with respect to its convergence rate. It provides the numerical basis for the calculation of the turbulent basic flow $\tilde{U}_i^0$ for the stability analysis of local perturbations that is implemented in the university program KAPPA and currently available commercial software.

The boundary-layer flow of a *transonic wing* calculated in this manner is shown in Figure 3.6. First the geometry of the wing in the flow discretized with a finite-volume grid is shown. The fine resolution in the region of the stagnation line and in the wake of the wing, as well as in the region of the shock wave, is clearly visisble. The result of the finite-volume calculation for the Mach number $M_\infty = 0.78$, the Reynolds number $Re_L = 26.6 \cdot 10^6$ and the sweep angle $\phi = 20°$ is shown in the form of isotachs, i.e. lines of constant Mach

finite–volume grid

pressure

iso Mach lines

$M_\infty = 0.78$, $Re_L \cdot 10^6 = 26.6$, angle of incidence $= 2.2°$
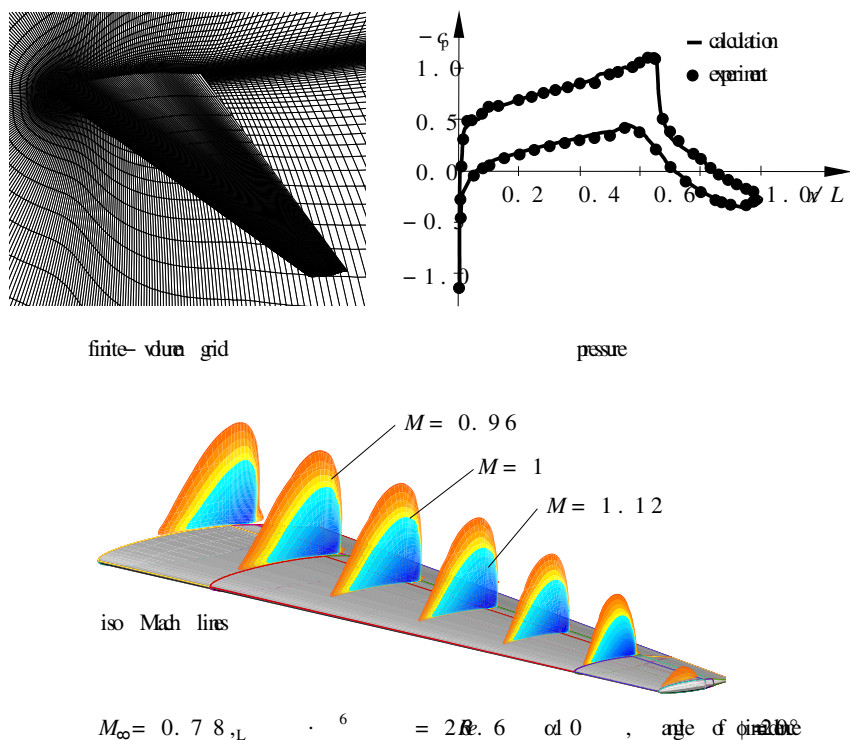
Fig. 3.6. Finite-volume discretization, pressure and Mach number distribution of a transonic wing

number. The numerical solutions shows the supersonic field and the shock
wave that terminates this downstream. For the given lift coefficient $c_a = 0.0506$
of a model wing of the Airbus A 320, a drag coefficient of $c_w = 0.0184$ is
calculated. This is the value that can be reached if a transonic laminar wing
can be realized, as will be treated further in Section 4.1.2.

Whereas the flow past a wing is solved with the Favre-averaged compressible
fundamental equations, for the flow past a car the Reynolds-averaged equa-
tions are solved. As a turbulence model for the anisotropic turbulent wake
flow, a nonlinear K-ε turbulence model is applied. In the c_p diagrams in Fig-
ure 3.7, the dimensionless pressure distributions on the upper and lower sides
of the car are shown for the Reynolds number $Re_L = 8 \cdot 10^6$ ($U_\infty = 130 km/hr$)
in comparison with experimental results in a wind tunnel. In comparison to
the flow past a wing, in calculations of the flow past a car, the road must also
be taken into account. The calculation is then carried out following a trans-
formation of reference frame from a moving car in air at rest to a car at rest
in a wind flow. Therefore the road also needs to be discretized in order to take
account in the calculation of boundary-layer effects between the underside of
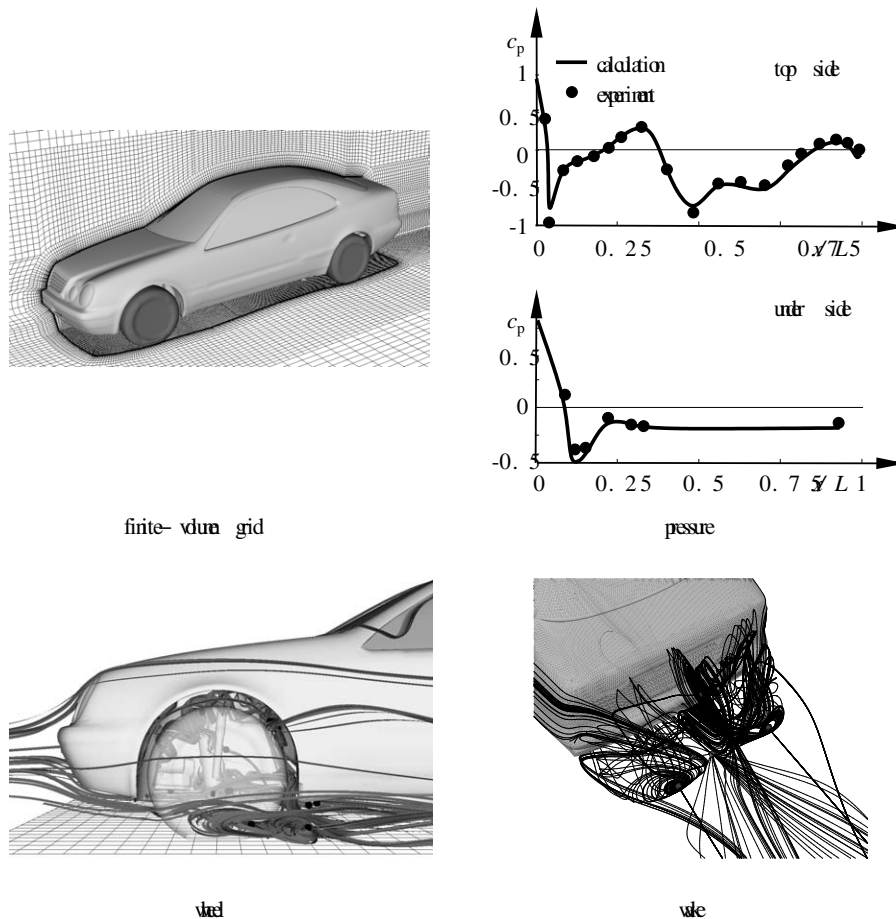
Fig. 3.7. Finite-volume discretization of the flow past a car and the pressure distri-
bution in the symmetry plane, $U_\infty = 130 km/hr$, $Re_L = 8 \cdot 10^6$

42

the car and the road. The boundary condition for the road is then prescribed as the velocity of the free stream of air, while on the underside of the car it is required that $u_i = 0$. The condition of the moving road is challenging to achieve in a wind tunnel using a moving band, which is why frequently a simplified experiment is resorted to in a wind tunnel with a road at rest and a car at rest in free stream of air. Therefore the calculations of the basic flow for the stability analysis, as in Section 4.2.3, were carried out with a road at rest and a car at rest. Figure 3.7 it can be seen that the measured and calculated pressure distributions agree very well with each other. The numerical solution also shows that the structure of the wake flow was correctly represented. Downstream from the trunk a horseshoe vortex forms which is energized on the one hand by the shear layer at the spoiler lip on the trunk and on the other hand by the diffusor flow between the underside of the car and the road.

3.2 Local Perturbations

As confirmation of the existence of absolutely unstable regions in the wave flow, simulation calculations of local wave packets are carried out using the finite-difference Galerkin method described in Section 3.1. The laminar basic flow in the wake of a flat plate, shown in Figure 3.4, was superimposed with sine-wave perturbations at various positions in the wake flow. Figure 3.8 shows a selection of sinusoidal impulse responses. The sine units and velocity components return the impulse response at the marked points after onset of the impulse, which is analogous to the asymptotic behavior at large time
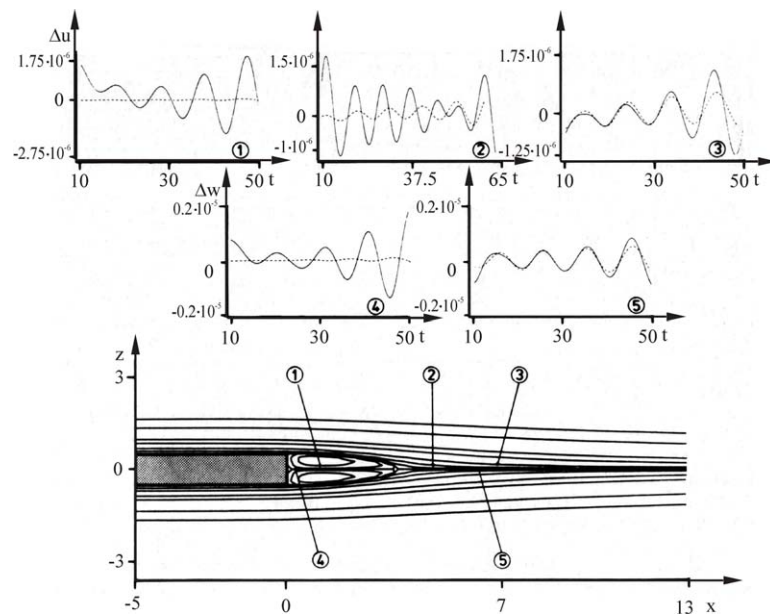
Fig. 3.8. Numerical simulation of the impulse response for the quasi-steady basic state $Re_L = 200$
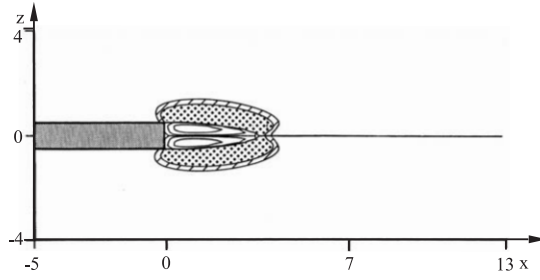
Fig. 3.9. Absolutely unstable region $Re_L = 200$

steps. The solid lines represent the velocity signals after the onset of the disturbance; the dashed lines represent the original disturbances. It is noticeable that the disturbaces initiated by the impulse are, after sufficient time has passed, larger at each point than the natural impulses present. This situation can be attributed to the absolute instability of the flow region. Evaluation of the impulse responses reveals that they are of two differing types. At points 1 and 4 the induced disturbances immediately increase, and their amplitudes lie, at all points in time, significantly above those of the natural disturbances. Conversely, the induced disturbances at points 2, 3 and 5 are damped at first and after a certain amount of time are of the same magnitude as the natural disturbances, only to increase again. Moreover, it can be shown that the early damping, which is evident from signal 2, becomes larger upstream. Figure 3.9 gives the complete results. The area of quasi-steady backflow and the corresponding area of absolute instability are illustrated. From the random tests taken, it can be concluded that the region in which the disturbances are immediately amplified enlarges when larger amplitudes are introduced. In comparison, Figure 3.10 shows the development of amplitude disturbances at a subcritical Reynolds number. All of the induced disturbances are temporally and spatially damped. The existence of and knowledge about absolutely unstable regions offers the possibility of effective wake control, as mentioned in the introductory Chapter 1. Figure 3.11 shows the effect of a base bleed and
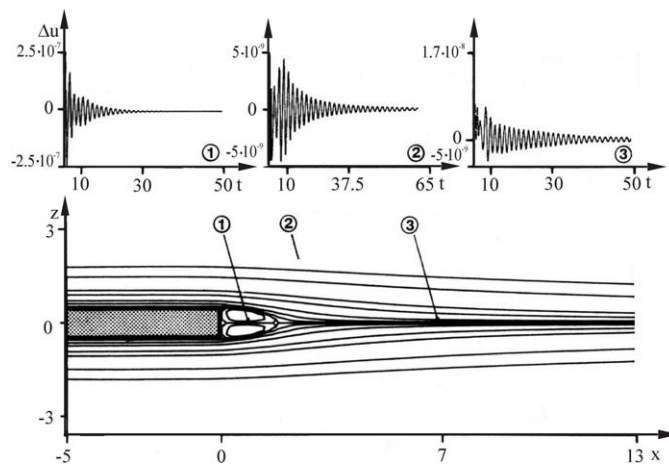
Fig. 3.10. Impulse response at a subcritical Reynolds number $Re_L = 80$

44

of a perturbation cylinder on the periodic vortex shedding at blunt bodies. With flow control, the Kármán vortex street in the wake is supressed.

At the time of the Prandtl memorial lecture *H. Oertel* 1994, the Orr-Sommerfeld stability analysis of Section 2.1 had been carried out numerically using the assumption of parallel flow with the *Chebyshev collocation method.* The unknown amplitude function $\hat{\psi}(z)$ should be obtained in the range $[-\infty, \infty]$. Chebyshev polynomials $T_K(\eta)$ of order K have been used to approximate $\hat{\psi}(z)$ in the transformed coordinate $\eta = \eta(z)$:

$$\hat{\psi}(\eta) = \sum_{K=0}^{N-1} b_K T_K(\eta). \tag{3.24}$$

The range is mapped into $[-1, 1]$ via an exponential transformation. The approximation of $\hat{\psi}(z)$ and its derivatives is not performed using an expansion with respect to the Chebyshev coefficient b_K. Instead the Chebyshev collocation method is applied to obtain directly the values of $\hat{\psi}(z)$ at the collocation points:

$$\eta_j = \cos \frac{\pi j}{N-1}; \quad j = 0, \ldots, N-1. \tag{3.25}$$

To distinguish between absolute and convective instability, the eigenvalue spectrum of the Orr-Sommerfeld equation for complex wave number a and complex frequency ω is necessary.
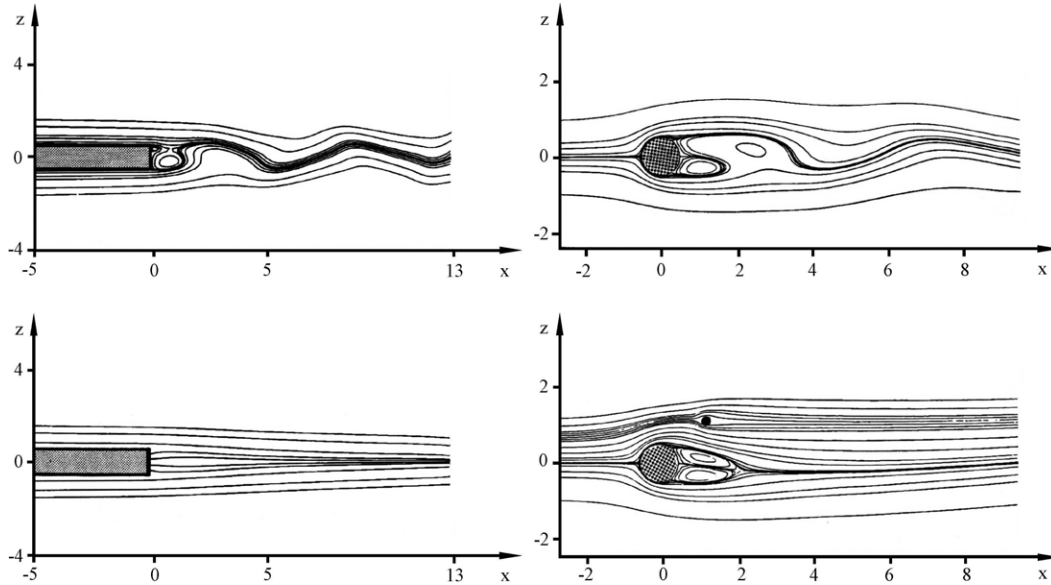
Fig. 3.11. Supression of vortex shedding by means of base bleed, $Re_L = 200$ (left) and perturbation cylinder, $Re_L = 55$ (right)

Figure 3.12, showing the corresponding quasi-steady local wake-flow profile from the numerical solution, reveals that the well-known resonance in Figure 2.12 disappears with base bleeds larger than a critical value. This indicates that the most efficient wake control can be achieved by avoiding absolutely unstable regions in the wake.

Nowadays the commercial software COMSOL Multiphysics is available to solve the stability analysis of local perturbations. COMSOL is based on the programming environment MATLAB and is an effective tool to solve arbitrary systems of partial differential equations. In addition, COMSOL contains an environment for defining and implementing grids for geometries. For two-dimensional problems, the triangulation is based on triangular shaped cells. Routines exist to solve steady and unsteady linear and nonlinear problems, as well as eigenvalue problems. The *finite-element method* is used to discretize the differential equations.

The formulation of the differential equations is kept very general and therefore there is a large degree of flexibility to investigate a wide spectrum of stability problems.

The general system of partial differential equations reads:
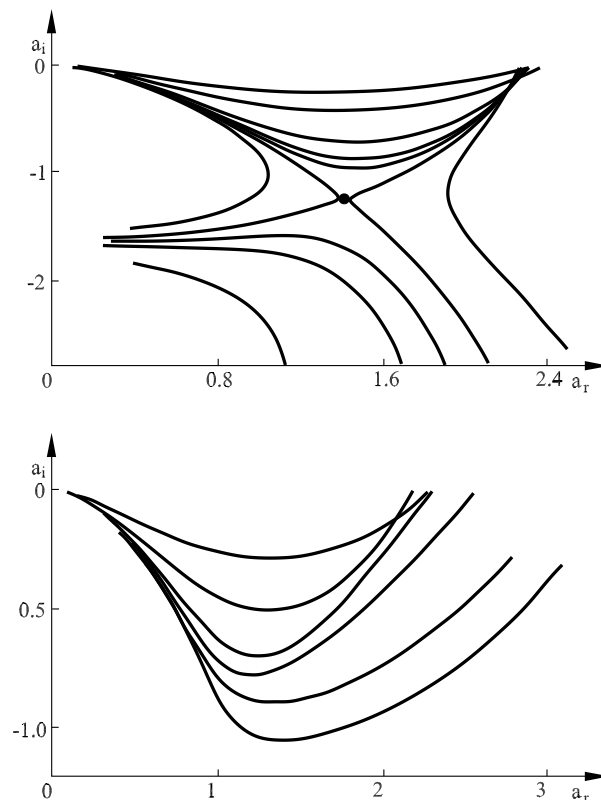
Fig. 3.12. Spatial amplification rate with and without base bleed for a flat plate, $Re_L = 200$

$$e_{iA}\frac{\partial^2 u_i}{\partial t^2} + d_{iA}\frac{\partial u_i}{\partial t} + \frac{\partial}{\partial x_i} \cdot \left(-c_i\frac{\partial u_k}{\partial x_k} - \alpha u_i + \gamma\right) + \beta\frac{\partial u_k}{\partial x_k} + a_i u_i = f_i. \quad (3.26)$$

In COSMOL notation, the conservation equations for mass and momentum read:

$$d_{iA}\frac{\partial u_i}{\partial t} + \frac{\partial}{\partial x_k}\Gamma_k = F_i. \quad (3.27)$$

Here d_i are the mass coefficients, Γ_i the flux matrix

$$d_{iA} = \begin{pmatrix} \rho \\ \rho \\ 0 \end{pmatrix} \quad , \quad \Gamma_i = \begin{pmatrix} -2\mu\frac{\partial u}{\partial x} + p & -\mu\left(\frac{\partial u}{\partial y} + \frac{\partial v}{\partial x}\right) \\ -\mu\left(\frac{\partial v}{\partial x} + \frac{\partial u}{\partial y}\right) & -2\mu\frac{\partial v}{\partial y} + p \\ 0 & 0 \end{pmatrix} \quad (3.28)$$

and F_i are the source terms:

$$F_i = \begin{pmatrix} -\rho\left(u \cdot \frac{\partial u}{\partial x} + v \cdot \frac{\partial u}{\partial y}\right) \\ -\rho\left(u \cdot \frac{\partial u}{\partial x} + v \cdot \frac{\partial v}{\partial y}\right) \\ -\left(\frac{\partial u}{\partial x} + \frac{\partial v}{\partial y}\right) \end{pmatrix}. \quad (3.29)$$

The general fomulation of the Dirichlet boundary conditions R_i and the Neumann boundary conditions G_i at the boundaries of the flow region ∂V reads:

$$R_i = 0 \quad , \quad -n_i \cdot \Gamma_i = G_i + \frac{\partial R_i}{\partial u_i}\mu_L. \quad (3.30)$$

The resulting eigenvalue problem is solved with the finite-element method (see *E. Laurien, H. Oertel* 2009). With the finite-element method, in contrast to the finite-volume method described in the previous section, it is not the differential quotients that are discretized, but rather the solution functions.

The starting point for the finite-element method is the spatial discretization of the geometry into N grid elements. Within these elements, ansatz functions Φ_i are defined. By means of a linear combination of ansatz functions with the coefficient U_i, the approximation solution for the unknown quantity u is obtained:

$$u = \sum_{i=1}^{N} U_i \cdot \Phi_i. \quad (3.31)$$

The *Lagrange elements* used have the following properties:

the ith node of the grid $\Phi_i = 1$,
at all other nodes $\Phi_i = 0$,
within the elements to which the ith node of the grid belongs, Φ_i is a polynomial of a certain prescribed order.

Depending on the order of the polynomial, this results in intermediate nodes within an element.

In the COMSOL software packet, the order of the form functions is given by a lower index in the following notation: $P_m P_n$. The index m stands for the order of the ansatz functions to determine the velocity, while the pressure is approximated by nth order ansatz functions.

The properties of the elements in combination with equation (3.31) mean that the approximation for the solution function u at a node i is given by the value of the coefficient U_i. Between the nodes the solution function has a form defined by the ansatz functions. Instead of the solution function u, therefore, the unknown parameters U_i need to be determined. These are also known as the *degrees of freedom* of the problem.

3.3 Software Verification

Every fluid mechanics software requires, because of the discretization errors of the algorithms and the rounding errors on the computer, verification using qualified experiments or, if possible, with analytical solutions. In our fluid mechanics textbook *H. Oertel, M. Böhle* 2009, numerous verification examples are provided for the various regions of the flow. In this article we summarize the examples that are relevant for flow control in the applications described in Chapter 4.
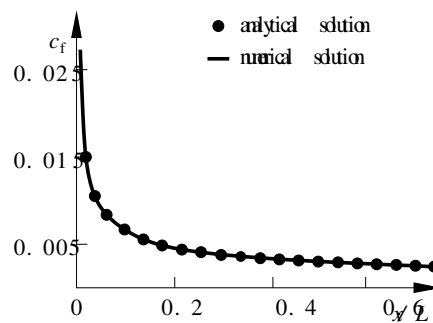
Fig. 3.13. Local friction coefficient c_f of the laminar plate boundary layer, $Re_L = 1 \cdot 10^5$

The classical example for *boundary-layer flows* is the laminar and turbulent boundary layer of a plate in a longitudinal flow. Figure 3.13 shows the result of the calculated laminar plate boundary layer in comparison with the analytical solution of Blasius:

$$c_f(x) = \frac{0.664}{\sqrt{Re(x)}}, \tag{3.32}$$

for various *spatial discretizations*. Here $Re(x) = \rho \cdot U_\infty \cdot x/\mu$ is the local Reynolds number formed with x. The dimensionless wall shear stress $c_f = \tau_w/((1/2) \cdot \rho \cdot U_\infty^2)$ is in agreement for all discretization schemes tested.

The two-dimensional turbulent plate boundary layer without a pressure gradient is an important example for verification and validation for the adaption of *turbulent models*. By means of a correspondingly fine computational grid the effect of the discretization error on the numerical solution can be kept very small. The Reynolds number is $Re_L = 2 \cdot 10^6$ and the degree of turbulence is precribed with $Tu_\infty = 0.5\%$. The transition is fixed with a Reynolds number of $Re_\delta = 770$ formed with the momentum-loss thickness. For these parameters the average velocity profile at the position $x/L = 1$ and the variation of the friction coefficient C_f along the plate is compared in Figure 3.14 with experimental data.

The time-averaged velocity profiles calculated with the standard K-ϵ turbulence model and the quadratic K-ϵ model are slightly broader that the measured profile. However, this has no effect of the calculated friction coefficient c_f.

For verification of the software for the calculation of compressible *transonic wing boundary layers*, the flow past the two-dimensional RAE2822 wing is first calculated. This is used for verification of the spatial discretization and effect of the far-field boundary on the numerical results. There are experimental data for free streams with Mach number $M_\infty = 0.73$, the Reynolds number
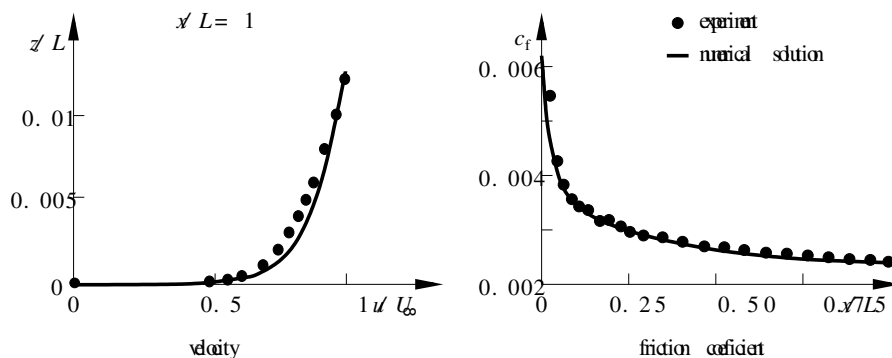
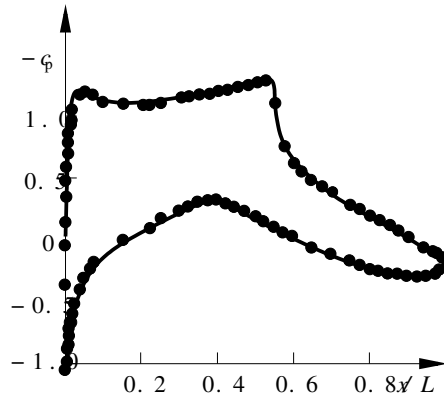Fig. 3.14. Turbulent plate boundary layer, $Re_L = 2 \cdot 10^6$

49

Fig. 3.15. Pressure distribution c_p of the transonic wing profile (RAE2822), $Re_L = 6 \cdot 10^6$, $M_\infty = 0.73$

$Re_L = 6 \cdot 10^6$ and for the angle of attack $\alpha = 3°$. Prescribing these parameters, fixing the transition at $x/L = 0.05$ and with the Baldwin-Lomax turbulence model, the calculated pressure distributions on the top side and under side of the profile are compared to experimental results.
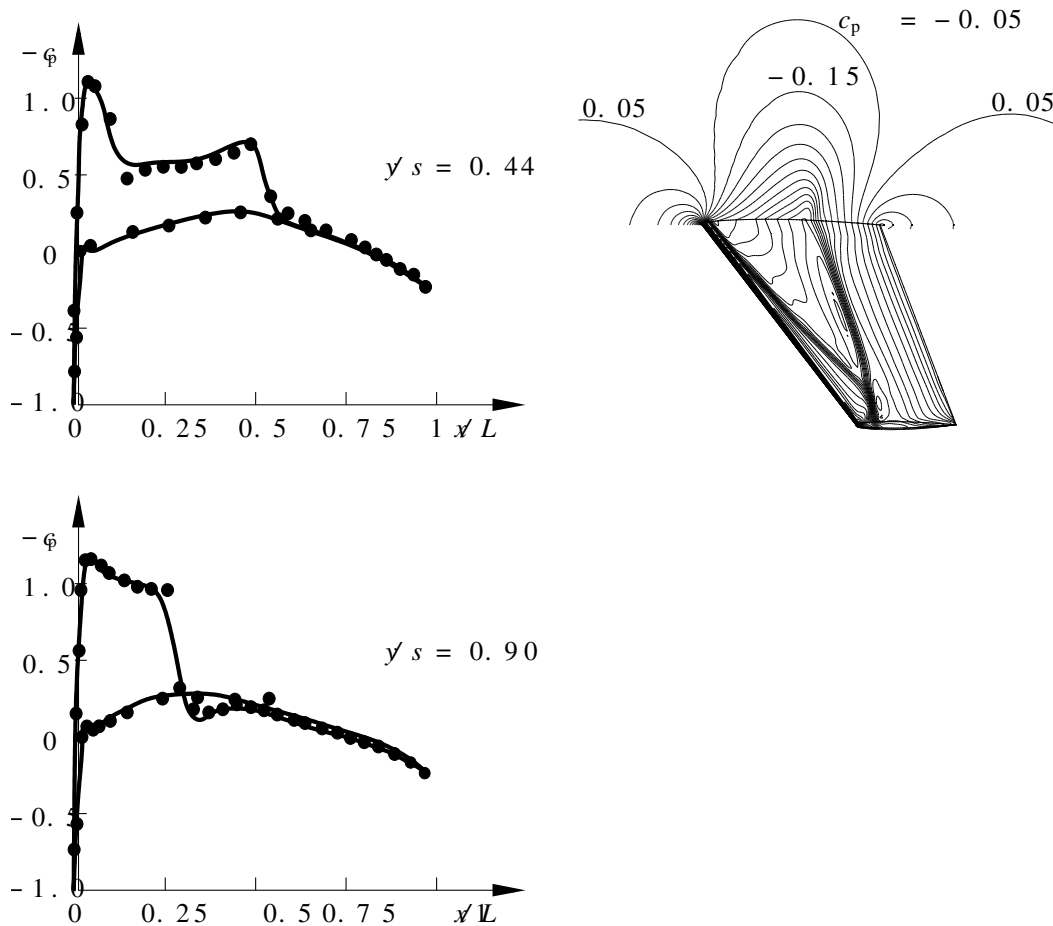

Fig. 3.16. Pressure distributions and isobars of the transonic wing (ONERA M6), $Re_L = 1.17 \cdot 10^7$, $M_\infty = 0.84$

The degree of turbulence in the free stream is $Tu_\infty = 0.3\%$. The turbulence length scale is estimated using the molecular viscosity and the Prandtl mixing length approach with

$$l_t \sim \frac{\mu}{\rho \cdot \sqrt{K_\infty}} \quad , \quad K_\infty = Tu_\infty \cdot U_\infty. \tag{3.33}$$

The pressure distributions of Figure 3.16 and the calculated shock position agree very well with the experimental values. The calculated lift coefficient $c_a = 0.795$ and the drag coefficient $c_w = 1.7 \cdot 10^{-2}$ are also in good agreement with experiment.

For the three-dimensional steady flow, the transonic flow past the test wing ONERA M6 is selected as the verification example. A double shock occurs on the suction side of this wing, which then merges to form one shock at the tip of the wing. The following data are selected for the free stream: Mach number $M_\infty = 0.84$, Reynolds number $Re_L = 1.17 \cdot 10^6$ and angle of attack $\alpha = 3.06°$. The numerical calculation is carried out using the Baldwin-Lomax turbulence model. The degree of turbulence is given with $Tu_\infty = 0.3\%$. To evaluate the solution, the results are compared with experimental data in various sections through the span of the wing.

In both sections the merging of the shock waves can clearly be seen in the computational grid used (see Figure 3.16). Because the finite-volume grid is too coarse, the shock waves merge too early on the wing. Close to the wing tip $y/s = 0.9$, apart from some insignificant merging of the shock waves, the pressure distribution is reproduced well compared to experiment.

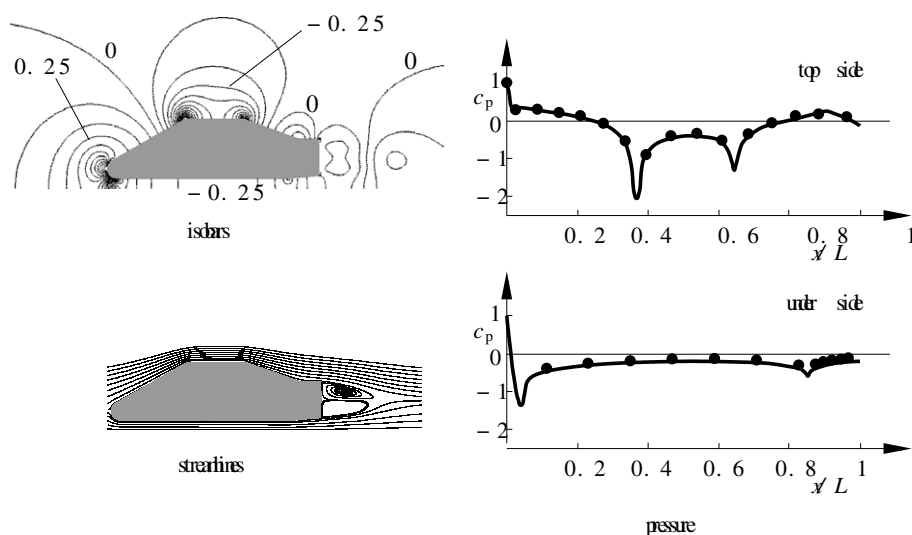The verification of the software for the *incompressible flow past a car* is carried

Fig. 3.17. SAE car body, $Re_L = 1 \cdot 10^7$

51

out with the SAE (Society of Automotive Engineering) model body, which the car industry has agreed upon. Using this, the effect of the computational grid and the various turbulence models on the lift and drag coefficients can be investigated systematically. The Reynolds number formed with the running length is $Re_L = 1 \cdot 10^7$, which corresponds to an unperturbed free stream velocity of $36m/s$ or $130km/hr$ and a length of the model body of $L = 4.2$. The turbulence quantities of the K-ϵ turbulence model are given as 1%. The logarithmic law of the wall is carried forward into the viscous sublayer of the boundary layer and correspondingly adapted, so that the calculation of the integral coefficients is possible to a first approach, even without resolving the viscous sublayer. To improve in particular the calculated lift coefficient, the two-layer turbulence model is used to ensure that the viscous sublayer is taken into account.

Figure 3.17 shows the calculated isobars and pressure distributions of the model body on the top and under sides each in the mid section. Starting from the stagnation point ($c_p = 1$), the flow accelerates on the upper side until the front edge of the roof is reached ($c_p = -2$). After this the flow decelerates and then accelerates again to the back edge of the roof. Finally the flow decelerates in the direction of the lid of the trunk. On the under side the flow accelerates, starting from the stagnation point, and then decelerates along the undercarriage. The start of the diffusor can be clearly recognized with the small suction peak. The calculations with different computational grids show that the necessary independence from the finite-volume computational grid is achieved at about 4 million cells, and the calculated pressure distributions agree with the experimental values, as long as the wing tunnel geometry is taken into account in the calculation and discretized with about 4.8 million cells.

Two-equation turbulence models used with an optimal computational grid lead to only small variations in the calculated lift and drag coefficients. The calculated drag coefficient in the wind tunnel is $c_w = 0.169$ in comparison to the experimental value of $c_w = 0.165$. For the lift coefficient, the variations are larger. The calculated value for the front axle lift $c_a == 0.116$ is compared to the measured value of $c_a = -0.136$. For the back axle lift $c_a = -0.036$ is calculated and $c_a = -0.151$ is measured. In the experimental values, the usual wind tunnel corrections such as boundary-layer suction and a moving band are not taken into account.

The classical verification example for the calculation of an unsteady *wake flow* is the laminar and turbulent Kármán vortex street of a cylinder in a flow, which has already been used in the previous sections. Here the most important thing is the analysis of the time accuracy of the software. The Reynolds number formed with the cylinder diameter D for the laminar flow past a cylinder is $Re_D = 500$.

Figure 3.18 shows a snapshot of the velocity distribution and the change in time of the u component of the velocity for the laminar Kármán vortex street in comparison to the turbulent Kármán vortex street at a Reynolds number $Re_D = 1.4 \cdot 10^4$. The calculated Strouhal number $Str = f \cdot D/U_\infty = 0.22$ agrees with the experimental value $Str = 0.20 - 0.22$ for the laminar Kármán vortex street. The drag coefficient is calculated in agreement with experiment as $c_w = 1.3$. This provides confirmation of the time accuracy of the software and of the drag coefficient for unsteady flow past a cylinder.

With turbulent flow past a cylinder, the effect of different turbulence models for unsteady flows can be demonstrated. The Reynolds number $Re_D = 1.4 \cdot 10^4$ is given, and various two-equation turbulence models are tested for unsteady turbulent flow.

It turns out that the standard K-ϵ turbulence model is not suitable for calculating turbulent vortex shedding because of the assumed isotropy. For this reason the quadratic K-ϵ turbulence model is used. For the degree of turbulence $Tu_\infty = 0.5\%$ is given and for the length scale $l_\infty = 0.01$. The calculated drag coefficient $c_w = 1.3$ is in agreement with experiment. The calculated Strouhal number $Str = 0.235$ is 10 % higher than the experimental value $Str = 0.2$. This is because the transition from the laminar boundary layer on the surface of the cylinder to the turbulent wake is not correctly modeled by the quadratic turbulence model.

Calculation of the vortex street at the Reynolds number $Re_D = 5.25 \cdot 10^5$ in the transition region to the turbulent boundary layer on the cylinder yields
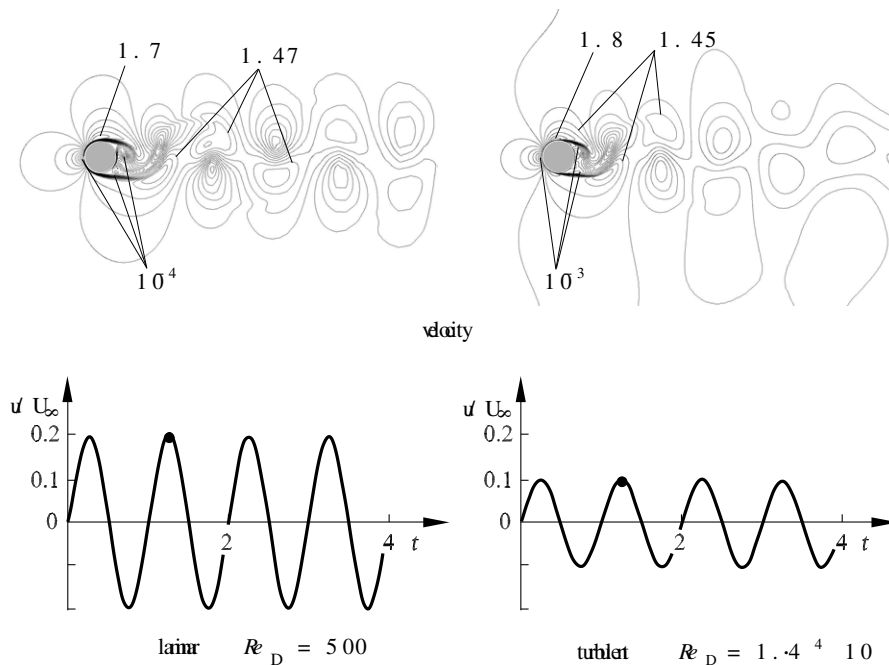
Fig. 3.18. Laminar and turbulent Kármán vortex street

53

agreement of the values of the Strouhal number $Str = 0.21$.

Verification of the software for steady flow past three-dimensional bodies is carried out using the example of *flow past a sphere.* At the selected Reynolds number $Re_D = 5.25 \cdot 10^5$ the boundary layer on the sphere separates transitionally and passes via a transition process into the turbulent wake. Therefore it is useful to calculate the laminar flow past the sphere up to the separation line using the Navier-Stokes equations and the finite-volume method, and in the turbulent wake to use coarse structure direct numerical simulation DNS of the periodically separating turbulent ring vortices.

Another possibility for the calculation is time-precision solution of the Reynolds equations and adaption of a suitable turbulence model. To calculate the flow past the sphere, the nonlinear low-Reynolds-number K-ϵ and K-ω turbulence models are selected. In the laminar region of the boundary-layer flow on the sphere, with Reynolds-averaged simulation calculations, the prescribed degree of turbulence $Tu_\infty = 1\%$ and the characteristic turbulence length $l_\infty = 0.1$ are retained. The computational grid consists of $2.9 \cdot 10^6$ grid points.

Figure 3.19 shows the calculated pressure distribution in the azimuthal direction on the sphere, in agreement with experimental values, as well as the calculated isotachs and streamlines. In the wind tunnel experiment the sphere is held with a rod in the wake. The simulation results shows that the flow separation on the sphere is predicted too late by the K-ϵ turbulence model and too soon by the K-ω turbulence model. This leads to deviations in the pressure distribution on the back side of the sphere.
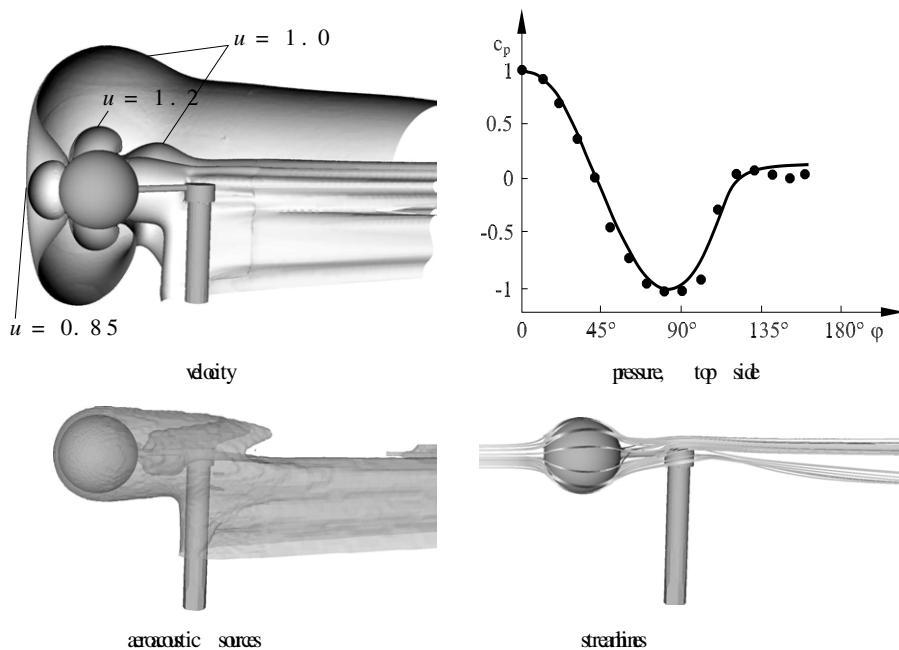

Fig. 3.19. Flow past a sphere, $Re_D = 5.25 \cdot 10^5$

If it is only the integral coefficients of the unsteady flow past a sphere that are of interest, there is also the possibility to determine the quasi-steady solution directly (as is required for the stability analysis) without precise time solution. These results are shown in Figure 3.19. In addition to this the iso-surfaces of the quadrupole acoustic noise determined from the quasi-steady solution are shown; these will be necessary in Section 4.3 on the resonator.

Therefore, depending on the problem, the three different numerical models as described can be applied for the calculation of the flow past three-dimensional bodies.

A verification example for turbulent unsteady internal flow is the three-dimensional flow past a *stagnation body* in a pipe flow, as will be treated in Section 4.2.4. The stagnation body shown in Figure 3.20 is in a fully developed turbulent pipe flow. The diameter ratio of pipe to stagnation body is $D/d = 3.6$. At the wall of the pipe a horseshoe vortex forms around the stagnation body, which then passes over into the periodic vortex shedding in the wake of the stagnation body.

The flow calculation is carried out with the nonlinear low-Reynolds number K-ϵ turbulence model with a hybrid law of the wall and a correspondingly fine grid in the wall boundary layer. In the fully developed pipe flow a degree of turbulence of $Tu_\infty = 5\%$ and the turblence length $l = 0.01m$ are given. Figure 3.20 shows the snapshot lines of the vorticity and the dependence of the constant value of the Strouhal number $Str = 0.237$ on the Reynolds number, which can be used for the measurement of the volume flow in the pipe. The small systematic variation between the simulation calculation and the experiment lies within the measurement error tolerance of 5 %.
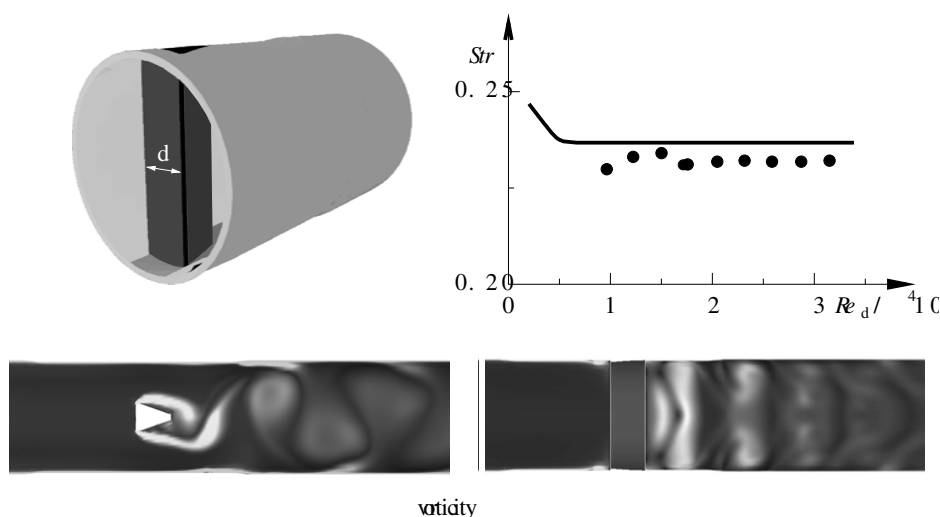

vorticity

Fig. 3.20. Stagnation body in a pipe flow

55

Absolutely unstable *resonators* are responsible for the onset and expansion of fluid-mechanically generated noise in piping systems. The pipe flow with two screens that form a resonator is selected as the verification example for the software with respect to the localization of acoustic noise. Figure 3.20 shows the geometric arrangement as well as the result of direct numerical simulation DNS of the Navier-Stokes equations. The pipe has a diameter of $D = 5 \cdot 10^{-2} m$ with the Reynolds number $Re_D = 1.7 \cdot 10^4$ at the average velocity $u_m = 5 m/s$. The inner diameter of the screens is $D_B = 2.8 \cdot 10^{-2} m$. The screens each produce a periodic vortex shedding, which causes the indicated frequency spectrum of the noise expansion. The velocity profile and the turbulent kinetic energy are given via a fully developed velocity profile. Particular formulation of the boundary conditions avoids reflection of the sound waves at the free ends of the flow region.

Depending on the distance L between the two aperatures, after the flow separates at the first aperature a characteristic interaction and reflection occur with the second aperature. As well as the classical quadrupole noise of the shear flow, there there is also the tonal component of the screen resonator. Figure 3.21 shows for $L = D$ a snapshot of the streamlines in the pipe cross-section. For further aeroacoustic evaluation, the frequency spectrum of the pressure is shown at three characteristic positions. One location for evaluation is between the aperatures. The other two locations are at a distance D in front of the first aperature and after the second cross-sectional narrowing, respectively. The frequency spectra evaluated with direct numerical simulation DNS are in agreement with the spectra measured by experiment.
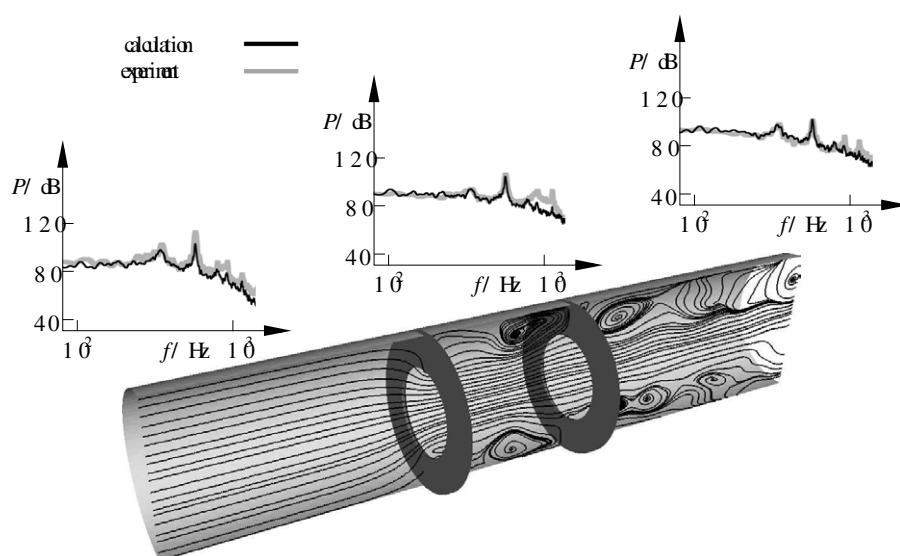

Fig. 3.21. Aeroacoustic resonator

Validation of the stability theory model of absolute instability and its application for flow control is carried out with the perturbation cylinder experiment in the wake of the flow past a cylinder, as described in Chapter 1 and Section 3.2. Periodic vortex shedding behind circular cylinders can be reduced by suitable placing of a second, smaller perturbation cylinder in the absolutely unstable region of the wake. Introducing the perturbation cylinder means that the time amplified perturbations in the part of the wake close to the cylinder are supressed, so that a convectively unstable wake occurs.

For the validation the free, two-dimensional and incompressible flow past a cylinder with diameter D, shown in Figure 3.22, is calculated. At the intake a constant velocity U_∞ is prescribed. At the side walls the absence of stress is forced by means of the natural boundary condition $\sigma_{ij}n_{ij} = 0$. At the outlet a constant pressure is prescribed, while the no-slip condition holds on the surface of both cylinders.

The position of the perturbation cylinder with diameter d is selected in accordance with the experimental setup of *P.J. Strykowski* 1990 as $x_S = 1.2D, y_S = 1.0D$. The ratio of the diameters of the two cylinders is $D/d = 10$. The geometrical grid is set up with the software package COMSOL, described in Section 3.2, using triangular cells. The number of degrees of freedom is initially increased successively in preliminary investigations, until the calculated eigenvalues no longer indicate any dependence on the grid.

The basic flow used for the global stability analysis are the calculated quasi-steady flow fields. Figure 3.23 shows isolines of vorticity for the two basic flows with and without the perturbation cylinder, respectively, at a Reynolds number of 55. These indicate a very good agreement with the streamlines of Figure 3.11.

The eigenfunctions of the two velocity components of the configurations with
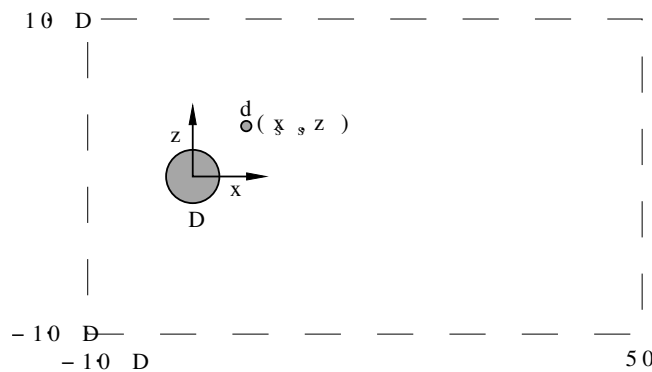

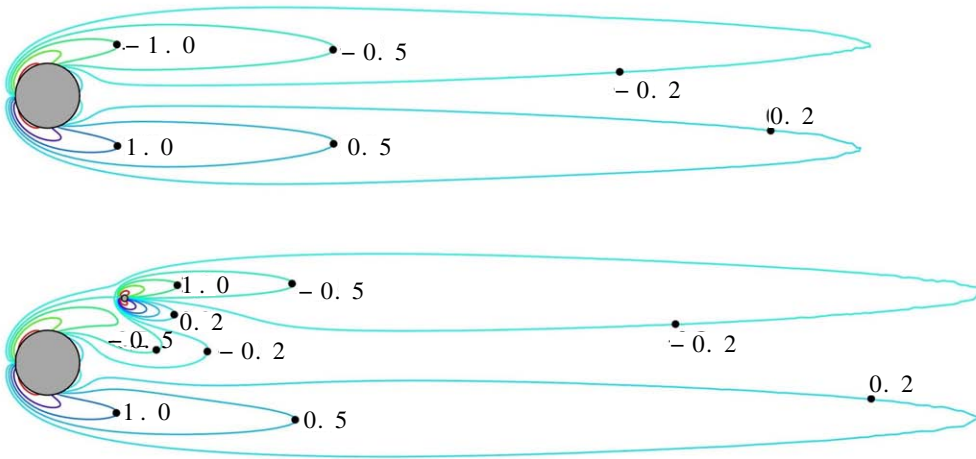Fig. 3.22. Arrangement of cylinder and perturbation cylinder

Fig. 3.23. Isolines of vorticity of the quasi-steady solution with and without perturbation cylinder, $Re_D = 55$

and without perturbation cylinder that are associated with the most unstable eigenvalue are shown in Figure 3.24 for $Re_D = 55$.
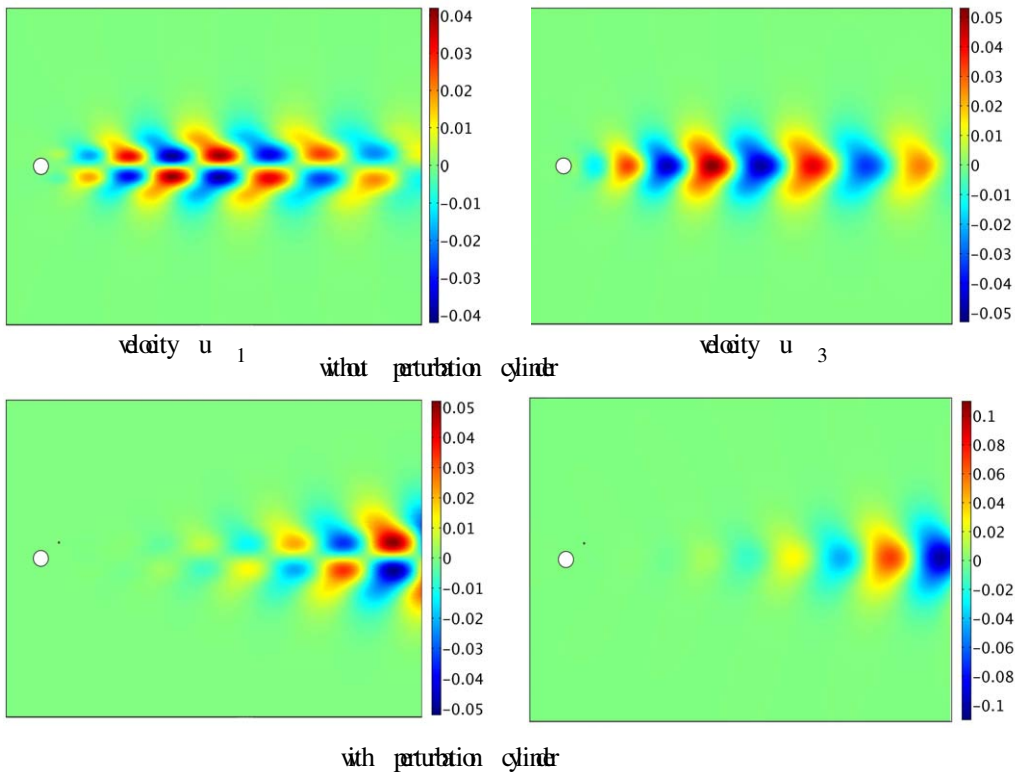

Fig. 3.24. Eigenfunctions of the amplified and damped eigenvalue of the flow past a cylinder without and with a perturbation cylinder, $Re_D = 55$

The eigenvalue in the case without the perturbation cylinder, for the Reynolds number given here, leads to an amplification of the perturbation. After the perturbation cylinder is introduced the initially absolutely unstable region becomes convectively stable. The calculated eigenvalue signals a stable flow. In the configuration with a perturbation cylinder the periodic vortex shedding occurs only at higher Reynolds numbers.

Following this, the Reynolds number of the flow past the circular cylinder with and without the perturbation cylinder is varied incrementally and compared with the experimental values. In order to guarantee that the results can be compared with the experimental results, the amplification rate λ_r is made dimensionless:

$$A = \frac{-\lambda_r \cdot D^2}{\nu}. \tag{3.34}$$

The dimensionless amplification rate is shown in Figure 3.25. Without a perturbation cylinder there is very good agreement of the calculated amplification rates with the experimentally determined values. The perturbations superimposed on the basic state decay as long as the real part of the eigenvalue is positive. If the sign changes the initially stable state becomes unstable. Therefore the critical Reynolds number can be determined from the root of the real part of the eigenvalue. For the flow past the cylinder the critical Reynolds number is $Re_{\mathrm{crit}} = 45.5$. The critical Reynolds number is also in good agreement with the experimentally determined value of 46.0.

For the flow past a cylinder with perturbation cylinder, the change in amplification rate as determined by the global stability analysis is also in good agreement with the experimental results. In principle, however, the calculated amplificate rates are smaller than the experimentally determined values.

The calculated and measured frequencies of the periodic vortex shedding can-
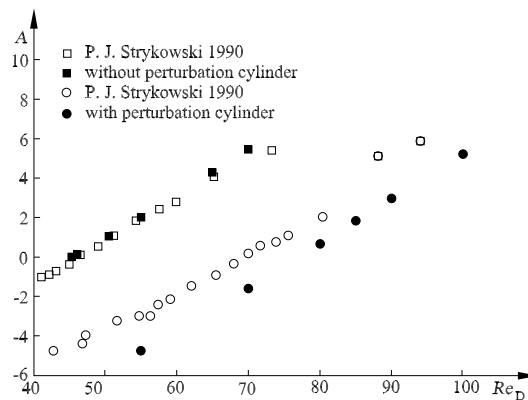

Fig. 3.25. Dependence of the rates of amplification on the Reynolds number

not be compared directly, as corresponding to Figure 3.2 the linear stability analysis calculates the frequency of the quasi-steady basic state. The experiment, however, measures the frequency in the nonlinear saturation region, which differs in order of magnitude by 10 %.

4　Flow Control Applications

Now that the theoretical fundamentals of the stability analysis of local perturbations and the stability theory concept of absolute instability for flow control have been introduced, the practical application of convectively unstable boundary-layer flows and absolutely unstable wake flows follows. The laminar–turbulent transition in a boundary-layer flow takes place via the transition process described in Chapter 2, which can be controlled by means of a suitable pressure distribution to ensure a transonic laminar wing. The periodically oscillating wake flow was described as a resonator phenomenon in the absolutely unstable region, which can also be controlled via a suitable pressure distribution at the rear of a car of by means of blowing (base bleed) or suction at the back. This stability theory concept of a fluid-mechanical resonator can also be transferred to fluidic oscillators.

4.1　Boundary Layer

4.1.1　Transition

In accordance with the description in Section 2.1, for a three-dimensional boundary layer on a swept transonic wing, downstream it is Tollmien-Schlichting waves and along the stagnation line it is cross-flow instabilities that determine the laminar–turbulent transition. In addition to the stability analysis, direct simulation of the transition process up to turbulent boundary-layer flow by numerical solution of the compressible Navier-Stokes equations DNS has also been performed. Figure 4.1 shows the simulation results of the *Tollmien–Schlichting transition* and the *transition of the cross-flow vortices* in a three-dimensional wing boundary layer at Mach number $M_\infty = 0.62$ and Reynolds number $Re_L = 26 \cdot 10^6$. Contour surfaces of the rotation $\omega_i = \frac{\partial}{\partial x_i} \times u_i$ are shown. The transition process of the Tollmien–Schlichting waves begins with downstream traveling plane waves. As in Figure 2.5, three-dimensional perturbations are superimposed, and Λ-structures form. The Λ-structures are regions of local shearing and excess velocity in the peaks. They are lined up periodically in the span and form several rows periodically ordered behind each other. The occurrence of the Λ-structures is associated with the appearance of strong free-shear layers. These are prominent local maxima of the shear stress far from the wall. As the transition proceeds, the high shear rates decay into increasingly smaller structures, leading eventually to the turbulent state. The decay of the shear layers takes place within a few wavelengths of the Tollmien–Schlichting waves.

The mechanisms of the transition process of cross-flow vortices are similar.

Figure 4.1 shows the formation of the Λ-structures associated with high shear rates and fluctuation in the perturbation quantities in the peaks. In the final state of the transition, they decay within a short distance into a turbulent boundary-layer flow.

Figure 4.2 shows a sketch of local perturbations of the Tollmien–Schlichting transition and the transition of cross-flow instabilities in the three-dimensional boundary layer of a swept transonic wing. Both instabilities are convectively unstable in the boundary layer.

In what follows the behavior of three-dimensional wave packets in a three-dimensional compressible boundary layer is briefly analyzed. In contrast to the investigation into two-dimensional perturbations, the transverse wave number b now also appears in the dispersion relation function $D(\omega, a, b)$, whose roots

transition of Tollmien–Schlichting waves

transition of cross–flow vortices
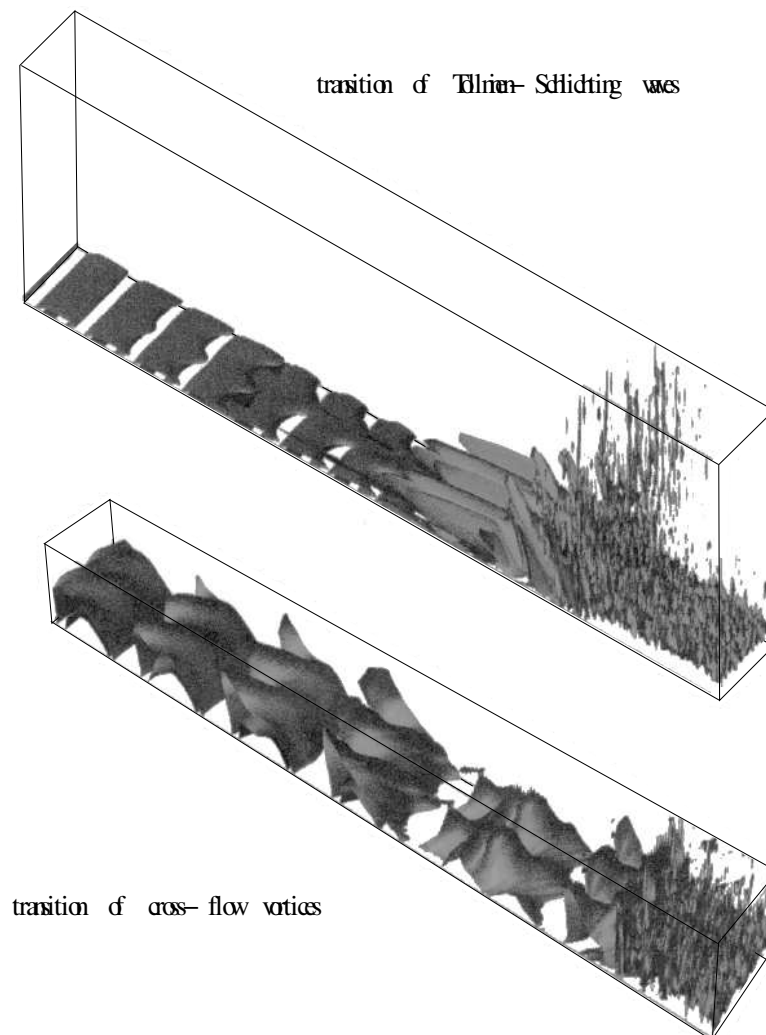
Fig. 4.1. Laminar–turbulent transition in the compressible wing boundary layer, $M_\infty = 0.62$, $Re_L = 26 \cdot 10^6$
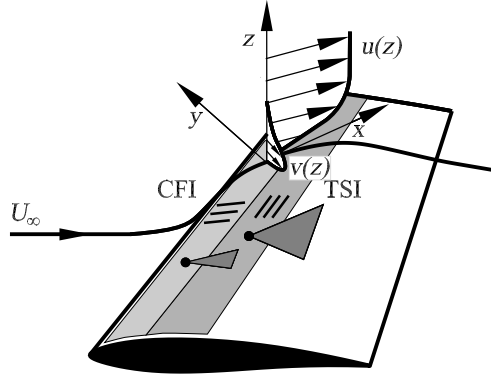
Fig. 4.2. Local cross-flow (CFI) and Tollmien–Schlichting instabilities (TSI) in the three-dimensional boundary layer of a swept wing

are indeed given by those combinations (ω, a, b) representing the solutions of the stability eigenvalue problem for complex ω, a, b. The change in amplitude of a perturbation wave packet in the plane reference frame, moving with the group velocity (U, V) is considered. The frequency observed is then

$$\omega' = \omega - a \cdot U - b \cdot V. \tag{4.1}$$

As in the two-dimensional case, again those waves whose group velocity vector $(\partial\Omega/\partial a, \partial\Omega/\partial b)$ is real have to be found. The complex frequency function $\Omega(a, b)$ is then defined by $D(\Omega(a, b), a, b) \equiv 0$. The relative temporal amplification ω'_i is then plotted, not just as a function of $U = \partial\Omega/\partial a$, but also in the group velocity plane (U, V). The line of height $\omega'_i = 0$ is of particular interest, since it encloses the region in the (U, V) plane in which $\omega'_i > 0$. Therefore, this region represents the parts of the perturbation that contribute time-asymptotically to the wave packet. Figure 4.3 contains diagrams with the regions of temporal amplification at two representative positions on a swept wing. The lower diagram in the figure shows a typical curve $\omega'_i = 0$, which
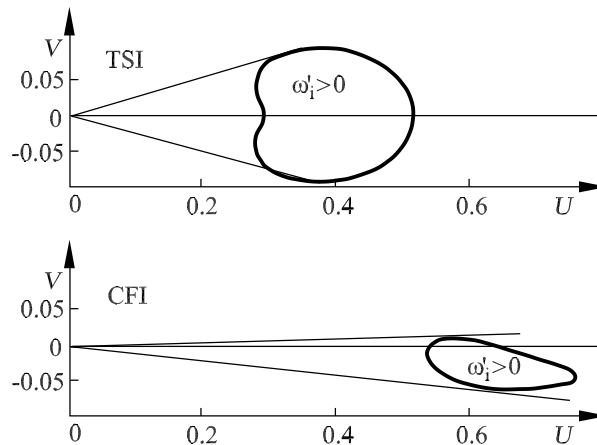

Fig. 4.3. Regions of relative temporal amplification of the Tollmien–Schlichting instabilities (TSI) and cross-flow instabilities (CFI) in the group velocity plane (U, V)

is computed for a position close to the leading edge of the swept wing, i.e. in the cross-flow instability region. The upper diagram shows the same curve at a position further downstream on the wing, where Tollmien–Schlichting instabilities are present. It can be seen that both instabilities have convective character, since in both cases the origin $(U, V) = (0, 0)$ is not contained in the $\omega_i' > 0$ region. The growing perturbation energy is transported downstream in both cases. The tangents at the curves $\omega_i' = 0$ determine the angular region within which these amplified perturbations remain. In the case of the cross-flow instabilities, the angular range is very narrow and lies essentially downstream. Note that the associated instabilities are waves that travel practically perpendicular to the downstream direction. This clearly indicates the fundamental difference between group velocity and phase velocity.

As it was determined that the cross-flow instabilities are convective in nature and that they induce a spatially extended transition process downstream, the associated spatial wave packet amplification rates ($g_{max} = [(\omega_i - a_i \cdot U - b_i \cdot V)/ \sqrt{U^2 + V^2}]_{max}$) for the transonic swept-wing boundary layer were computed. Figure 4.4 shows the eigenvalues, eigenfunctions, and unstable regions of wave packet perturbations for angles of sweep from 15° to 25°. In developing a swept laminar wing, it is essential to avoid cross-flow instabilities, since they induce a transition process already directly at the leading edge. Using the
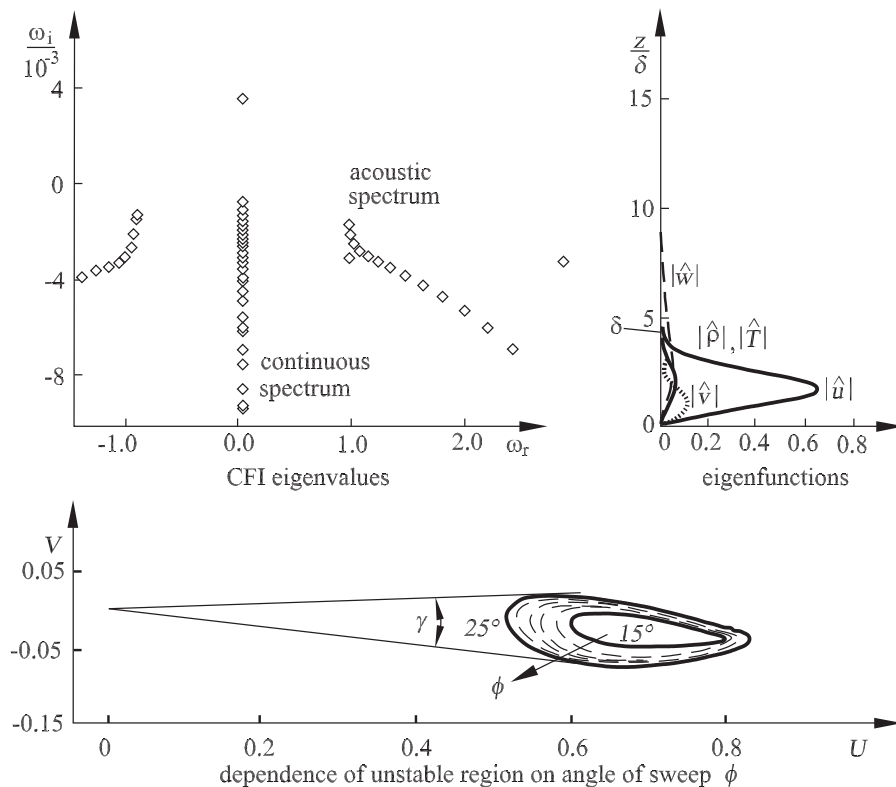

Fig. 4.4. Eigenvalues, eigenfunctions, and unstable regions of the cross-flow instability in the compressible boundary layers of swept wings, $M_\infty = 0.78$, $Re_L = 26 \cdot 10^6$

methods of stability analysis, the range of the design parameters of a swept wing can be determined within which active control measures are not needed (corresponding to the natural laminar behavior). One of these parameters is the angle of sweep. In an otherwise identical free stream, there is a critical range of angle of sweep within which the transition process changes from TSI-dominated to CFI-dominated (Figure 4.2). Stability theory therefore yields a limit for the angle of sweep of a laminar transonic wing.

4.1.2 Laminar Wing

Transonic civil aircraft fly with so-called supercritical profiles. The shape of the front region of the wing was chosen so that the subsonic regime is extended downstream and a weakened shock wave occurs in the rear region of the wing. The resultant pressure distribution for a free-stream Mach number of 0.75 is shown as a dashed line in Figure 4.5. If the friction drag c_f of the wing is to be reduced, the wing has to be shaped so that the laminar–turbulent transition in the wing boundary layer is shifted downstream. In addition, the suction tip on the upper side of the wing has to be avoided and a continuous acceleration as far as the shock wave achieved. Such a pressure distribution is shown in Figure 4.5 as a heavy line. It leads to smaller leading-edge radii and steeper pressure increases at the trailing edge. The shape of the profile is chosen so that the onset of the Tollmien–Schlichting waves TS is shifted downstream into the shock–boundary-layer interaction region. The sweep of the wing also has to be reduced so that no cross-flow instabilities occur at the leading edge. The solution of the Reynolds equations for such a *laminar wing* at the transonic free-stream Mach number 0.78 is shown in Figure 3.6. A sweep angle of $\phi = 20°$ is chosen, at which the amplification rate of the cross-flow instabilities close to the leading edge is considerably smaller than the amplification rate
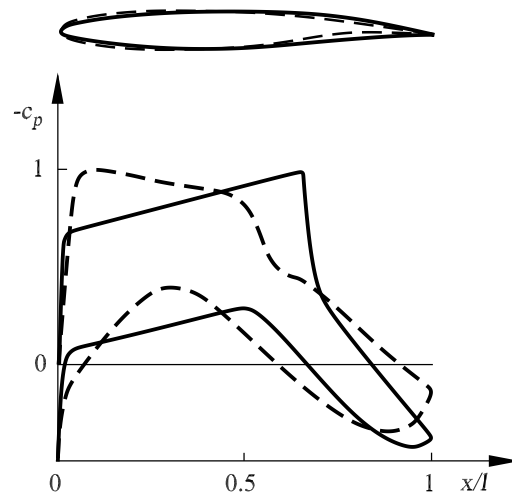

Fig. 4.5. Conventional supercritical profile and laminar profile, $M_\infty = 0.75$, $c_a = 0.5$, $\mathrm{Re}_l = 25 \cdot 10^6$
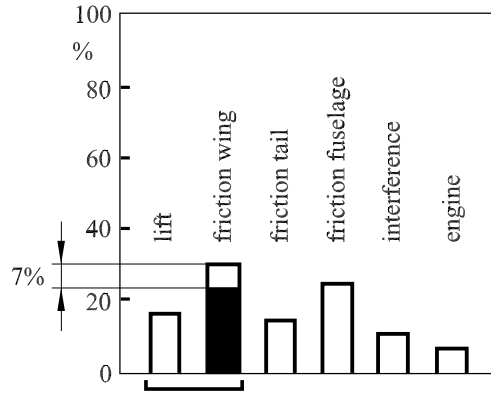
Fig. 4.6. Drag contributions of a civil airplane

of the Tollmien–Schlichting instabilities. The laminar boundary-layer flow is retained right into the shock–boundary-layer interaction region. The extended supersonic region on the transonic wing is concluded by a weak shock wave.

The drag contributions for the entire airplane are summarized in Figure 4.6. The contribution due to the wing is 46%. By making the selected wing laminar, a decrease of 15% in the drag is attained, as shown in the polar diagram of Figure 4.7 (*H. Oertel, R. Stauk* 1998). For the airplane this means a reduction potential of about 7%.

An important result of the stability analysis is the areas of spatial amplification of local cross-flow disturbances in the group-velocity plane of Figure 4.4 at different angles of sweep and at the wing position where the spatial amplification rate is maximal near the stagnation line ($x/L \approx 0.0015$) .

The area of amplified disturbances in the group-velocity plane is enclosed by different neutral curves $g = 0$ calculated for the corresponding angles of sweep. The zero point of the group velocity is not located within the unstable region,
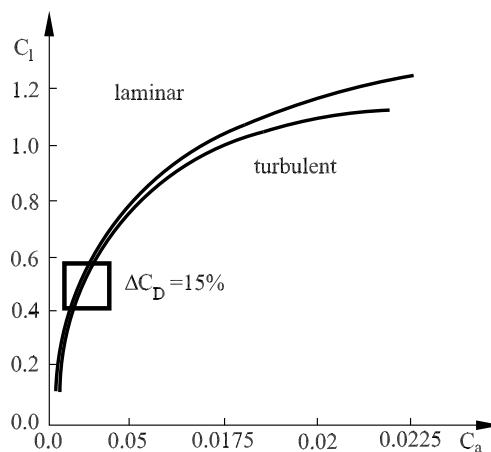

Fig. 4.7. Drag polars of the laminar and turbulent swept wing, $\Phi = 20°, M_\infty = 0.78, Re_L = 26.6 \cdot 10^6$

66

and so the perturbation energy does not remain at the location of its origin, but is convected downstream with the mean flow. This result shows that the instability mechanism of the flow is convective instability. Furthermore it can be seen that the disturbances remain within a small wedge-shaped range of the acute angle γ, which increases with increasing angle of sweep Φ. For an angle of sweep $\Phi = 15°$, the corresponding acute angle γ within which the disturbances remain amounts to $\gamma \approx 4.0°$, and increases to $\gamma \approx 9.2°$ for an angle of sweep of $\Phi = 25°$.

In conclusion it can be said that a transonic laminar swept wing can only be realised for a certain range of angles of sweep. At realistic angles of sweep of $\Phi = 30°$ to $\Phi = 35°$, the cross-flow disturbances have to be suppressed, for example by suction near the stagnation line of the wing.

4.2 Wake

4.2.1 Flow Control

The basics of flow control in the absolutely unstable wake flow has been described in the previous chapters, with the suction in Figure 1.1, the perturbation cylinder in Figures 1.4 and 3.23, as well as with the base bleed into the wake flow in Figure 3.11. A prerequisite is knowledge of the dependence of the various laminar and turbulent flow structures behind blunt bodies on the Reynolds number Re_D. Following on from the flow past a sphere of diameter D in Figure 3.18, the Reynolds number dependence of the drag coefficient $c_w(Re_D)$ (Figure 4.8) and of the Strouhal number $Str = Str(Re_D)$ (Figure 4.9) are discussed.

The dimensionless shedding frequencey Str is defined as the ratio of the local acceleration to the convective inertia:

$$Str = \frac{\rho \cdot U_\infty / T}{\rho \cdot U_\infty^2 / D} = \frac{f \cdot D}{U_\infty}, \tag{4.2}$$

with the shedding frequency $f = 1/T$, the inverse of the period of oscillation T.

The discussion of the Reynolds-number dependence c_w starts first for Reynolds numbers $Re_D \leq 1$. At such Reynolds numbers, the friction forces dominate by far the inertial forces. This is a creeping flow, which can be described analytically. For the drag force W of a sphere in a steady flow at $Re_D \leq 1$, the analytical solution of the Navier-Stokes equation reads:
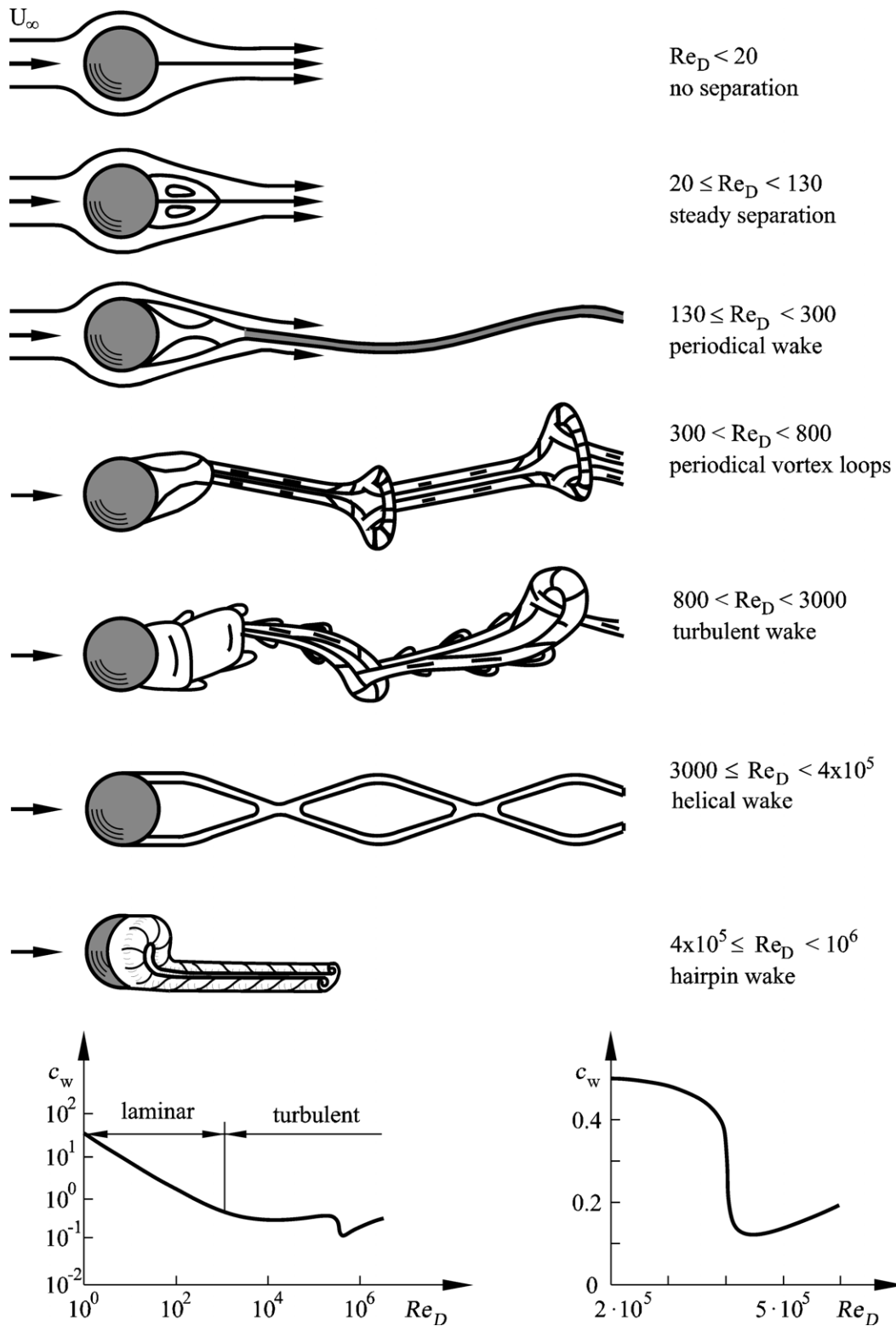
$\mathrm{U_\infty}$

$\mathrm{Re_D} < 20$
no separation

$20 \leq \mathrm{Re_D} < 130$
steady separation

$130 \leq \mathrm{Re_D} < 300$
periodical wake

$300 < \mathrm{Re_D} < 800$
periodical vortex loops

$800 < \mathrm{Re_D} < 3000$
turbulent wake

$3000 \leq \mathrm{Re_D} < 4\mathrm{x}10^5$
helical wake

$4\mathrm{x}10^5 \leq \mathrm{Re_D} < 10^6$
hairpin wake

Fig. 4.8. Dependence on the Reynolds number $Re_D = (U_\infty \cdot D)/\nu$ of flow shapes and drag coefficient c_w for a sphere in a flow

68

$$W = 6 \cdot \pi \cdot \mu \cdot \frac{D}{2} \cdot U_\infty. \tag{4.3}$$

One third of this drag force W originates in the pressure gradient and two thirds in the friction forces. Furthermore it is noteworthy that the drag force W in the creeping flow regime is proportional to the first power of the velocity of the free stream U_∞. Taking account of the definition of the c_w value, the following relation is obtained for $c_w = c_w(Re_D)$:

$$c_w = \frac{W}{\frac{1}{2} \cdot \rho \cdot U_\infty^2 \cdot \frac{\pi}{4} \cdot D^2} = \frac{24 \cdot \mu}{\rho \cdot U_\infty \cdot D} = \frac{24}{Re_D}. \tag{4.4}$$

The relation $c_w = (24/Re_D)$ is also called *Stokes' law* and is valid in the Reynolds number regime $Re_D < 20$.

If the Reynolds number is increased to a value of $Re_D = 130$, downstream from the sphere a state of steady flow separation is reached. Owing to the strong friction forces, the fluid particles directly at the wall lose so much kinetic energy that they are unable to offset the pressure increase in the back half of the sphere. This results in flow separation downstream from the equator of the sphere. A steady backflow region is found in the wake region directly behind the sphere. In calculating steady wake flows, the inertial terms can no longer be neglected and the full Navier-Stokes equations have to be solved.

At a Reynolds number $Re_D = 300$ the wake flow becomes unstable and a periodic wave-shaped wake forms. A further increase of the Reynolds number up to a value of $Re_D = 800$ first leads to unsteady periodic vortex shedding of the laminar boundary layer on the surface of the sphere with a laminar vortex street in the wake. Spiral vortex loops, also called hairpin vortices, form and propagate periodically in the wake. For Reynolds numbers larger than $Re_D = 420$, an irregular oscillation of the wake flow normal to the direction
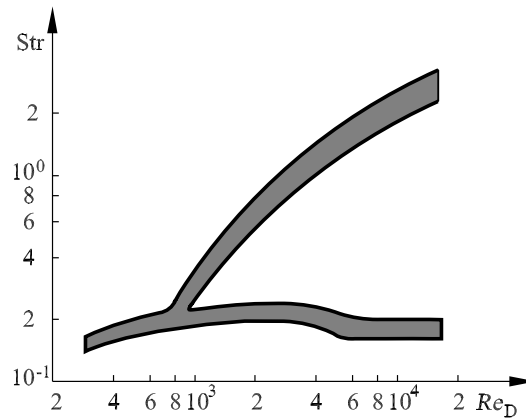

Fig. 4.9. Dependence on the Reynolds number Re_D of the dimensionless shedding frequency for a sphere in a flow

69

of flow is superimposed onto the periodic shedding of the vortex loops. The dimensionless shedding frequency is $Str = 0.18 - 0.2$.

At Reynolds numbers greater than $Re_D = 800$ the transition takes place to turbulent wake flow. First transitional and then turbulent, periodically shedding vortex loops form with a Strouhal number of $Str = 0.2 - 0.22$. In addition to the shedding frequency of the wake flow, a second, higher frequency arises (see Figure 4.9), which is caused by secondary instabilities of the local shear layers in the vortex loops. In the Reynolds number region $3000 \leq Re_D < 4 \cdot 10^5$ the discrete vortex loops are shed by periodic shedding of rotating ring vortices, which form a helical wave-like wake. The Strouhal number decreases until it reaches a constant value of $Str = 0.18 - 0.2$.

In the Reynolds number region $3 \cdot 10^5 \leq Re_D \leq 4 \cdot 10^5$, the boundary-layer flow on the sphere becomes turbulent. The shedding region is displaced downstream on the surface of the sphere and this causes a tapering of the wake flow. Associated with this is a drastic reduction of the c_w value from 0.48 to 0.12, as shown in Figure 4.8. The friction drag is greater for a turbulent boundary layer, so the drop in the c_w value is caused by the reduction in pressure drag. A time average of the flow portrait indicates horseshoe-like shedding of a vortex surface.

In the region $4 \cdot 10^5 \leq Re_D < 10^6$ the laminar–turbulent transition region moves forward on the surface of the sphere, and the friction drag increases,
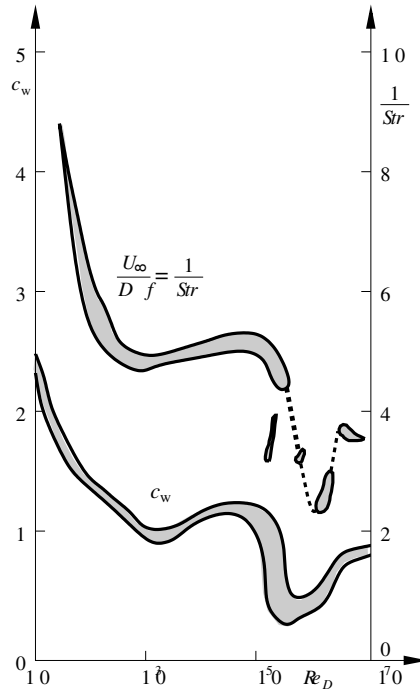

Fig. 4.10. Friction coefficient c_w and reciprocal values of the dimensionless shedding frequency $1/Str$ for the flow past a cylinder

70

while the pressure drag remains essentially constant. The c_w value therefore increases again. In the Reynolds number region $Re_D > 10^6$ the boundary layer on the surface of the sphere is turbulent downstream from the front stagnation point, thus fixing the shedding point, which no longer changes with further increase of the Reynolds number. The c_w value of the sphere therefore becomes independent of Re_D. A periodically oscillating and rotating streamline-shaped vortex pair forms in the turbulent wake.

The dependence of the friction coefficient c_w on the Reynolds number displays similar behavior for the *flow past a cylinder*. Figure 4.10 shows all known experimental values c_w together with the measured reciprocal values of the dimensionless shedding frequency $1/Str$. Figure 4.11 completes the flow portrait for the flow past a cylinder for the region of steady flow separation in the Reynolds number region $3 \leq Re_D < 40$ and the region of the laminar von Kármán vortex street $40 \leq Re_D \leq 200$.

The periodic vortex shedding of the von Kármán vortex street commences at the Reynolds number $Re_D = 40$. With increasing Reynolds number $1/Str$ decreases sharply, the shedding frequency increases correspondingly, in order to take on almost constant values of $Str = 0.21$ at Reynolds numbers between 10^3 and 10^5. With the transition to turbulent boundary-layer flow on the cylinder, $1/Str$ drops sharply in accordance with the drop in drag coefficient c_w. For Reynolds numbers greater than 10^7 a constant shedding frequency is also found in the turbulent wake flow for constant c_w values, as the laminar–turbulent transition in the boundary layer of the cylinder has moved
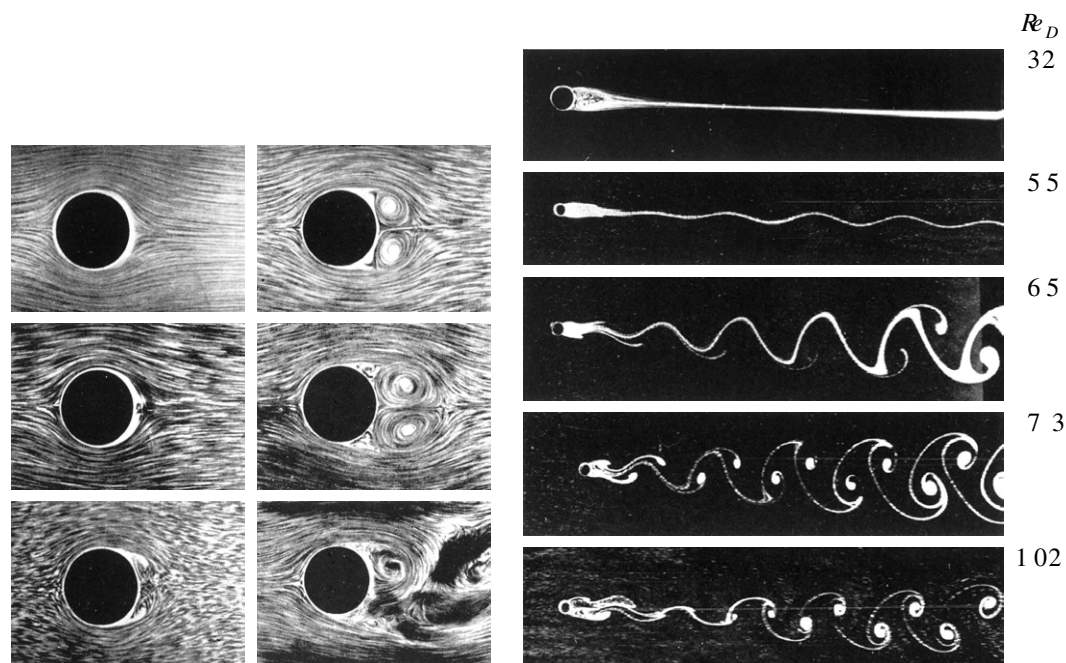

Fig. 4.11. Flow past a cylinder and laminar von Kármán vortex street

71

to the stagnation point and no change of the turbulent flow is found for further increasing Reynolds number. For the Reynolds number region of 10^4 to 10^5, Figure 4.12 summarizes various three-dimensional and two-dimensional shapes and the dependence of the drag coefficient c_w on the Reynolds number extended for various rotationally symmetric bodies.

The circular disk has its greatest drag for turbulent Reynolds numbers. As the flow separation is fixed by the geometrically determined trailing edge, the drop-off in the drag at Reynolds number $4 \cdot 10^5$ does not occur. For ellipsoids this drop-off is shifted to smaller Reynolds numbers because of the body shape. For streamline bodies the drop in the drag also does not occur, as the laminar–turbulent transition takes place initially in the boundary layer on the body and then moves continuously into the wake.
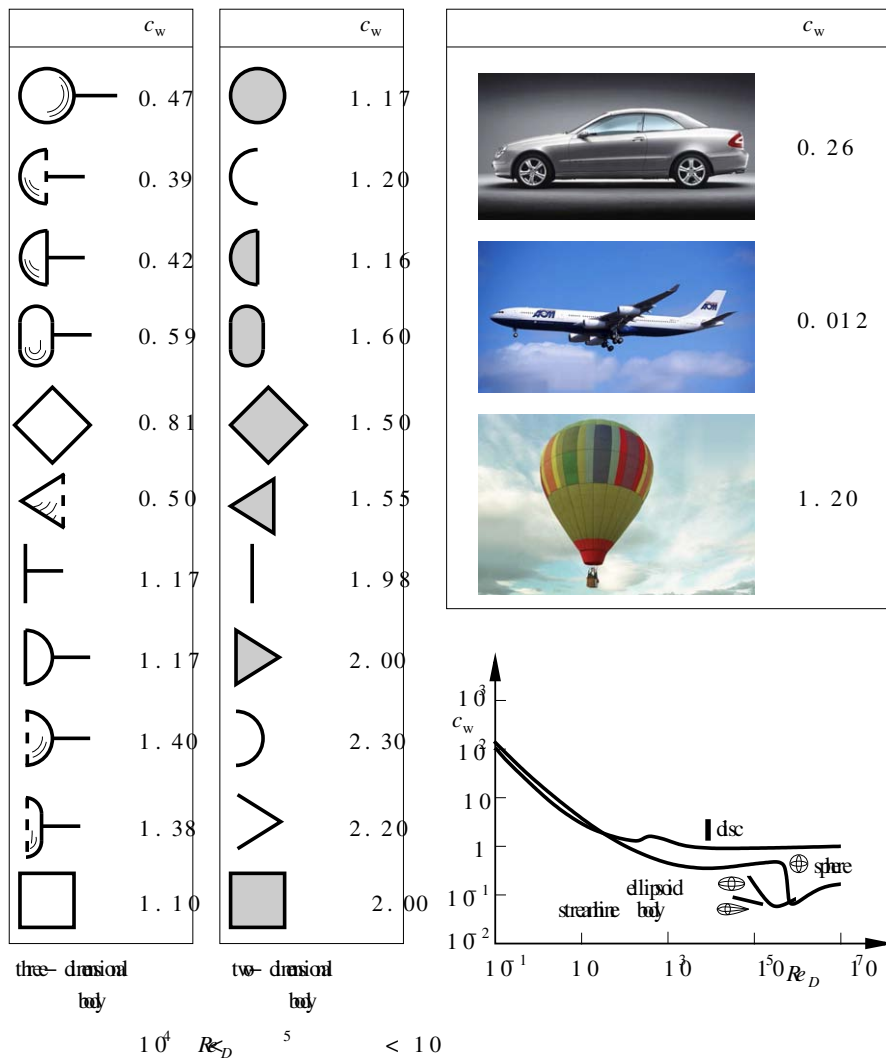

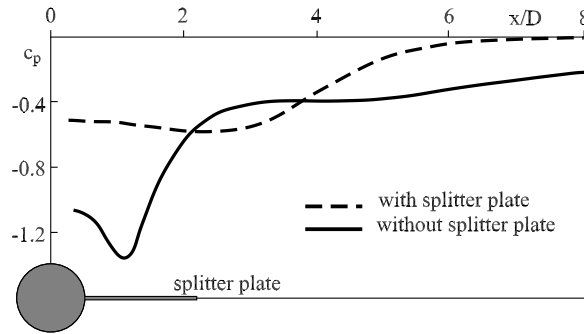Fig. 4.12. Drag coefficients of blunt bodies

Fig. 4.13. Wake control by splitter plates

4.2.2 Elastic Splitter Plate

One common method in aerodynamics to suppress the periodically oscillating wake flow is to place a splitter plate in the wake of the cylinder, and so to suppress the absolutely unstable region. Figure 4.13 shows the pressure coefficient c_p without and with a splitter plate. It is clear that the pressure drag with no absolutely unstable wake is reduced. The question arises of how an elastic splitter plate behaves in the wake.

To this end a flow–structure coupled calculation of the flow field sketched in Figure 4.14 as well as a structure-mechanical calculation of the splitter plate are necessary. The necessary coupling algorithm and the structure-mechanical finite-element method are described in our textbook on biofluid mechanics *H. Oertel* 2008.

Figure 4.14 shows the geometrical arrangement of the cylinder with the elastic splitter plate in a channel. The velocity profile at the entrance to the channel is prescribed analytically. The slightly asymmetrical shape of the channel causes an initial perturbation and, above a critical Reynolds number $Re_D = 100$, an unsteady flow past the cylinder and the flexible structure forms, so that periodic oscillations are instigated in the latter. Whereas the laminar flow past a cylinder is absolutely unstable in the wake and vortices are shed periodically at the Reynolds number $Re_D = 40$, periodic vortex shedding occurs at a higher Reynolds number for the elastic splitter plate. As a result of the initial per-
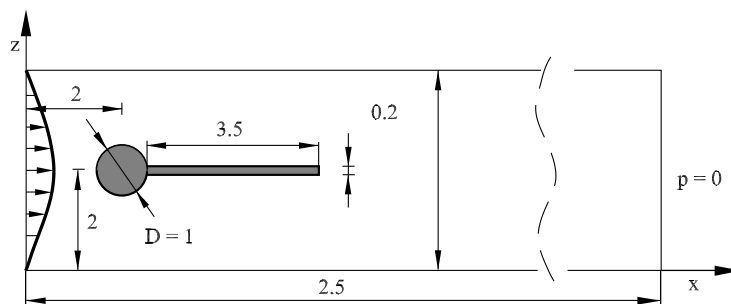

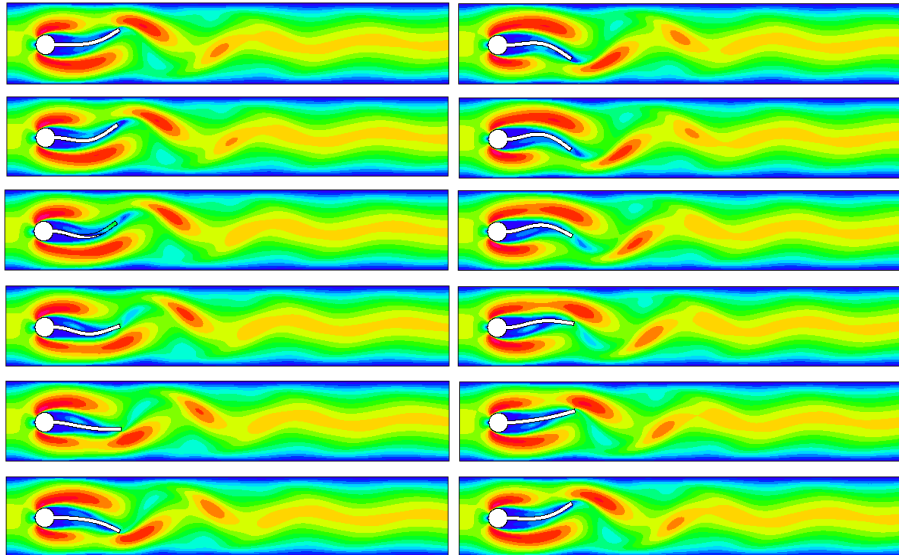Fig. 4.14. Geometry of the elastic splitter plate

73

Fig. 4.15. Velocity field and motion of the structure for one period of oscillation, $Re_D = 100$

turbation in the channel, a resonance of the eigen-oscillations of the structure with the periodically separation flow occurs. Figure 4.15 shows the velocity field for the absolutely unstable resonance oscillation for one oscillation cycle.

4.2.3 Car Aerodynamics

The prime example of the practical application of stability-theory concepts to control absolutely unstable wake flows is the flow past a vehicle. The boundary layer that separates at the rear of the car, after it passes the spoiler lip on the lid of the trunk, generates a part of the wake flow of the vehicle as a free shear layer (Fig 4.16). It forms a horseshoe vortex in which the edge vortex and the backflow on the lide of the trunk merge into one another. Superimposed onto this is a second backflow region, that is energized by the diffusor flow
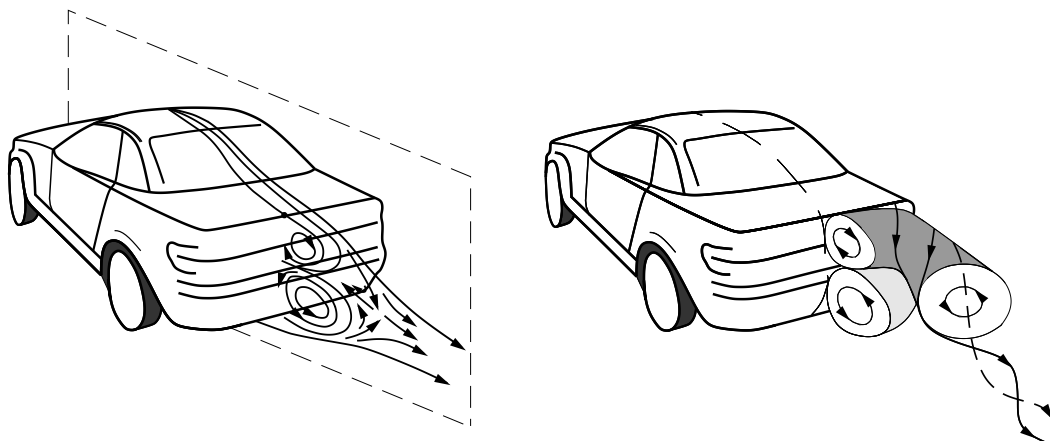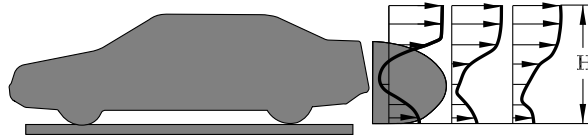

Fig. 4.16. Flow separation at the back of a car

Fig. 4.17. Wake flow of the car in a wind tunnel, $Re_L = 5 \cdot 10^6$

between the street and the vehicle. The shear layers as well as the global flow structure of the wake flow are periodically unstable, which can be seen as an oscillation of the horseshoe edge vortex downstream from the trunk. A typical method of flow control is suitable shaping of the back end of the car, to keep the absolutely unstable region of the wake flow as small as possible. This leads to tapering of the back end, where the pressure distribution is shaped so that a reduction of the absolutely unstable wake region is ensured. The calculation of the basic solution for the stability analysis of local perturbations in the wake has already been seen in Figure 3.7.

In addition to this, the time-averaged velocity profile in the mid section of the wake flow of the car model was measured in a wind tunnel. Figure 4.17 shows the wake flow at a Reynolds number of $Re_L = 5 \cdot 10^6$ with the shaded region the expected absolutely unstable region. Figure 4.18 shows the wind-tunnel model and the measured velocity profiles behind the car without and with flow control at the Reynolds number $Re_L = 1.33 \cdot 10^6$. The expert can see immediately that the measured boundary-layer flow on the floor of the wind tunnel does not correspond to the reality of a car driving on the street. However, the results of the perturbation calculation show that the eigenvalues
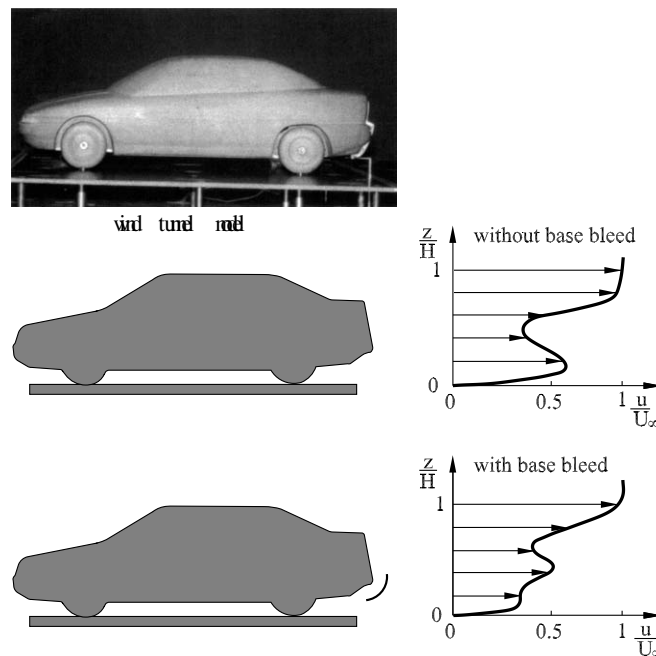

Fig. 4.18. Wind-tunnel measurement of the time-averaged wake flow of a car, $Re_L = 1.33 \cdot 10^6$

of the experimentally incorrectly simulated boundary-layer flow can be separated from the eigenvalues of the wake flow that is of interest. Therefore, in the perturbation calculation the incorrectly simulated boundary-layer profile can be separated from the measured basic profile $\bar{u}_i^0$.

Inactive flow control for a car is realized by means of a flow channel integrated into the fender. In the diffusor between the street and the vehicle, a few percent of the mass flux in the flow channel is deviated such that it reduces the shear layer behind the spoiler lip on the trunk and thus prevent the absolutely unstable region in the wake of the car. Initial measurements of the time-averaged velocity profile with base bleed shows that the flow control could not yet be optimized, but that a measured drag reduction of 10% was achieved through prevention of the absolutely unstable region in the mid section of the wake flow.

The result of the wave-packet perturbation analysis is summarized in Figure 4.19. The larges rate of amplification ω_i of the wave packets is plotted against the downstream coordinate x/H (H the height of the car) for the group velocity $g = 0$. Positive rates of amplification ω_i of the perturbation waves identify the absolutely unstable region behind the vehicle. Negative rates of amplification indicate the convectively unstable region. With base bleed the perturbation calculation yields a convectively unstable turbulent wake flow in the entire region with a measured drag reduction of 10%.

4.2.4 Vortex

Flow rate measurement of liquid, steam and gas is one of the most important areas of application for today's field instrumentation. Vortex meters are used
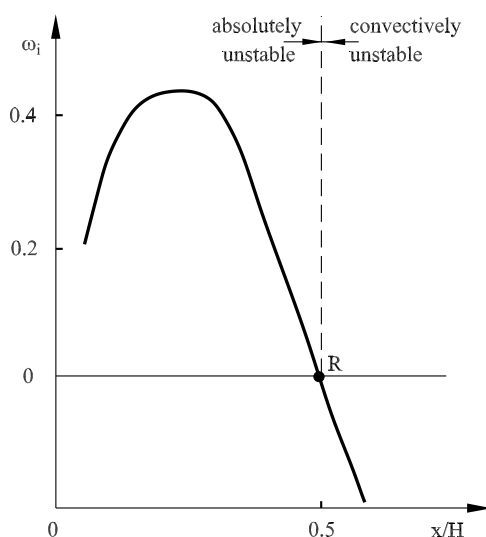

Fig. 4.19. Rate of amplification ω_i in the wake of a car

in numerous branches of industry to measure the volumetric flow by exploiting the unsteady vortex flow behind a blunt body. Among the wide variety of measurement principles, the vortex-shedding flow meter is well regarded to be reliable, robust and flexible. The range of application of the vortex-shedding device reaches from liquids through saturated steam to pure gases. The measurement principle of vortex flow meters is based on the formation of vortices shed from an obstacle spread over the span of a pipe.

Figure 4.20 shows the investigated CAD geometry corresponding to Figure 3.19 and a picture of the triangular vortex-shedding device in a pipe ($d/D = 0.23$, d diameter of the vortex-shedding device, D pipe diameter) as well as the results of numerical flow simulation of the turbulent flow. The upstream flow is a turbulent pipe flow. The flow structure reveals a horseshoe vortex at the connection of the shedding device with the wall. Downstream from the blunt body, the horseshoe vortex near the pipe wall interacts with a turbulent, three-dimensional shedding wake flow. The corresponding shedding frequency allows the flow rate to be determined. The relation between the Strouhal number Str and the Reynolds number Re_d is:

$$Str = a + \frac{b}{Re_d},$$
(4.5)

with constants a and b.

Most of the work on vortex shedding is related to the wake of a cylindrical body at velocities resulting in Reynolds numbers in the laminar range of $Re_d = 50 - 150$, as described in Section 4.2.4. In state-of-the-art industrial flow meters, rectangular or triangular shaped blunt bodies are employed,

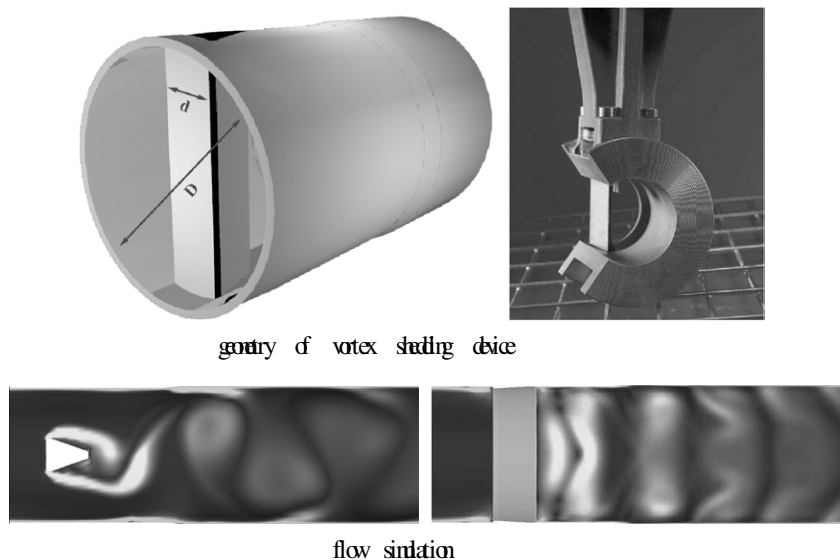geometry of vortex shedding device

flow simulation

Fig. 4.20. Vortex-shedding device and flow simulation in a pipe

operating at Reynolds numbers of $Re_d = 3000$ and beyond in the turbulent vortex-shedding region. In contrast to the majority of academic work on vortex shedding, the boundary conditions in industrial flow meters are significantly different. Von Kármán (and many of his successors) used long, thin rods in a flow with constant upstream velocity. In vortex flow meters, the turbulent flow is confined by the pipe wall which produces a flow with a significant velocity profile. At the junction between the blunt body and the pipe wall, a horseshoe vortex exists. Despite these difference, the formation of vortices is to some extent similar to that of a von Kármán vortex street. The most common similarity is the fact that the frequency of vortex shedding is directly proportional to the flow velocity. This behavior is employed in vortex flow meters. In the simplest case the vortex shedding frequency is counted and multiplied by a constant calibration factor yielding the volumetric flow rate

$$\dot{V} = K \cdot f.$$

This, however, implies that industrial flow meters are operated assuming a constant Strouhal number, indicated by a single calibration factor K associated with a flow meter.

$$
\begin{aligned}
u \cdot A &= K \cdot f, \\
\frac{u}{f \cdot d} \cdot A \cdot d &= K, \\
\frac{1}{Str} \cdot A \cdot d &= K,
\end{aligned}
\tag{4.6}
$$

with the pipe area A.

In fact, the Strouhal number is found to be a function of the Reynolds number, as shown in Figure 4.21. To estimate the Strouhal-Reynolds-number dependence for the triangular vortex-shedding device of Figure 4.20, experiments as
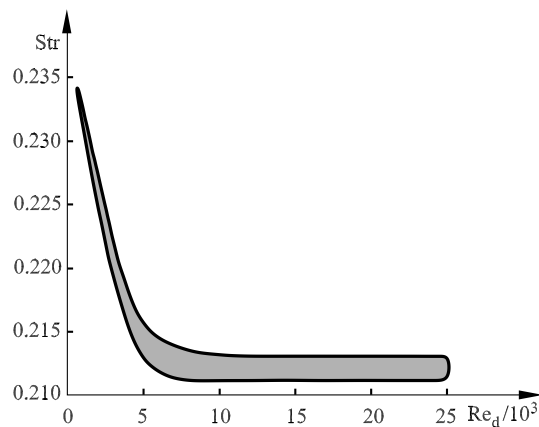

Fig. 4.21. Strouhal-Reynolds-number dependence of vortex shedding

well as numerical simulations have been performed. The decay of the Strouhal number with increasing Reynolds number is theoretically confirmed by the stability analysis of local perturbations.

A vortex flow meter as commercial available was investigated to produce experimental data directly comparable with numerical simulations. For the tests a flow meter of nominal diameter DN150 was used. Figure 4.22 shows the geometry of the experimental and numerical set up, with the triangular vortex-shedding device and the paddle for measuring the shedding frequency.

The vortex-sensing element is a paddle-shaped device mounted in an opening of the blunt body close the the pipe wall. It senses the pressure fluctuations at the trailing edge of the blunt body caused by the alternating flow separation. The paddle is held by a membrane sealing the pipe. At the opposite side (outside the flow) a cylinder is attached to the membrane. The cylinder performs the same movement as the paddle as it is moved by the pressure fluctuations. The cylinder is embedded in two semicircular shells but separated by a small gap, forming a capacitor. A charge amplifier amplifies the charge of the capacity.

To validate the numerical model for the calculation of the stability analysis of the time-averaged basic flow $\bar{U}_i^0$, the results of numerical simulation were compared with the results of measurements. For this purpose an experimental rig was build. The validation measurements were performed for a geometrically similar ($d/D = 0.27$) but smaller flow meter owing to restrictions in laboratory space. The experiment fluid was air at ambient pressure and temperature. The measurements were done in a Reynolds number range of $1 \cdot 10^4 < Re_d < 2.8 \cdot 10^4$. The necessary pressure was provided by a radial flow pump. The mass flow through the pipe was measured using an impeller flow meter. The shedding frequency was evaluated from the raw data of the vortex-shedding flow meter.
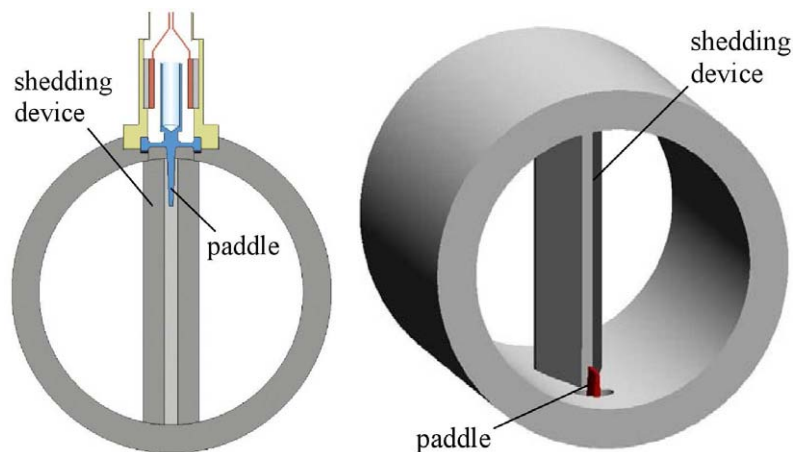

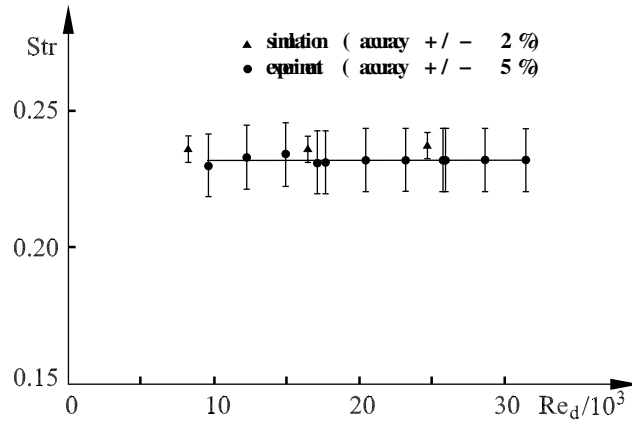Fig. 4.22. Geometry of experimental set up

79

Fig. 4.23. Results of the validation

Figure 4.23 shows the comparison between the measured and the simulated Strouhal number over the Reynolds number. There is very good agreement in the perfectly linear *Str-Re* relation over the measurement range with a slight offset, which is within the experimental uncertainty.

The numerical simulations reveal a complex flow structure around and behind the blunt body (see Figure 4.24). At the junction of the blunt body with the pipe wall, a horseshoe vortex can be detected. The size of it depends on the Reynolds number. In the center plane of the blunt body, periodic vortex shedding similar to the structure of the von Kármán vortex street occurs. Towards the upper and lower pipe walls the influence of the horseshoe vortex and the smaller distance to the side wall change the flow characteristics and create a complex periodic three-dimensional vortex-shedding structure. Figure
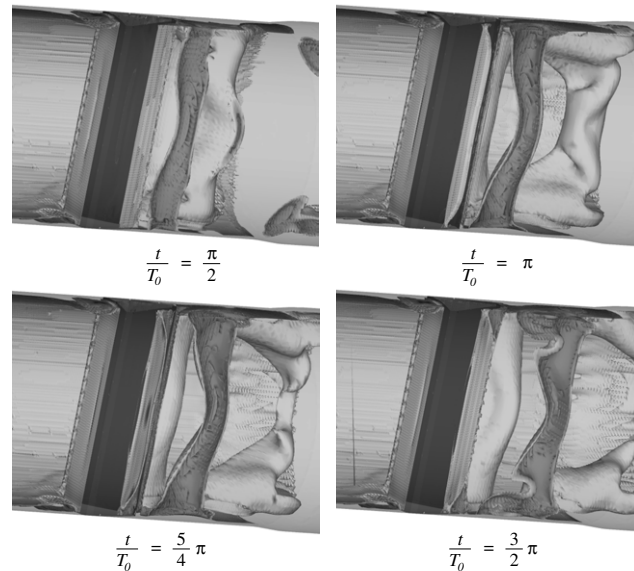

$$\frac{t}{T_0} = \frac{\pi}{2}$$

$$\frac{t}{T_0} = \pi$$

$$\frac{t}{T_0} = \frac{5}{4}\pi$$

$$\frac{t}{T_0} = \frac{3}{2}\pi$$

Fig. 4.24. Three-dimensional flow in the vortex-shedding device at 4 time steps of one period T_0

80

4.24 shows the periodic three-dimensional flow structure by visualization of the isovolume of the vorticity.

In contrast to Figure 4.10 showing the von Kármán vortex street, in which $1/Str$ is plotted, the results of the numerical simulation show an increase of the Strouhal number with decreasing Reynolds number, starting at a Reynolds number of $Re_d = 4800$. Figure 4.25 shows the Strouhal-Reynolds number dependence determined by the numerical flow simulation in comparison with the results of the stability analysis. Additionally the experimental results are displayed in the same illustration.

Figure 4.25 shows an increase of the Strouhal number for small Reynolds numbers in the simulations. The same tendency can be observed in the experimental data. The absolute discrepancy arises from the tolerances in the geometry of the blunt body in the experimental set up.

The increase of the Strouhal number for small Reynolds numbers is also confirmed by the results of the stability analysis. Differences in the absolute values of the Strouhal numbers for higher Reynolds numbers are due to the constraints of the stability analysis of local perturbations with regard to the assumed parallel flow condition of the classical Orr-Sommerfeld stability analysis of Section 3.2. In order to reconcile the absolute values of the Strouhal number with the values from experiment and simulation, a stability theory calculation with the commercial software packet COMSOL is necessary.
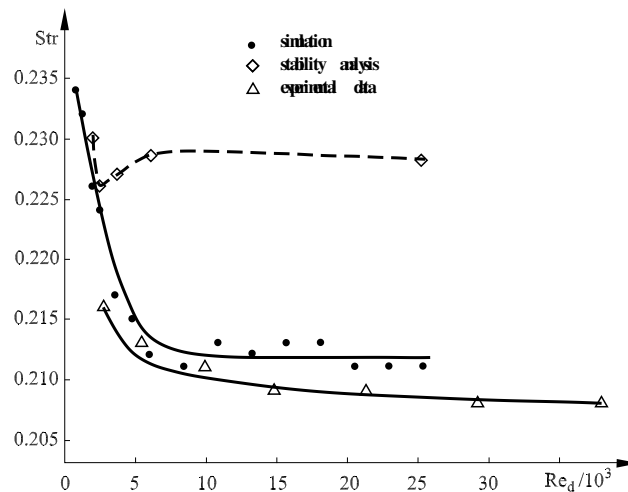
Fig. 4.25. Comparison between the Strouhal numbers determined by the numerical flow simulation and by the stability analysis

81

4.3   Resonator

Fluid-mechanical resonators are basically absolutely unstable because of the feedback. This is the case for an aeroacoustic resonator between two diaphragms in a pipe flow and a fluidic oscillator applied as a fan nozzle for cleaning the windshields of cars.

4.3.1   Double-Diaphragm Resonator

The double-diaphragm resonator in a pipe flow (Figure 3.20) has already been used in Section 3.3 to verify the software for the flow calculation and to localize the source of acoustic noise in the resonator. The reduction of aeroacoustic noise emission plays a major role in modern product development processes. In particular, aviation tasks are focused on the difficulty of aeroacoustic propagation owing to an increasing demand for passenger comfort and protection of the environment. Reynolds-averaged Navier-Stokes (RANS) approaches, as decribed in Section 3.1, were developed in order to determine source term distributions on the basis of K-ϵ turbulence models and synthetic energy spectra. However, in order to describe the real sound propagation, a direct resolution of fluctuation terms must be taken into account. Since the acoustic field is determined by the large turbulent scales, detached eddy simulations (DES) can be applied for aeroacoustic investigations.

In accordance with the publication of *S. Höttges et al.* 2010, on the basis of the classical wave equation with source terms, three source mechanisms for sound can be distinguished:

Monopole: fluctuation of pressure due to pulsating mass flux
Dipole: fluctuation of pressure due to change of forces over time
Quadrupole: fluctuation of pressure due to turbulence

Based on Lilley's modifications of source terms, terms describing the interaction of flow and sound-field convection and refraction are moved beside the wave operator. Therefore the right-hand side of equation (4.7) contains no terms with contribution to propagation but only source terms formulated for shear-layer dominant flow

$$\frac{\mathrm{d}}{\mathrm{d}t}\left[\frac{\mathrm{d}^2\Pi}{\mathrm{d}t^2} - \frac{\partial}{\partial x_i}\left(a^2\frac{\partial\Pi}{\partial x_j}\right)\right] + 2\frac{\partial u_j}{\partial x_i}\frac{\partial}{\partial x_j}\left(a^2\frac{\partial\Pi}{\partial x_j}\right) = -2\underbrace{\frac{\partial u_j}{\partial x_i}\frac{\partial u_k}{\partial x_j}\frac{\partial u_i}{\partial x_k}}_{A} + \Psi, \quad (4.7)$$

where

$$\Psi = \underbrace{2\frac{\partial u_j}{\partial x_i}\frac{\partial}{\partial x_j}\left(\frac{1}{\rho}\frac{\partial \tau_{ik}}{\partial x_k}\right) - \frac{\mathrm{d}}{\mathrm{d}t}\left[\frac{\partial}{\partial x_i}\left(\frac{1}{\rho}\frac{\partial \tau_{ik}}{\partial x_k}\right)\right]}_{B} + \underbrace{\frac{1}{c_p}\frac{\mathrm{d}^3 S}{\mathrm{d}t^3}}_{C},\tag{4.8}$$

$$\Pi = \frac{1}{\kappa}\cdot\ln\left(\frac{p}{p_{\text{ref}}}\right).\tag{4.9}$$

and

  A: effects of fluctuation and shear layer
  B: effects of fluid viscosity
  C: effects of entropy fluctuations

For flows with high Reynolds numbers, the effect of fluid viscosity can be neglected. The fluctuation of entropy can also be neglected as long as neither heat transfer nor combustion are taken into account. The remaining source term A can be further divided using a linear perturbation approach for u_i that is similar to Reynolds decomposition.

Assuming quasi-steady flow of an incompressible fluid, the source term A is further simplified:

$$A = -2\frac{\partial u_j'}{\partial x_i}\frac{\partial u_k'}{\partial x_j}\frac{\partial u_i'}{\partial x_k}.\tag{4.10}$$

The velocity fluctuations are obtained from the turbulent flow simulation using a synthetic turbulence method.

The investigation of mean properties of the turbulent flow and the derived fluctuating components already provides an insight into the source regions for shear-layer dominant noise. For an accurate prediction of noise in the double-diaphragm resonator, however, an investigation of unsteady flow properties is mandatory. In order to obtain accurate noice prediction, the detached eddy simulation (DES) method was chosen. This approach is reasonable since the acoustic behavior is dominated by large-scale turbulence which is directly resolved.

Basically all eddy-viscosity models can be adapted for DES use. In this work a modified K-ϵ model is utilized. Here the dissipative source term $D = \rho\epsilon$ is replaced by an expression containing a characteristic length $\tilde{l}$:

$$D = \rho\cdot\frac{k^{3/2}}{\tilde{l}}.\tag{4.11}$$

The turbulence model used acts either as the original RANS model or as a DES sub-gridscale model, depending on the distance from the wall and the

grid size. Hence in all areas the best method regarding accuracy and simulation effort is used

$$\tilde{l} = \min\left(\frac{k^{3/2}}{\epsilon}, C_{\mathrm{DES}} \cdot \Delta\right), \tag{4.12}$$

where $\Delta \equiv \max(\Delta x, \Delta y, \Delta z)$.

Validation of the aeroacoustic model is carried out using the experimental set up shown in Figure 4.26. Air enters the domain from the left-hand side with $U = 5m/s$ and passes the double diaphragm device. Pressure fluctuations are measured and detected numerically a distance $1D$ upstream (1) and $1D$ downstream (3) from the restrictors of the pipe, as well as in the cavity in between (2). The distance between the two diaphragms is $1D$. Figure 4.27 shows experimental and calculated frequency spectra for microphone position 2 only in order to reduce the amount of information given. Microphone positions 1 and 3 behave accordingly, so the major simulation outcomes can be concentrated on microphone position 2 which is, as expected, the most interesting location owing to diaphragm resonator effects. The spectra show the dominant resonator frequency at $f = 550Hz$ both in experiment and with the aeroacoustic model of the unsteady simulation calculation.

At $f = 320Hz$ a further low frequency resonance frequency occurs. The high-frequency oscillations are replaced by the shear layers caused by the diaphragms, where the tonal component of the diaphragm resonator dominates. In addition to the spectra, Figure 4.28 shows the steady field of the aeroacoustic sources whose time-averaged velocity profile $\bar{U}_i^0$ is used for the stability analysis of local perturbations, as well as snapshots of the unsteady distributions of the velocity magnitude, dissipation rate and turbulent kinetic energy in the mid section of the double-diaphragm resonator.

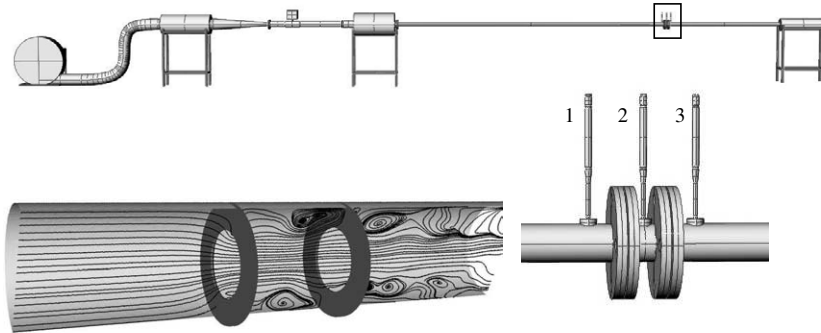With the experimental and numerically validated spectra of Figure 4.27, in

Fig. 4.26. Experimental set up and flow simulation of the double-diaphragm resonator

addition to the stability analysis, this aeroacoustic development tool can be used to control the tonal and shear-layer frequencies through suitable geometrical shaping of resonators, so that such frequencies are no longer irritating for the human ear. The air conditioning of the cockpit and the cabin of the new generation of Airbus airplanes were designed using the methods described here.

4.3.2 Fluidic Oscillator

The fluidic oscillator combines the absolutely unstable fluid-mechanical resonator with circuit technology in order to realise analogue and digital switching for measuring and control tasks. The area of application extends from measuring technology to medical technology, to switching mechanisms for aerospace engineering. With the rapid development and increasing miniaturization of electronic components, however, it is electronics that has become established. While logic switches made of several fluidic components have been almost completely superseded because of their high energy requirements, individual fluidic components are widely applied until today.

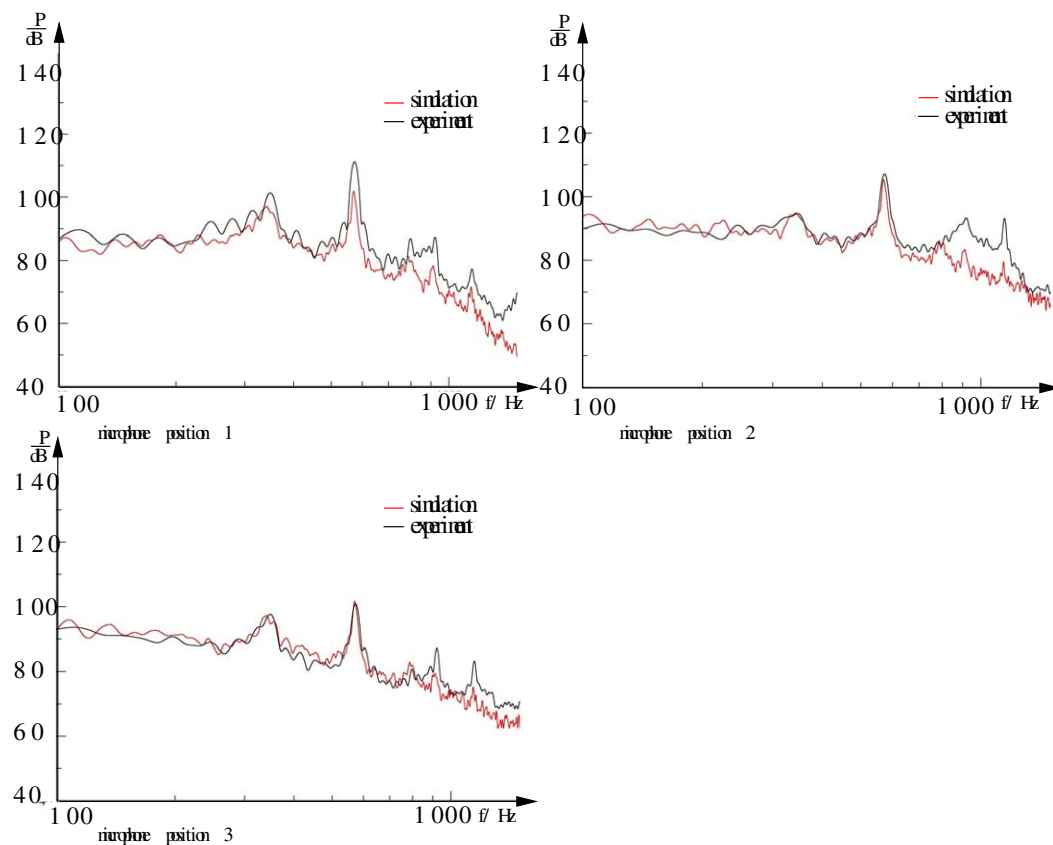As fluidic components can do without moving parts they are very robust

Fig. 4.27. Power spectral density distributions

85

and reliable. They can be used in regimes in which electronic components reach their limits of application. Fluidic components can be applied in extreme environmental conditions, such as at high temperatures, in electromagnetic radiation, strong magnetic fields, radioactivity, aggressive media and at high accelerations. A further classical area of application is in measuring technology, for example for measuring flow rates or temperatures.

In recent years interest has been renewed in fluidic components. Possibilities for application of fluidic oscillators have been tested in flow control, to reduce or avoid separation regions, to avoid resonance noise in the flow past cavities, to improve combustion processes or for efficient cooling of turbine blades or electronic components.

The main area of application of fluidic components at present is in the car industry as nozzles for cleaning windshields. A fluidic oscillator used as a fan nozzle is currently used in most cars. In such fan nozzles, a flat distribution of water is sprayed onto the windshield with an automatically oscillating point jet. The motion of the jet is achieved only by suitable shaping of the nozzle geometry and of the fluid-mechanical resonator, so that no moving components or external sources of energy are necessary. In comparison to standard nozzles, the advantage here is the considerably lower requirement for cleaning agents combined with a considerably large wetting area on the front windshield, as
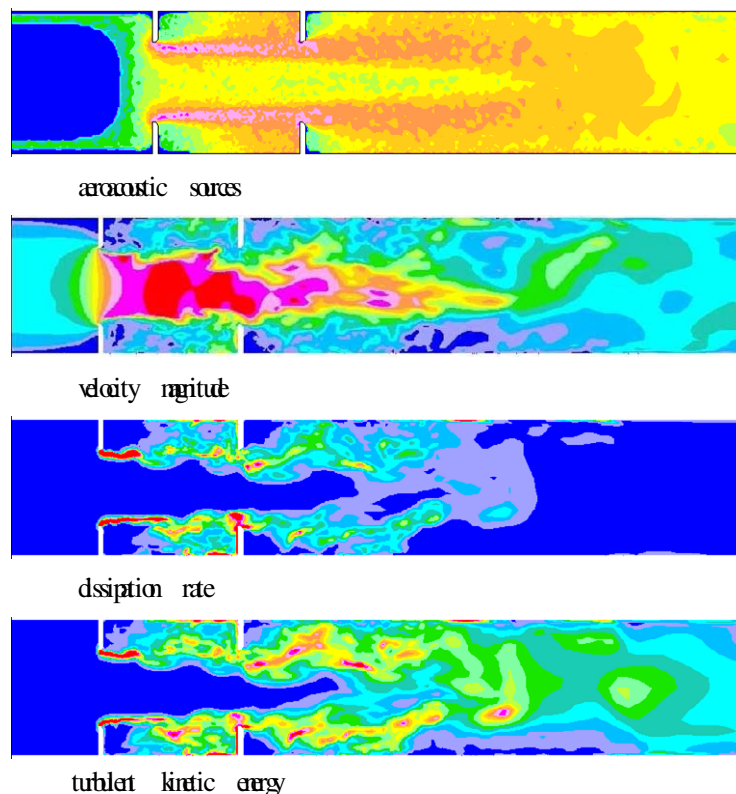

Fig. 4.28. Flow simulation of the double-diaphragm resonator

well as higher stability of the jet against head-wind effects. If the Reynolds number in the fan nozzle falls below a critical Reynolds number at low external temperatures, the oscillation of the jet is disrupted and the cleaning agent leaves the nozzle as a compact point jet. Particularly in winter at low temperatures, and thus higher viscosity of the cleaning agent, this leads to insufficient cleaning efficiency on the windshield.

In this case stability theory with determination of the critical Reynolds number can help to shape the feedback of the fan resonator so that it remains functional even at low temperatures.

Figure 4.29 shows the geometrical arrangement of the fan nozzle with the resonator volume and the fluidic feedback (*S. Höttges* 2010). The feed line of the cleaning agent into the fan nozzle is from below through a circular opening. After a right-angled deviation this connects to convergent intake region, which terminates with a narrow cross-section. The adjacent resonator chamber consists of a continuously divergent region, a region with constant chamber width and a second divergent region. On both sides of the front face of the main chamber are beam splitters. These divert a part of the oscillating jet and lead it back through the feedback. Via the control input, the fed back medium is added to the main jet perpendicular to the direction of flow. Most of the cleaning agent departs the main chamber via the outlet opening. The applicability at low temperatures is achieved by the linearly increasing depth of the resonator chamber donwstream from the crosspoint. It is shaped so that even at relatively high viscosities the oscillation of the jet is ensured.

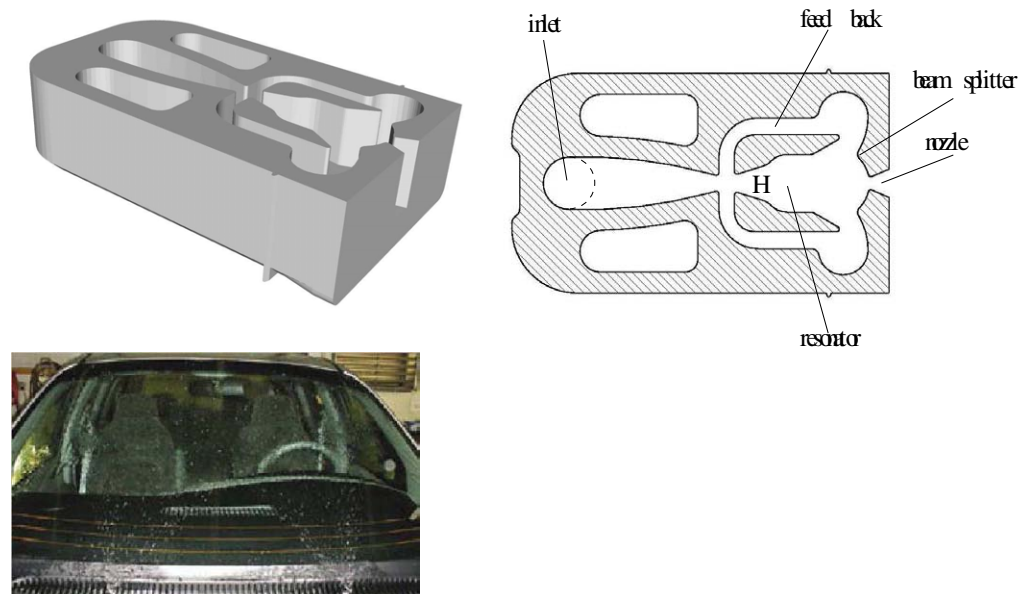Calculation of the oscillating flow was carried out using the commercial soft-

Fig. 4.29. Geometry of the fan nozzle

ware described in Section 3.1. The result of the simulation calculation is shown in Figure 4.30 for one cycle of oscillation. At each point in time the projection of the three-dimensional streamlines in longitudinal section of the resonator
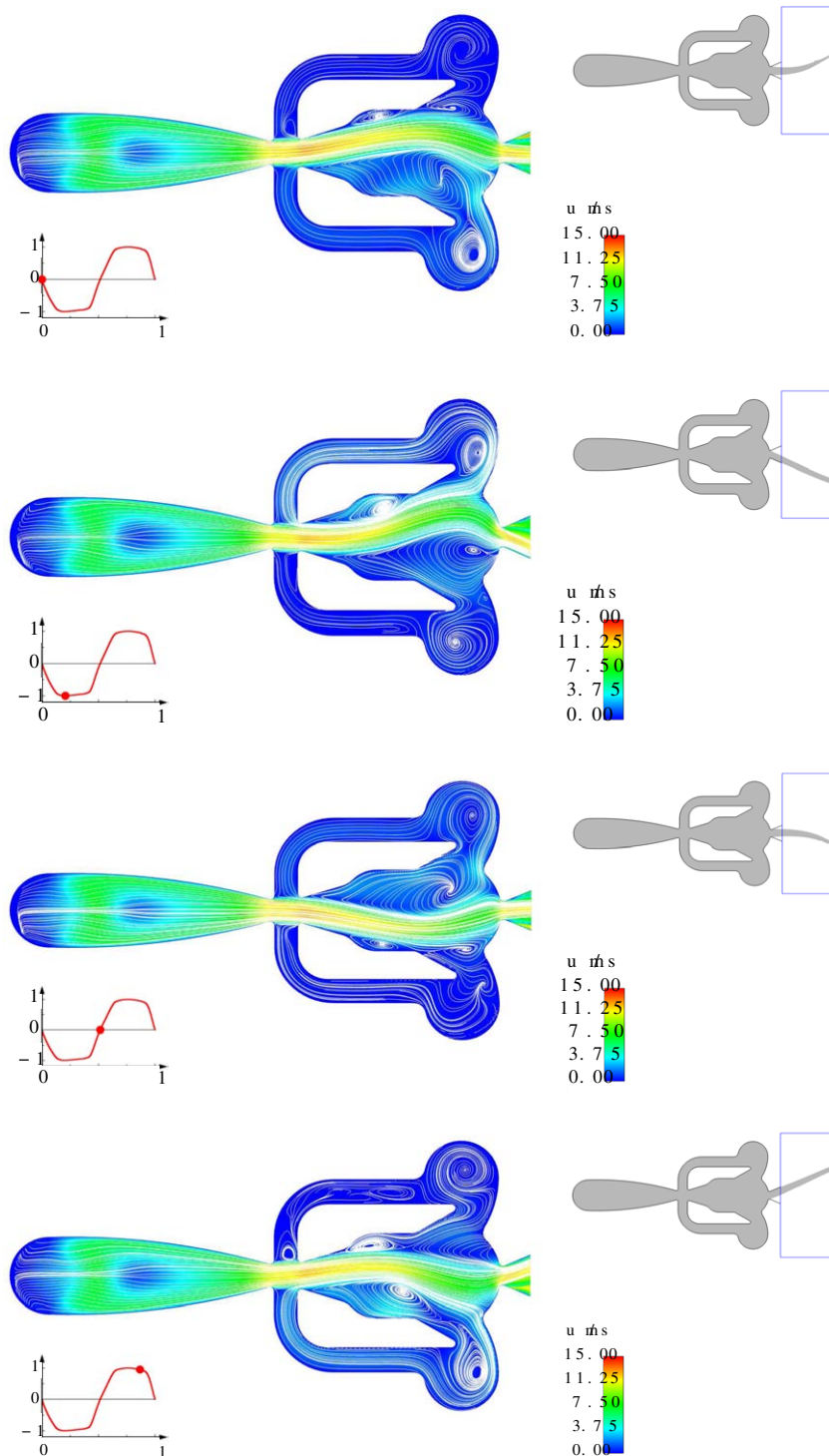

Fig. 4.30. Flow simulation

88

and the nozzle is shown, where the magnitude of the velocity is color coded. In addition, at each point in time the same section through jet of cleaning agent is shown in the nozzle outlet and in the adjoining exit volume as iso-surfaces of constant water-ethanol concentration.

At the first point in time, the lower vortex in the resonator is dominant and the main jet is deviated upwards. At the exit from the nozzle the jet has a vanishing velocity in the z-direction. Because of its inertia, the main jet is curved in the exit volume. Later the lower vortex moves further to the right to the front limits of the main chamber and increases further in size. This causes the main jet in the main chamber to be deviated further upwards. Following this a part of the main jet is diverted by a beam splitter placed at the front face of the main chamber and fed back via the upper feedback line. At the interface between the main chamber and the feedback line a vortex is induced which, however, does not contribute to the functionality of the nozzle and can be avoided by suitable shaping of the geometry in this area. The volume flux via the upper feedback line increases with increasing deviation of the main jet and, in the second picture, it reaches its maximum. As a consequence of this the upper separation region grows because of the continuous inflow. The jet outside the nozzle is now in its lower end position. As the backflow is maintained, the upper vortex in the main chamber increases further and moves to the right in the main chamber, while the lower vortex is increasingly dissipated. Through the growth of the upper vortex the jet in the main chamber is now deviated further downwards. Because of the curvature of the jet, and through the overflow of the side bulge, a small vortex arises already at the start of the main chamber. Outside the nozzle the jet is still in its lower end position.

In the third picture the jet in the main chamber is curved so far downwards, because of the growing upper vortex, that the jet now departs its lower end position outside the fan nozzle. Then the upper vortex grows further and moves in the direction of the front face of the main chamber. The main jet in the main chamber is deviated so far downwards that a part of the main jet is diverted by the beam splitter and the backflow starts via the lower feedback line. The volume flux through the feedback fline then increases, causing the lower vortex to increase and the main jet in the lower part of the main chamber is already deviated upwards. In the fourth picture the jet outside the fan nozzle reaches its upper end position. As the flow in the lower feedback line is maintained, the lower vortex increases further and moves to the right in the main chamber. With increasing size of the lower vortex, the jet in the main chamber is deviated further upwards. The vortex that will later cause the deviation on the opposite side now forms on the upper side in the region of the side bulge of the main chamber. The lower vortex has grown so much that the jet outside the nozzle leaves its upper end position and moves downwards, so that the cycle of oscillation can begin again.
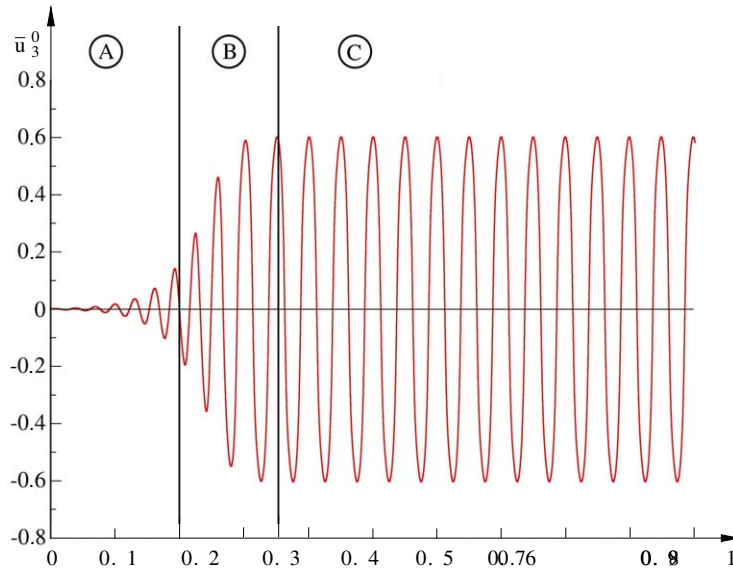
Fig. 4.31. Time dependence of the velocity, $Re_H = 252$

With the time-averaged velocity profile, the stability analysis to determine the critical Reynolds number is carried out using the commerical software COMSOL. Figure 4.31 shows the calculated basic solution U_3^0 of the oscillator at the Reynolds number $Re_H = 252$ formed with the height of the intake (see Figure 4.29). Small disturbances grow exponentially starting from the quasi-steady or time-averaged basic state. The region of constant exponential
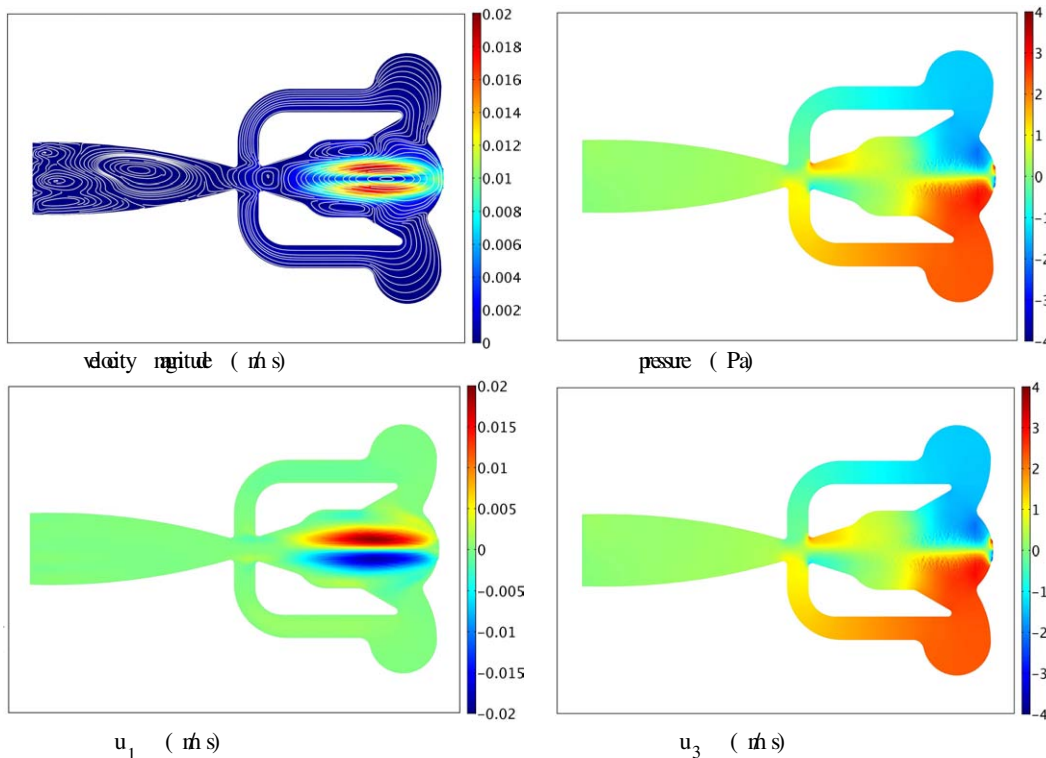

Fig. 4.32. Eigenfunctions of the eigenvalue with the smallest real part

90

amplification is called the linear growth region.

In the transition region B the exponential growth of the perturbations is nonlinearly bounded. These gain importance with increasing amplitude and eventually lead to the formation of self-perpetuating oscillation of constant maximum amplitude in the fan nozzle in the nonlinear saturation state. The periodic solution of the underlying nonlinear system of equations is also called a limit cycle. The amplitude of the limit cycle in the fan nozzle increases with increasing Reynolds number.

Figure 4.32 shows the eigenfunctions of the stability analysis and the smallest real part. The eigenfunctions and the eigenvalues are both complex, and only shown for one particular phase. As the real part is negative, small perturbations are amplified in time. The basic flow is therefore unstable at $Re_H = 252$.

To determine the critical Reynolds number of the oscillator, the eigenvalues and eigenfunctions are determined at different intake pressures of the fan nozzle. The form of the eigenfunction of the eigenvalue with the smallest real part does not change. Only the amplitude of the eigenfunction deviates from the values shown in Figure 4.32 with variation in the pressure and therefore in the Reynolds number.

The distribution of the resulting eigenvalues for various Reynolds numbers is shown in Figure 4.33 in the complex plane. The eigenvalues are symmetric with respect to the x axis and therefore form a complex conjugate pair. It can also be seen that for increasing Reynolds number the eigenvalues with the smallest real part are shifted to the left. This means that the solutions become ever more unstable with increasing Reynolds number. The perturbations superimposed on the basic state decay as long as the real part of the eigenvalue is positive.
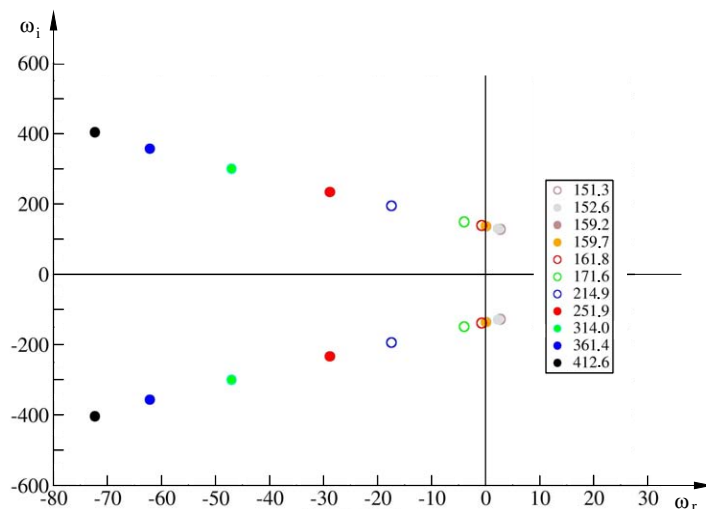

Fig. 4.33. Change in eigenvalue with variation of the Reynolds number

The basic state is therefore stable.

The change in sign in the real part of the eigenvalue is characteristic of the transition from the stable to the unstable state. The root of the real part and thus the rate of amplification can be determined from the results of the stability analysis. In accordance with Figure 4.33 the change in sign of the real part of the eigenvalue lies at the critical Reynolds number $Re_{\text{crit}} = 159.6$.

Figure 4.34 shows a comparison of the frequencies of the fan nozzle determined with the stability analysis and flow simulation in the basic state for different intake velociies U_H in the resonator. Very good agreement is found for the results of the stability analysis both for the quasi-steady flow as well as for the time-averaged basic flow, where the maximum frequency in the linear growth region determined from the unsteady flow simulations can easily be seen. The change in the frequency also agrees with a validation experiment carried out.

The linear change in the frequency corresponds to the constant Strouhal number of Figure 4.23 of the wake flow of a vortex damming body as well as the perturbation cylinder experiment of Sections 1.1 and 3.4. This confirms the statement made at the start of this chapter that the stability theory concept of absolute instability can also be used for flow control and to design fluid-mechanical resonators.
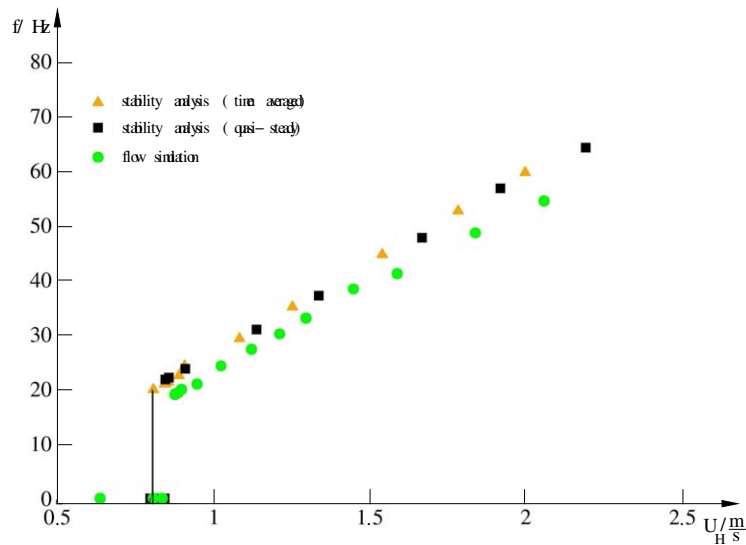

Fig. 4.34. Comparison of frequencies

92

5 Conclusions

Based on the Prandtl memorial lecture *H. Oertel* 1994, the stability-theory concept of absolute instability was developed into efficient flow control for laminar and turbulent flows. Through the stability theory of local perturbations the flow regions can be determined in which temporally and spatially amplified perturbations propagate, and this provides the opportunity of controlling the flow in these convectively or absolutely unstable regions through suitable shaping, surface properties, perturbation bodies, suction or blowing. In addition to calculation of the flow and experiments in test facilities, a stability-theory development tool for flow control based on commercial fluid-mechanical software is also available. The mathematical methods of Laplace transform and Fourier transform of wave packets that it uses were developed long ago, but for their first time their application to perturbation differential equations of laminar and turbulent flows has led to a classification of viscous flows that enables efficient flow control.

With the examples of the von Kármán vortex street in the wake of a cylinder of a stagnation body in a pipe flow for measuring the volume flux, the flow past a car, and the laminar–turbulent transition in the three-dimensional transonic boundary layer of a wing, we have demonstrated how the drag may be reduced by eliminating the absolutely unstable regions in the flow field. Based on the wave-packet perturbation calculation, a design criterion for transonic laminar wings was presented. This restricts the angle of sweep of the transonic wing and is based on avoiding the onset of the convectively unstable cross-flow waves in the three-dimensional boundary layer on the wing. The stability-theory analysis of fluid-mechanical resonators extends the range of application to aeroacoustic design of air conditioning sytems of cars and airplanes. The tonal frequencies of the systems of piping can be controlled through suitable selection of the geometry to enable low noise air conditioning systems.

The theoretical basis of the stability theory of local perturbations was developed already in the 1990s. However, its application to practical three-dimensional turbulent flows became possible only in the last 15 years through the availability of commercial fluid-mechanical software.

References

B. Baccani, F. Domenichini, G. Pedrizzetti. Model and Influence of Mitral Valve Opening during the Left Ventricular Filling. J. Biomech., 36, 335-361, 2003.

A. Bers. Theory of Absolute and Convective Instabilities. Int. Congress on Waves and Instabilities, B1-B52, Innsbruck, Austria, 1973.

R.J. Briggs. Electron-stream Interactions in Plasmas. MIT Press, 1964.

F.N.M. Brown. A Combined Visual and Hot-Wire Anemometer Investigation of Boundary-Layer Transition. AIAA, 6, 1, 29-36, 1957.

S. Chandrasekhar. Hydrodynamics and Hydromagnetic Stability. Clarendon Press, Oxford, 1961.

J. Delfs, J. Ehrhard, E. Meiburg, H. Oertel. Lagrange Identification of Absolutely Unstable Regimes in Wakes. ACTAMECHANICA, 122, 89-97, 1997.

J. Delfs, H. Oertel. Dynamics of Localized Disturbances in Engineering Flows. J. Fluid Mech., 347, 369-374, 1997.

P. G. Drazin, W. H. Reid. Hydrodynamic Stability. Cambridge University Press, 1981.

M. Gaster. A Note on the Relation Between Temporally-Increasing and Spatially-Increasing Disturbances in Hydrodynamic Stability. J. Fluid Mech., 14, 222–224, 1962.

K. Hannemann, H. Oertel. Numerical Simulation of the Absolutely and Convectively Unstable Wake. J. Fluid Mech., 199, 55-88, 1989.

W. Heisenberg. Über Stabilität und Turbulenz von Flüssigkeitsströmen. Annalen der Physik, 74 of 4, 577–627. Barth, Leipzig, 1924.

S. Höttges, A. Class, H. Oertel. Hydrodynamic Stability Analysis of Fluidic Oscillator Flow. Int. J. Flow Control, in preparation.

S. Höttges, S. Krittian, T. Schenkel, K. Debatin, H. Oertel. Aeroacoustic Analysis of Pipe Flow Restricted by Orifice Plates using DES. AIAA, in preparation.

Th. von Kármán. Über den Mechanismus des Widerstandes, den ein bewegter Körper in einer Flüssigkeit erfährt. Nachrichten von der Königlichen Gesellschaft der Wissenschaften zu Göttingen, 547-556 (1912).

W. Koch. Local Instability Characteristics and Frequency Determination of Self-Excited Wake Flows. J. Sound Vib., 99, 53-83.

Y. Kohama. Some Expectations on the Mechanism of Cross-Flow Instability in a Swept Wing Flow. Acta Mechanica, 66, 21-38, 1987.

E. Laurien, H. Oertel. Numerische Strömungsmechanik, 3rd edition. Vieweg + Teubner, Wiesbaden, 2009.

C. C. Lin. The Theory of Hydrodynamic Stability, 5. Cambridge University Press, Cambridge, 1955.

H. Oertel. Wakes behind Blunt Bodies. Ann. Rev. Fluid Mech., 22, 539-564, 1990.

H. Oertel. Bereiche der reibungsbehafteten Strömung. 37. Ludwig Prandtl Gedächtnisvorlesung, GAMM Tagung, TU Braunschweig, 1994.

H. Oertel. Bereiche der reibungsbehafteten Strömung. Z. Flugwiss. Weltraum-
forschung, 19, 119-128, 1995.

H. Oertel. Strömungsmechanik. Springer, Berlin, Heidelberg, New York, 1995.
Universitätsverlag Karlsruhe, 2005.

H. Oertel, J. Delfs. Mathematische Analyse der Bereiche reibungsbehafteter
Strömungen. Z. angew. Math. Mech, 75, 7, 491-5-5, 1995.

H. Oertel. Turbulenzentstehung in kompressiblen Grenzschichtströmungen.
Sonderdruck Braunschweigische Wissenschaftliche Gesellschaft, Jahrbuch
1995, 131-141, 1996.

H. Oertel. Strömungsmechanik Software KAPPA für Ausbildung, Forschung
und Industrieprojekte. Bericht 96/2, Institut für Strömungslehre, Univer-
sität Karlsruhe, 1996.

H. Oertel, J. Delfs. Strömungsmechanische Instabilitäten. Springer, Berlin,
Heidelberg, New York, 1996. Universitätsverlag Karlsruhe, 2005.

H. Oertel, R. Stank. Dynamics of Localized Perturbations in Transonic Wing
Boundary Layers. AIAA, 99-0551, 1-11, 1999.

H. Oertel. Onset of Turbulence (Stability Theory). Schlichting H., Gersten K.,
Boundary-layer Theory, 415-494, Springer, Berlin, Heidelberg, New York,
2003.

H. Oertel. Einsetzen der Turbulenz (Stabilitätstheorie). Schlichting H., Ger-
sten K., Grenzschichttheorie, 445-531, Springer, Berlin, Heidelberg, New
York, 2006.

H. Oertel Bioströmungsmechanik. Vieweg + Taubner, Wiesbaden, 2008.

H. Oertel ed. Prandtl - Führer durch die Strömungslehre, 12th edition.
Springer, Berlin, Heidelberg, New York, 2008.

H. Oertel ed. Prandtl - Essentials of Fluid Mechanics, 3rd edition. Springer,
Berlin, Heidelberg, New York, 2009.

H. Oertel, M. Böhle, U. Dohrmann. Strömungsmechanik, 5th edition. Vieweg
+ Teubner, Wiesbaden, 2009.

W. M. F. Orr. The Stability or Instability of the Steady Motions of a Perfect
Liquid and a Viscous Liquid. Proc. R. Ir. Acad., A 27, 69–138, 1907.

L. Prandtl. Über Flüssigkeitsbewegung bei sehr kleiner Reibung. Verhandlg.
III. Intern. Math. Kong. Heidelberg, 574-584, Teubner, Leipzig, 1905.

J. W. S. Rayleigh. On Convection Currents in a Horizontal Layer of Fluid,
when the Higher Temperature is on the Under Side. Philos. Mag. Ser, 32,
6, 529–546, 1916.

*M. Reik., R. Höcker, C. Bruzzese, M. Hollnach, O. Koudal, T. Schenkel,
H. Oertel.* Flow Rate Measurement in a Pipe Flow by Vortex Shedding.
Forschung im Ingenieurwesen, 74,2, 77-86, 2010.

O. Reynolds. An Experimental Investigation of the Circumstances which De-
termine whether the Motion of Water shall be Direct or Sinuous, and of the
Law of Resistance in Parallel Channels. Philosophical Transactions of the
Royal Society of London, 174, 935–982. Royal Society, London, 1883.

O. Reynolds. On the Dynamic Theory of Incompressible Viscous Fluids and
the Determination of the Criterion. Philosophical Transactions of the Royal

Society of London, 186, 123–164. Royal Society, London, 1894.

H. Schlichting. Grenzschichttheorie. Braun, Karlsruhe, 1951.

H. Schlichting, K. Gersten. Boundary-Layer Theory, 8th edition. Springer, Berlin, Heidelberg, New York, 2003.

H. Schlichting, K. Gersten. Grenzschichttheorie, 10th edition. Springer, Berlin, Heidelberg, New York, 2006.

A. Sommerfeld. Ein Beitrag zur hydrodynamischen Erklärung der turbulenten Flüssigkeitsbewegung. G. Castelnuovo, ed., Atti del IV Congresso internazionale dei matematici, 116–124, Roma, 1908.

C. G. Speziale. Analytical Methods for the Development of Reynolds Stress Closures in Turbulence. Ann. Rev. Fluid Mech., 23, 107–157, 1991.

M.J. Stoynov, H. Oertel. Linear and Nonlinear Dynamics of Localized Disturbances in Three-Dimensional Boundary Layers. Z. angew. Math. Mech., 82, 10, 685-698, 2002.

P.J. Strykowski, K.R. Sreenivasan. On the Formation and Suppression of Vortex Shedding at Low Reynolds Numbers. J. Fluid Mech, 218, 71-107.

G. I. Taylor. Stability of a Viscous Liquid Contained Between Two Rotating Cylinders. Philosophical transactions of the Royal Society of London, A 223, 289–343. Royal Society, London, 1923.

W. Tollmien. Über die Entstehung der Turbulenz. Nachrichten von der Gesellschaft der Wissenschaften zu Göttingen, Mathematisch-Physikalische Klasse, 21–44, 1929.